

**Surface-Adsorbed CO as a Molecular
Probe for the *In-Situ* Characterization
of Electrocatalytic Interfaces**

Charuni Menaka Gunathunge

A thesis
submitted to the Faculty of
the Department of Chemistry
in partial fulfillment
of the requirements for the degree of
Doctor of Philosophy

Boston College
Morrissey College of Arts and Sciences
Graduate School

September 2020

Surface-Adsorbed CO as a Molecular Probe for the *In-Situ* Characterization of Electrocatalytic Interfaces

Charuni Menaka Gunathunge

Advisor: Matthias M. Waegle, Assistant Professor of Chemistry

The properties of electrified interfaces, such as surface structure of metal catalyst, local pH, coverage of surface-adsorbed intermediates, interfacial electric field, and water structure, influence the activity and selectivity of electrocatalytic reactions. Because these interfacial properties often influence each other and undergo changes with applied potential, it is very challenging to identify the key characteristics of the interface that directly modulate electrocatalytic reactions. In this thesis, we demonstrate *in-situ* probing of electrochemical interfacial properties by employing surface-enhanced infrared (IR) absorption spectroscopy (SEIRAS) in conjunction with surface-adsorbed CO (CO_{ads}) as a molecular probe of the Cu/aqueous electrolyte interface. This interface shows potential for the reduction of CO_2 and CO to a wide variety of hydrocarbons. The CO and CO_2 reduction reactions (CO/ CO_2 RR) feature CO_{ads} as an intermediate; therefore, this interface is conveniently probed by CO_{ads} . In the first part of this thesis, we focus on investigating the dynamics of the surface morphology of the electrode during electrocatalysis. We found that the surface morphology of polycrystalline Cu undergoes reconstructions during CO/ CO_2 RR. We determined that these reconstructions can be induced by CO_{ads} and the local pH. As a result of the surface reconstructions, new specific surface sites form that can affect catalytic activity. For example, we detected an electrochemically inert CO_{ads} population that appears as a result of reconstruction processes. Further, to form a rigorous connection between the product formation and the atomic-level surface morphology of rough polycrystalline Cu electrodes, we combined SEIRAS with differential electrochemical mass-spectrometry (DEMS). We established the potential-dependence of the line shape

of the $\text{C}\equiv\text{O}$ stretch band as an indicator of the atomic-level surface morphology. The last part of the thesis focuses on the determination of properties of the electrochemical double layer. Specifically, we elucidated the effects of cation identity on the electrochemical double layer. By evaluating the $\text{C}\equiv\text{O}$ stretch frequency in the presence of alkali metal cations (Li^+ , K^+ , and Cs^+), we determined that the promotion of the CO reduction reaction is associated with a cation-dependent interfacial field.

Contents

1	Introduction	1
1.1	Introduction	1
2	Theory	8
2.1	Surface-Enhanced Absorption Spectroscopy	8
2.1.1	Electromagnetic Mechanism	10
2.1.2	Chemical Mechanism	11
2.2	Attenuated Total Reflection (ATR) IR Spectroscopy	12
2.2.1	Snell's Law	13
2.2.2	Total Internal Reflection	14
2.2.3	Evanescent Wave	15
2.2.4	Attenuated Total Reflection	16
2.3	Chemisorption of CO on Transition Metals	17
2.4	Dependence of the C≡O Stretch Frequency on CO Chemisorption Energy	19
2.5	Dependence of the C≡O Stretch Frequency on CO Coverage	22
2.5.1	Dynamical Dipole Coupling	23
2.5.2	Chemical Effects	25
2.6	Electrochemical Double Layer	27
2.6.1	Helmholtz Model	27
2.6.2	Gouy-Champann-Stern (GCS) Model	29
2.6.3	Electric Field at an Electrochemical Interface	31

2.7	Stark Effect	32
2.8	Properties of the Electrochemical Double Layer Beyond the Electric Field	34
3	Spectroscopic Observation of Reversible Surface Reconstruction of Copper	
	Electrodes under CO₂ Reduction	36
3.1	Introduction	36
3.2	Results	38
3.3	Discussion	40
3.4	Conclusions	45
3.5	Materials and Methods	46
3.6	Acknowledgements	48
3.7	Original Publication	50
4	Existence of an Electrochemically Inert CO Population on Cu Electrodes in	
	Alkaline pH	51
4.1	Introduction	51
4.2	Results and Discussion	52
4.3	Conclusions	62
4.4	Materials and Methods	63
4.5	Acknowledgements	65
4.6	Original Publication	65
5	Revealing the Predominant Surface Facets of Rough Cu Electrodes under	
	Electrochemical Conditions	66
5.1	Introduction	66
5.2	Results and Discussion	68
5.3	Conclusions	81

5.4	Materials and Methods	82
5.5	Acknowledgements	85
5.6	Original Publication	86
6	Probing Promoting Effects of Alkali Cations on the Reduction of CO at the Aqueous Electrolyte/Copper Interface	87
6.1	Introduction	87
6.2	Results and Discussion	89
6.3	Conclusions	98
6.4	Materials and Methods	98
6.5	Acknowledgements	100
6.6	Original Publication	101
7	Summary and Future Perspective	102

List of Figures

2.1	AFM image of a thin Cu film deposited on Si-ATR prism using an electroless deposition method. The scale bar is 200 nm. Image was acquired in a $1 \times 1 \mu\text{m}^2$ area with a Si cantilever (Nanosensors; Neuchatel, Switzerland; PPP-NCHR 10 M, 7 nm tip radius, 330 kHz resonance frequency, and 42 Nm^{-1} spring constant) at a 0.5 Hz scan rate in non-contact mode on a Park XE-100 AFM system (Park Americas; Santa Clara, CA). Reproduced from Ref [64].	9
2.2	Schematic of electromagnetic surface-enhancement mechanism. Incident IR beam polarizes the metal islands through the surface plasmon excitation, which induces a dipole moment (p) at the metal islands. The induced dipole moment creates a local electric field stronger than the incident beam. The black solid lines represent the electric field created around the metal islands. Reproduced from Ref [63].	10
2.3	Electrochemical cell setup for <i>in-situ</i> IR measurements in (A) IR reflection absorption spectroscopy (IRAS) and (B) Kretschmann attenuated total reflection (ATR) configurations [63].	12
2.4	Reflection and refraction of incident light at an interface between medium 1 and medium 2. n_1 and n_2 are the refractive indices of the two media. Light incident from (A) the rarer medium to the denser medium and (B) the denser medium to the rarer medium.	13

2.5	Schematic of the exponential decay of the evanescent wave along the z-axis of the interface at total internal reflection (The image is not to scale).	15
2.6	Schematic illustration of the electronic density of states (DOS) of <i>sp</i> and <i>d</i> -bands of a transition metal (left side) and the 5σ and $2\pi^*$ orbitals of CO in a vacuum (right side). The middle section shows the broadening and lowering of the energy of the CO states due to the interaction with the metal <i>sp</i> -band when CO is approaching the metal. These CO states further hybridize with the <i>d</i> -bands of the metal and split into bonding and anti-bonding orbitals. E_F : Fermi level energy, M: Transition metal. Reproduced from the Ref [75].	18
2.7	A schematic illustration of the dependence of the $C\equiv O$ stretch frequency ($\nu_{C\equiv O}$) on (a) the coordination number of CO to the metal ($\nu_{C\equiv O}$ red shifts with increasing coordination number of CO) and (b) the coordination number of the metal atom on which CO is adsorbed. For Cu and Au, $\nu_{C\equiv O}$ blue shifts with decreasing coordination number of the metal atom while $\nu_{C\equiv O}$ red shifts on Pt.	20

2.8	<p>Dipole coupling between two (A) identical $^{12}\text{C}^{16}\text{O}$ and (B) $^{12}\text{C}^{16}\text{O}$ and $^{13}\text{C}^{16}\text{O}$ molecules (The model described in Ref [80] was used to get the normal modes and corresponding intensities). Singleton frequencies of $^{12}\text{C}^{16}\text{O}$ and $^{13}\text{C}^{16}\text{O}$ are 2100 and 2053 cm^{-1}, respectively [80]. Green dashed lines show the amplitude and phase of the two new normal modes at lower frequency. Dark blue solid and light blue dashed lines show the amplitude and phase of the two new normal modes at higher frequency. The addition of the amplitude and phase of each normal mode at corresponding frequencies gives rise to the observed IR band due to dynamical dipole coupling (black solid line with shaded area). A Gaussian distribution of the CO populations were simulated using an arbitrary line width.</p>	24
2.9	<p>A simplistic view of an electrochemical double layer during an electrocatalytic process. Local electric field, interfacial pH, solvation environment, and proton donation can be influenced by adsorbed cations on the electrode, the interfacial water structure, anions near the interface, or other adsorbed molecular species. These characteristics can in turn can modulate the activity and selectivity of catalytic processes.</p>	28
2.10	<p>(A) Electrochemical double layer at a negatively charged metal/electrolyte interface as described by the Helmholtz model. Solvated cations form a compact layer near the surface of the metal electrode. The closest distance where solvated cations can be found is known as the OHP. (B) Electrochemical double layer structure proposed by the Gouy-Chapmann-Stern model, which consists of a OHP and a diffuse layer. The potential drop across the diffuse layer (ϕ_2) with respect to the potential at the bulk electrolyte is known as the zeta potential (ζ).</p>	30

2.11	Anharmonic potential curve of CO molecule. Dipole moment of CO in the first vibrational excited state ($\vec{\mu}_1$) is slightly larger than that in the ground state ($\vec{\mu}_0$) as the length of the CO molecule is slightly larger in the excited vibrational state. Here q represents the charge. The difference in the dipole moment ($\Delta\vec{\mu}$) gives rise to a shift in the vibrational frequency of CO ($\Delta\nu$) in the presence of an externally applied electric field ($\vec{\epsilon}(\phi)$) with the relationship $\Delta\nu = -\Delta\vec{\mu} \cdot \vec{\epsilon}(\phi)$. Adapted with permission from Ref [129]. Copyright 2015 American Chemical Society.	33
3.1	Potential dependence of C≡O stretch band of CO _{atop} on copper during CO reduction in 0.1 M KHCO ₃ electrolyte. LFB and HFB traces show Gaussian fittings for low frequency band and high frequency band, respectively. Total fit is the summation of LFB and HFB. Reproduced from Ref [30]. . .	39
3.2	Potential dependence of the integrated band areas of LFB and HFB of the C≡O stretch band as shown in Figure 3.1. Reproduced from Ref [30]. . .	39
3.3	(A) Representative potential dependence of C≡O stretch spectra during a cathodic scan (left) and an anodic scan (right) after reaching the most cathodic potential of -1.1 V vs. SHE. LFB, HFB, and Total fit have the same meaning as in Figure 3.1. (B) Comparison of integrated band areas of LFB and HFB during cathodic and anodic scans. Reproduced from Ref [30].	41
3.4	(A) Representative potential dependence of the carbonate and C≡O stretch bands. (B) Potential dependence of the integrated band area of carbonate band. (C) Comparison of the integrated band areas of LFB and HFB from Figure 3.2 and carbonate band (carbonate band are is scaled by -0.22 as indicated). Reproduced from Ref [30].	42

3.5	(A) Time evolution of C≡O stretch band during a potential jump from -0.70 to -1.10 V vs. SHE. (B) Integrated band areas of LFB (black circles) and HFB (black squares) of the spectra shown in (A). The exponential fittings for the LFB and HFB are shown in blue and red color traces, respectively. The inset shows the LFB multiplied by $m = 1.4$ and offset by $b = 100 \text{ mOD cm}^{-1}$	43
3.6	(A) Representative CVs collected at 20 (red), 40 (blue), 60 (green), 80 (yellow), and 100 (purple) mV/s scan rates to measure the double layer capacitance of the Cu film. (B) Red squares show the Double layer charging current vs. scan rate. Black dashed line is a fit to the data. The roughness of the Cu film was calculated by dividing the slope of the plot (B) by a factor of 2 and the double layer capacitance of a smooth Cu foil which is $28 \mu\text{F cm}^{-2}$ [153].	47
3.7	A schematic of the PEEK single compartment cell with the Pt counter electrode, leakless Ag/AgCl reference electrode and the thin Cu film as the working electrode.	49
4.1	Representative IR spectra of the C≡O stretch mode of (A) CO _{atop} and (B) CO _{bridge} collected during a cyclic voltammetric scan in 0.05 M Li ₂ CO ₃ (pH 11.4) at a scan rate of 10 mV/s. Cathodic forward and anodic reverse scans area shown in left and right panels, respectively. Reproduced from Ref [64].	53

4.2	(A) Integrated band areas of CO_{atop} (left ordinate, blue color squares) and $\text{CO}_{\text{bridge}}$ (right ordinate, red color circles) bands shown in Figure 4.1 as a function of applied potential. (B) Geometric current density during the potential scan (Geometric area of the Cu electrode is $\approx 1.9 \text{ cm}^2$). CV peaks are assigned according to the published data [42, 166]. Arrows indicate the direction of potential scan. Reproduced from Ref [64].	55
4.3	Integrated band areas of CO_{atop} (blue squares) and $\text{CO}_{\text{bridge}}$ (red circles) as a function of time during potential polarization experiments. Region1: -1.1 V potential with CO purging at 5 sccm rate. Region2: -1.1 V potential with Ar purging at 5 sccm rate. Region3: The potential was jumped and held at -1.75 V with Ar purging at 5 sccm rate. (A) and (B) Experiments were carried out in $0.05 \text{ M Li}_2\text{CO}_3$ (pH 11.4) with polarization times of 25 and 1 min in Region1, respectively. (C) Experiment was carried out in 0.1 M LiOH (pH 12.4) with a 1 min polrization time in Region1. Reproduced from Ref [64].	56
4.4	SERS data of Cu electrode in Ar-purged $0.05 \text{ M Li}_2\text{CO}_3$ at (A) -0.5 V and (B) -1.1 V . The black spectrum in (A) is collected at open circuit potential. Two major peaks at 517 and 610 cm^{-1} are assigned to Cu_2O . Reproduced from Ref [64].	59
4.5	Integrated band areas of CO_{atop} (blue squares) and $\text{CO}_{\text{bridge}}$ (red circles) at the truning potentials of -1.1 and 0.11 V during consecutive CVs. Data were collected in CO-saturated $0.05 \text{ M Li}_2\text{CO}_3$ at a scan rate of 10 mV/s . Hollow and solid symbols represent the band area at -1.1 and 0.11 V , respectively. Reproduced from Ref [64].	60

4.6	Formation energy of CO at different adsorption sites on Cu(111) and (100) as a function of applied electric field. A more positive electric field indicates that the potential has become more cathodic. Reproduced from Ref [64].	61
4.7	Activation barrier for the water-assisted hydrogenation of CO to CHO on Cu(100) as a function of applied electric field. A more positive electric field indicates that the potential has become more cathodic. Reproduced from Ref [64].	62
5.1	An AFM image of a CuAu-Si film. The scale bar is 200 nm. Image was acquired in a $1 \times 1 \mu\text{m}^2$ area with a Si cantilever (Nanosensors; Neuchatel, Switzerland; PPP-NCHR 10 M, 7 nm tip radius, 330 kHz resonance frequency, and 42 Nm^{-1} spring constant) at a 0.5 Hz scan rate in non-contact mode on a Park XE-100 AFMsystem (Park Americas; Santa Clara, CA). Reproduced from Ref [158].	69
5.2	DEMS/SEIRAS setup. RGA, CE, and RE denote residual gas analyzer, counter electrode, and reference electrode, respectively. The sampling tip was inserted through a polytetrafluoroethylene (PTFE) bellows and connected to a micrometer, enabling the fine adjustment of the tip-electrode distance. Reproduced from Ref [158].	70
5.3	DEMS collected on Cu-Si and CuAu-Si in CO saturated 0.1 M potassium phosphate buffer (PH = 7). (A) Electrochemical current densities. (B) H_2^+ ($m/z = 2$), (C) CH_3^+ ($m/z = 15$), and (D) C_2H_2^+ ($m/z = 26$) partial pressures. All the signals in the figure are divided by the roughness factor of the respective film. Reproduced from Ref [158].	71

5.4	Normalized absorbance of CO_{atop} band on Cu-Si and CuAu-Si films at saturation coverage at -1.3 V. The spectra were concurrently collected with the DEMS data shown in Figure 5.3. Reproduced from Ref [158].	73
5.5	Potential dependence of the $\text{C}\equiv\text{O}$ stretch of CO_{atop} on (A) Cu-Si and (B) CuAu-Si films. The anotation indicates the potential in V vs. Ag/AgCl. The spectra were collected concurrently with the DEMS data shown in Figure 5.3. Reproduced from Ref [158].	74
5.6	Cyclic voltammetry (CV) collected on (A) Cu(100) and (B) Cu(111) single crystals. CV collected on (C) Cu-Si and (D) CuAu-Si thin films. All the CVs were collected in Ar-saturated 0.1 M KOH at a scan rate of 50 mV/s. Geometric current density is shown in the pannels. Reproduced from Ref [158].	75
5.7	A CV collected on electroless deposited Au underlayer of CuAu-Si film in Ar-saturated 0.1 M H_2SO_4 at 50 mV/s scan rate. Geometric current density is shown in the figure. Reproduced from Ref [158].	77
5.8	Normalized absorbance of CO_{atop} collected in an isotopic mixture of 10% $^{12}\text{C}^{16}\text{O}$ + 90% $^{13}\text{C}^{18}\text{O}$ (solid line) and in isotopically pure $^{12}\text{C}^{16}\text{O}$ (dashed line) on (A) Cu-Si and (B) CuAu-Si films at -1.3 V. Reproduced from Ref [158].	78
5.9	Schematic summarizing the key findings. (Left) Cu-Si film that possesses (100) and defect sites has a higher probability of finding CO_{atop} on terrace sites, therefore giving a separate IR peak at $\approx 2045 \text{ cm}^{-1}$. (Right) CuAu-Si film that possesses (111) and defect sites has a lower coverage of CO_{atop} on terrace sites. Thus, a separate IR peak is not observed for CO_{atop} adsorbed on Cu(111) terrace sites. Reproduced from Ref [158].	80

5.10	Schematic of the home-build two-compartment polyetheretherketone (PEEK) SEIRAS electrochemical cell. Reproduced from Ref [158].	85
6.1	Representative IR spectra of the $C\equiv O$ stretch mode of CO_{atop} collected in CO-saturated 0.1 M DCO_3 ($M = Li^+, K^+, Cs^+$) during a cyclic voltammetric scan from -0.38 to -1.48 V vs. SHE at 2 mV/s scan rate. IR spectra collected during cathodic forward scan (left panels) and anodic reverse scan (right panels) are shown. Reproduced from Ref [109].	90
6.2	Normalized integrated band area of CO_{atop} shown in Figure 6.1 in 0.1 M DCO_3 ($M = Li^+, K^+, Cs^+$) as indicated in the panels. Red and blue traces represent data collected during cathodic forward and anodic reverse scans, respectively. The arrows indicate the direction of the potential scan. Reproduced from Ref [109].	91
6.3	Time dependence of the normalized band area of CO_{atop} following a potential step from saturation coverage of CO at -1.04 V to a reaction potential of -1.51 V vs. SHE. Data were collected in CO-saturated 0.1 M bicarbonate solutions as indicated. Reproduced from Ref [109].	92
6.4	$C\equiv O$ stretch frequencies as a function of potential collected in CO-saturated 0.1 M bicarbonates of Li^+ , K^+ , and Cs^+ containing electrolytes. The error bars show ± 2 standard deviation calculated from 3 independent experiments. Solid lines are linear fits to the experimental data. Reproduced from Ref [109].	93
6.5	Normalized integrated band area of CO_{atop} in 0.1 M Li^+ and Cs^+ bicarbonate ($pH^* 8.7$) and 0.05 M Li^+ and Cs^+ carbonate ($pH^* 11.4$ and 10.6 , respectively.) Reproduced from Ref [109].	95

6.6	Normalized integrated band area of CO _{atop} electrogenerated from reduction of CO ₂ . Experiments were carried out in CO ₂ -saturated 0.1 M alkali metal bicarbonate solutions (pH* 6.8±0.1) as indicated. Reproduced from Ref [109].	97
-----	---	----

List of Tables

2.1	C≡O Stretch Frequency as the CO Coverage Reaches Zero at Different Surface Facets with Corresponding CO Binding Energy Data	21
-----	--	----

Acknowledgements

First, I would like to acknowledge my doctoral advisor and my mentor for past five years, Prof. Matthias M. Waegele. He sets a perfect example of how a professional scientist should be, which I aspire to become one day. I'm truly grateful for his continuous guidance throughout my time in Boston College by patiently and rigorously discussing scientific and technical questions in order for me to excel as a scientist. His continual encouragement has helped me immensely to improve as a scientist as well as a person and molded me to the person who I am today. I'm truly proud to recognize my self as an advisee of Prof. Matthias M. Waegele. Further, I thank Prof. Matthias M. Waegele for providing me with the financial support throughout these years so that I can carry out the highest quality research I could, without any obstruction.

I would also like to acknowledge my thesis committee chair and the current department head of the Department of Chemistry, Boston College, Prof. Dunwei Wang and other committee members, Profs. Chia-Kuang Tsung and Udayan Mohanty, for offering their time and efforts. I'm grateful to Prof. Micheal J. Janik from Pennsylvania State University and his post-doctoral student, Dr. Yawei Li for successful collaborations and providing theoretical insights that helped us tremendously to acquire a better understanding of our research work.

I have fond memories working with Waegele's group members, Jingy Li, Xiang Li, Vincent Ovalle, Paul Hicks, Jinchun Yang, Connor Gallacher and Julie Hong. I'm truly blessed to work with this wonderful group of people, especially with Jingyi Li and Xiang Li who has began their Ph.D. work in the same year as I did. They were always there to discuss research, theories as well as providing assistance in every way that I can think of, contributing immensely to the success of the research that I did during past five years.

Finally, I would like to thank my family and friends for their extreme support. To

my parents, Mrs. Ajantha Aranwela and Mr. Bandu G. Gunathunge for their love, care and educational platform which took me to where I am today. I thank my sister, Naduni Gunathunge for her continuous love and always being there for me. Further, I am thankful for my mother-in-law, Mrs. Shriyani Kaluarachchi for her love, care and understanding. I am extremely grateful to Dr. Suraj Fernando and Mrs. Ramani Fernando for their continual encouragement, support and love. To my husband, Nelaka Govinna, I am forever grateful for his unconditional love and patients, and always supporting and pushing me to be the best version of my self.

To my husband and my parents, I dedicate this thesis.

Chapter 1

Introduction

1.1 Introduction

Electrocatalytic processes provide a sustainable strategy for the conversion of small molecules such as CO₂, H₂O and N₂ to value added fuels and commodity chemicals using renewable energy sources [1–5]. Further, electrocatalytic processes offer precise control over redox processes that are not realizable or difficult to achieve by other means [1–5]. Electrocatalytic processes are utilized not only in converting small molecules, but also in macro-molecular synthesis. Organic electrosynthesis presents greener and milder alternatives compared to conventional organic synthesis methods [6]. Accordingly, electrochemistry is used to perform technologically relevant chemical transformations, such as biomass conversion [7, 8], CO₂ reduction [9, 10], and water splitting [11, 12]. Nevertheless, electrochemical processes suffer from poor product selectivity, catalyst deactivation and require higher overpotentials [3, 13–15]. For instance, even though the thermodynamic potential for conversion of CO₂ to methane is 0.17 V vs. the reversible hydrogen electrode (RHE), during electrochemical CO₂ reduction, methane is observed at ≈ -1 V vs. RHE [10]. Also, evolution of unwanted side products, such as hydrogen gas, at cathodic potentials decrease the selectivity towards the desired products [1, 16].

To overcome the challenges associated with electrocatalytic processes as noted above,

a rigorous understanding of the electrode/electrolyte interface is essential. The complex nature of the interface between electrode and electrolyte renders the understanding of interfacial properties arduous. The surface morphology determines the ensemble of catalytically active surface sites, whose identities control the binding energy of surface-adsorbed intermediates [17–20]. The arrangement of ions, molecular co-catalysts, and the water structure on the electrolyte side of the interface can modulate interfacial pH, electric field, proton donation, solvation environment and adsorption energy of surface-adsorbed intermediates [21–29]. Moreover, the properties of the electrode and electrolyte sides interact with each other and evolve during the catalytic reaction conditions [30–32], making it even more challenging to understand the parameters that determine the activity and selectivity of electrocatalytic processes.

In-situ probing of the properties of the electrode/electrolyte interface is challenging and only a few techniques are available for this purpose, including X-ray techniques, atomic force microscopy (AFM), scanning tunneling microscopy (STM), surface-enhanced Raman scattering (SERS) and surface-enhanced infrared absorption spectroscopy (SEIRAS). Among these techniques for *in-situ* probing of the electrochemical interface, SEIARS has emerged as a convenient method [33–35]. When SEIRAS is coupled with a suitable molecular probe, this technique provides atomic level information of the structure and dynamics of double layer properties under reaction conditions. The C≡O stretch frequency of CO_{ads} depends on the coordination number of the metal atom on which CO is adsorbed and on the double layer properties. Further, CO_{ads} is an on-pathway intermediate of technologically significant reactions such as CO₂ reduction and CO oxidation reactions [36–38]. In addition, CO_{ads} can be used as a spectator species of other reactions. For these reasons, CO_{ads} is an attractive probe of the electrocatalytic interface.

The C≡O stretch frequency however is affected by CO coverage (dynamical dipole coupling, chemical effects), electric field, co-adsorbates, and interfacial water structure.

Therefore, it is important to develop strategies for the interpretation of the $\text{C}\equiv\text{O}$ stretch band of CO_{ads} . In this thesis we demonstrate how to unveil the *in-situ* properties of catalyst morphology and electric double layer by employing CO_{ads} as a molecular probe.

In the first part of this thesis, we focus on the influence of the electrode side on activity and selectivity of electrocatalytic processes. Activity and selectivity of electrocatalytic reactions depend distinctly on the morphology of the catalyst [39–43]. For instance, it has been suggested that Pt(111) terrace sites show the least activity towards CO oxidation in 0.1 M NaOH electrolyte, while step and kink sites of Pt(110) and (100) are more active (oxidation potentials of 0.75 and 0.35 V vs. RHE, respectively) [40]. Similarly, the selectivity for C_{2+} hydrocarbons from CO_2 reduction reaction (CO_2RR) is about six times higher on oxide-derived copper electrodes compared to that on a polycrystalline copper foil [43].

However, morphology of the catalyst can be greatly affected during catalysis [44–48]. It has been shown that polycrystalline copper undergoes reconstruction within tens of minutes to yield Cu(100) surface facets when it is exposed to -0.9 V vs. the standard hydrogen electrode (SHE) in 0.1 M KOH electrolyte [46, 47]. Further, it has been demonstrated that Au(100) undergoes reconstruction under cathodic applied potentials in 0.1 M HClO_4 [48]. Eren *et al.* have shown that the Cu(111) surface forms CO-stabilized Cu clusters when it is exposed to CO gas with pressures higher than 0.2 torr [45]. By employing ambient pressure X-ray photoelectron spectroscopy (APXPS), they have further shown that this Cu cluster formation activates the surface for water dissociation during the water-gas shift reaction [45]. These examples emphasize that knowledge of the morphology of the catalyst, especially under reaction conditions, is crucial in developing better catalysts.

In Chapter 3, we demonstrate that copper catalyst's surface undergoes reversible reconstruction during CO_2RR , by utilizing atop-bound CO (CO_{atop}) as an *in-situ* probe [30]. The proposed theory is based on the observation of two distinct frequencies for the $\text{C}\equiv\text{O}$

stretch mode with SEIRAS and surface-enhanced Raman scattering (SERS): a low frequency band (LFB) $\approx 2050 \text{ cm}^{-1}$ at moderate cathodic potentials $< -1 \text{ V}$ vs. standard hydrogen electrode (SHE), and a high frequency band (HFB) $\approx 2080 \text{ cm}^{-1}$ at cathodic potentials $> -1 \text{ V}$ vs. SHE. The LFB and HFB bands are assigned to CO_{atop} on terrace and defect copper surface sites, respectively. HFB appears only when the LFB band area reaches a significant value of $\approx 100 \text{ mOD cm}^{-1}$, suggesting that adsorbed CO induces surface reconstruction that forms undercoordinated copper surface sites. Further, the simultaneous enhancement of the intensity of Raman scattering related to the Cu-C bond ($\approx 345 \text{ cm}^{-1}$) and the frustrated rotation of CO_{atop} ($\approx 285 \text{ cm}^{-1}$) with the appearance of the HFB, support the surface reconstruction hypothesis. Observation of a similar trend during cathodic and anodic scans demonstrates that this adsorbed CO induced surface reconstruction is reversible.

The preference for a particular adsorption configuration of adsorbed CO on metal catalysts can be influenced by aspects such as electrolyte pH and catalyst morphology. The sensitivity of the $\text{C}\equiv\text{O}$ stretch frequency to the adsorption configuration qualifies it as a powerful probe to study morphological changes of catalysts during electrochemical processes. In Chapter 4, we show that IR spectra collected in CO saturated $0.05 \text{ M Li}_2\text{CO}_3$ exhibit two distinct bands in the frequency ranges of $1800 - 1900$ and $2000 - 2100 \text{ cm}^{-1}$, which are due to bridge-bound CO ($\text{CO}_{\text{bridge}}$) and CO_{atop} configurations, respectively. During a cathodic polarization experiment at -1.1 V vs. SHE, CO_{atop} converts into $\text{CO}_{\text{bridge}}$ below the saturation coverage of CO_{ads} . This conversion of CO_{atop} to $\text{CO}_{\text{bridge}}$ is greater in long cathodic polarization experiments, but lesser in short cathodic polarization experiments (25 vs. 1 min cathodic polarization at -1.1 V vs. SHE). Increase of the $\text{CO}_{\text{bridge}}$ band area with time indicates that the $\text{CO}_{\text{bridge}}$ configuration on copper is favored in high pH conditions: The interfacial pH increases as hydroxide ions accumulate with time due to the concurrent hydrogen evolution reaction. The origin of the promotion of

$\text{CO}_{\text{bridge}}$ over CO_{atop} in high pH is suggested to be the formation of Cu(100) and (111) sites with pH-induced surface reconstruction of copper. This work demonstrates that the different binding configurations manifested by different frequencies of the $\text{C}\equiv\text{O}$ stretch band can be utilized to track the dynamics of the catalyst under electrochemical reaction conditions.

The $\text{C}\equiv\text{O}$ stretch frequency of CO_{ads} is influenced by the CO coverage through dynamical dipole coupling and chemical effects. Therefore, the $\text{C}\equiv\text{O}$ stretch frequency at high CO coverage does not reflect the true structure and morphology of the underlying metal catalyst in a straightforward manner. Even at low CO coverage, the $\text{C}\equiv\text{O}$ stretch frequency cannot be used as a sole probe to distinguish each of the crystallographic facets: The $\text{C}\equiv\text{O}$ stretch frequency on Cu (111) and (100) show only 1 cm^{-1} difference. In Chapter 5 we demonstrate that the relative amplitude of specific frequencies of the CO_{atop} band with applied potential can reveal the crystallographic facets of two polycrystalline copper catalysts, electrolessly deposited copper on a Si-ATR (attenuated total reflection) prism (Cu-Si) and electrochemically deposited copper on a gold supported Si-ATR prism (CuAu-Si). A distinct potential dependence of the $\text{C}\equiv\text{O}$ stretch frequency is observed on Cu-Si and CuAu-Si films in the low CO coverage regime at potentials $< -1\text{ V}$ vs. Ag/AgCl: On the Cu-Si film, the $\text{C}\equiv\text{O}$ stretch band appears $\approx 2045\text{ cm}^{-1}$ followed by an appearance of a second band $\approx 2080\text{ cm}^{-1}$ with increasing cathodic potentials. In contrast, on the CuAu-Si film, a single band $\approx 2080\text{ cm}^{-1}$ dominates at all potentials. This difference in the potential dependence of the $\text{C}\equiv\text{O}$ stretch band has led to the discovery that these two films possess disparate exposed surface facets.

By employing cyclic voltammetric characterization, we show that the Cu-Si film mainly possesses Cu(100) facets, whereas the CuAu-Si film possesses mostly Cu(111) facets. The difference in the probability of the CO occupancy of Cu(100) vs. (111) terrace sites can be observed as the difference in the potential-dependence of the lineshape of the $\text{C}\equiv\text{O}$

stretch band on Cu-Si and CuAu-Si films: On Cu-Si, a distinct IR band at $\approx 2045 \text{ cm}^{-1}$ is observed. This work demonstrates the unique sensitivity of the potential dependence of the $\text{C}\equiv\text{O}$ stretch band on the morphology of the underlying metal catalyst. The difference in morphology of Cu-Si and CuAu-Si films is further reflected by the difference in onset potentials for ethylene evolution, which is detected employing a combined SEIRAS and differential electrochemical mass spectrometry (DEMS) setup. Further, isotopic dilution experiments show that the relative CO coverage on the Cu-Si film is higher than that on the CuAu-Si film, confirming our assignment of the predominant surface facets of these two Cu thin films.

In Chapter 6 of this thesis, we illustrate an example for the utilization of CO_{ads} as a molecular probe to determine the properties of electrolyte side of the electrochemical interface. Here, we reveal that the interfacial electric field increases when moving from Li^+ to Cs^+ containing electrolyte during CORR conditions. Recent theoretical studies have shown that a greater interfacial electric field would enhance the activity of CO_2RR either by stabilizing the intermediates subsequent to CO or by decreasing the thermodynamic overpotential leading to the CHO intermediate from CO_{ads} [49, 50]. By employing *in-situ* SEIRAS, direct experimental evidence to show that an increase in the interfacial electric field enhances the reaction rate of CORR has been provided by experiments carried out in 0.1 M MDCO_3 ($\text{M}=\text{Li}^+, \text{K}^+, \text{Cs}^+$) electrolyte saturated with CO. Inspection of the integrated band area of CO_{atop} at a potential of -1.51 V vs. SHE revealed that the CO reduction rate in Cs^+ -containing electrolyte is one order of magnitude faster than that in Li^+ -containing electrolyte. Analysis of the frequency of CO_{atop} as a function of potential suggests that regardless of similar electrochemical Stark tuning rates of $\approx 30 \text{ cm}^{-1} \text{ V}^{-1}$ in the presence of all three cations, CO_{atop} frequencies in the K^+ and Cs^+ -containing electrolytes show a shift to lower wavenumbers with respect to the frequency in Li^+ containing electrolyte by about 1.4 and 3.7 cm^{-1} , respectively. This observed decrease in the

frequency of CO_{atop} for a given applied potential indicates an increase in the interfacial electric field with increasing cation size, explaining the observed increment in the CO reduction rate with increasing alkali cation size. Further, this investigation provides insights into the origin of the cation effects observed during CO_2RR .

The work presented in this thesis illustrates that the $\text{C}\equiv\text{O}$ stretch frequency of CO_{ads} observed with SEIRAS can reveal *in-situ* structural properties of electrode/electrolyte interface. We expect this comprehensive knowledge would lead to the development of better catalysts for important electrocatalytic processes that are mentioned in the above discussion. In the final chapter of this thesis (Chapter 7), a future perspective of the field explaining possible improvements of the experimental setups, methodologies and analyses are provided.

Chapter 2

Theory

2.1 Surface-Enhanced Absorption Spectroscopy

In 1980, Hartstein *et al.* observed that the IR absorption of a thin organic film of 4-nitrobenzoic acid is enhanced by a factor of ≈ 20 in the presence of a Ag overlayer or an underlayer on/under the organic thin film [51]. With this discovery, it was understood that the IR signal of molecules can be enhanced by a factor of 10^1 - 10^2 when the molecules are adsorbed on a rough thin metal layer [52, 53]. This surface enhancement was observed in a variety of metals such as Ag, Au, Cu, Pt, Pd, Pb, Rh, Ru and In [54–60]. Osawa and coworkers have carried out extensive experiments to understand the mechanisms and the properties of surface-enhanced infrared absorption spectroscopy (SEIRAS) [52, 54, 61, 62]. Using thin adlayers of p-nitrobenzoic acid on Ag island films deposited on CaF_2 , Osawa *et al.* have found that the surface enhancement is influenced by the shape and the size of metal islands [54]. Further, the IR signal of molecules adsorbed on metal islands with the molecule's axis perpendicular to the local surface of metal islands is selectively enhanced. This enhancement is short range and is present within ~ 5 nm from the metal island surface [52]. Additionally, a greater enhancement is observed for chemisorbed molecules compared to physisorbed molecules.

The enhancement mechanism of SEIRAS is similar to the mechanism of surface-

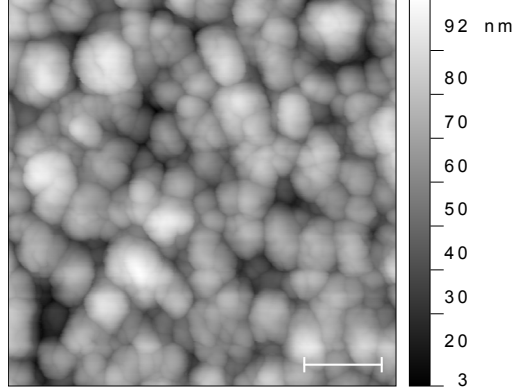


Figure 2.1: AFM image of a thin Cu film deposited on Si-ATR prism using an electroless deposition method. The scale bar is 200 nm. Image was acquired in a $1 \times 1 \mu\text{m}^2$ area with a Si cantilever (Nanosensors; Neuchatel, Switzerland; PPP-NCHR 10 M, 7 nm tip radius, 330 kHz resonance frequency, and 42 Nm^{-1} spring constant) at a 0.5 Hz scan rate in non-contact mode on a Park XE-100 AFM system (Park Americas; Santa Clara, CA). Reproduced from Ref [64].

enhanced Raman scattering (SERS). Two different mechanisms, electromagnetic and chemical mechanisms, have been suggested to be responsible for the surface enhancement.

Generally, the IR absorption (A) is expressed as [63]:

$$A \propto \left| \frac{\partial \mu}{\partial Q} \cdot E \right|^2 = \left| \frac{\partial \mu}{\partial Q} \right|^2 |E|^2 \cos^2 \theta \quad (2.1)$$

where $\frac{\partial \mu}{\partial Q}$ is the derivative of the vibrational dipole moment with respect to a normal coordinate Q , *i.e.* the absorption coefficient, E is the electric field that excites the molecule, and θ is the angle between the two aforementioned terms.

As mentioned above, the island structure of the metal film is important for the surface enhancement. Figure 2.1 shows an AFM image of a thin Cu metal film deposited on a Si-ATR prism. The Cu film consists of ~ 40 nm metal islands. Surface enhancement of the IR signal occurs when the average size of the metal islands is smaller than the wavelength of the incident IR beam. The electromagnetic mechanism assumes an increase in $|E|^2$ while the chemical mechanism assumes an increase in the absorption coefficient, $\left| \frac{\partial \mu}{\partial Q} \right|^2$.

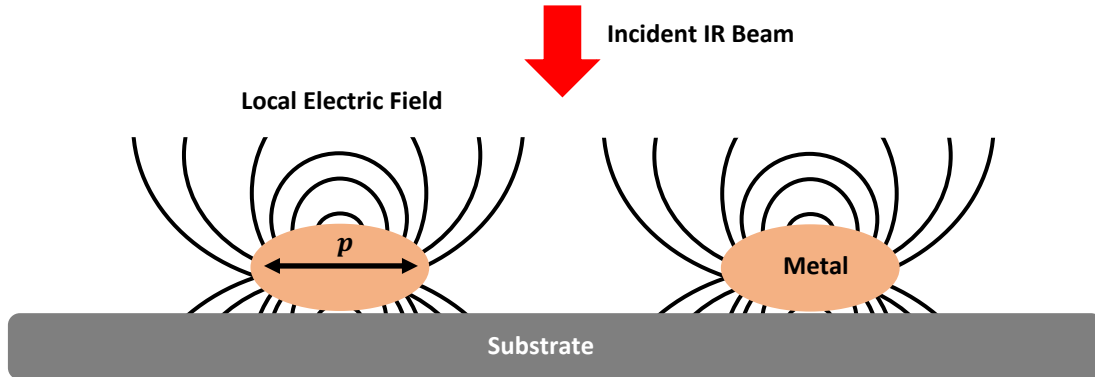


Figure 2.2: Schematic of electromagnetic surface-enhancement mechanism. Incident IR beam polarizes the metal islands through the surface plasmon excitation, which induces a dipole moment (p) at the metal islands. The induced dipole moment creates a local electric field stronger than the incident beam. The black solid lines represent the electric field created around the metal islands. Reproduced from Ref [63].

2.1.1 Electromagnetic Mechanism

Metal islands are polarized in the presence of incident IR radiation through excitation of their localized plasmon resonance. Due to this polarization of the metal islands, a dipole moment is induced at the center of the metal islands. The magnitude of this induced dipole moment (p) can be written as [52]:

$$p = \alpha V E \quad (2.2)$$

where α and V are polarizability and the volume of the metal islands and E is the amplitude of the incident electric field. This induced dipole moment p , creates an electric field around the metal islands that excites adsorbed molecules. This local electric field created by p is larger than the incident electric field, thereby increasing the $|E|^2$ term in Equation 2.1. The

increase in $|E|^2$ gives rise to the enhancement in IR absorption. Further, the local electric field created by p can be expressed as [52]:

$$|E_{local}|^2 = 4p^2/l^6 \quad (2.3)$$

where l is the distance from the center of the metal islands. This relationship between $|E_{local}|$ and l explains the short range nature of the surface enhancement.

2.1.2 Chemical Mechanism

The chemical mechanism has been suggested to also contribute to the surface enhancement of IR absorption on metal thin films. One chemical contribution is the orientation of the adsorbed molecules [54]. Chemisorption can preferentially orient the adsorbed molecules such that the molecular axis is perpendicular to the local surface of the metal islands, resulting in an enhancement of the IR signal. The preferentially oriented chemisorbed molecules possess a better surface enhancement than randomly oriented physisorbed molecules.

The second and well-studied chemical influence on SEIRAS is the increment of the absorption coefficient, $|\partial\mu/\partial Q|^2$ [52, 65]. It has been predicted that the absorption coefficient is enhanced by intensity borrowing from charge oscillations that occur between the molecular orbitals of the adsorbed molecules and the metal surface. Further, contribution from the chemical mechanism to SEIRAS is determined to be less than the contribution from the electromagnetic mechanism. However, it is emphasized that additional theoretical and experimental investigations are required to gather a comprehensive understanding of the chemical mechanism on SEIRAS.

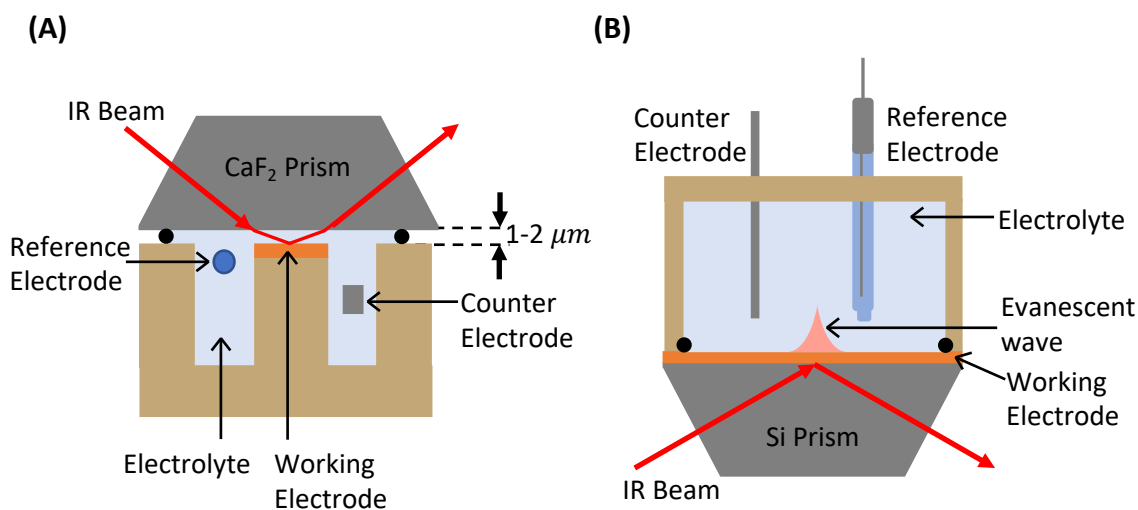


Figure 2.3: Electrochemical cell setup for *in-situ* IR measurements in (A) IR reflection absorption spectroscopy (IRAS) and (B) Kretschmann attenuated total reflection (ATR) configurations [63].

2.2 Attenuated Total Reflection (ATR) IR Spectroscopy

Spectroelectrochemistry is a powerful tool to collect information on the dynamics of metal/electrolyte interfaces and adsorbed molecular species under *operando* conditions. IR reflection absorption spectroscopy (IRAS) serves this purpose. Figure 2.3(A) shows the IRAS configuration. The main drawbacks related with this configuration are: (1) Poor mass transport due to the presence of a very thin electrolyte layer. (2) Higher solution resistance which results in slower reaction kinetics [35]. The Kretschmann attenuated-total reflection (ATR) configuration as shown in Figure 2.3(B) overcomes the above mentioned drawbacks of the IRAS configuration. The working electrode of the ATR configuration is a thin metal film (10-100 nm thick) deposited on an ATR prism using either sputtering, e-beam evaporation or electroless deposition methods [30, 50, 66–69]. Fundamental theories related to ATR-spectroscopy are described below.

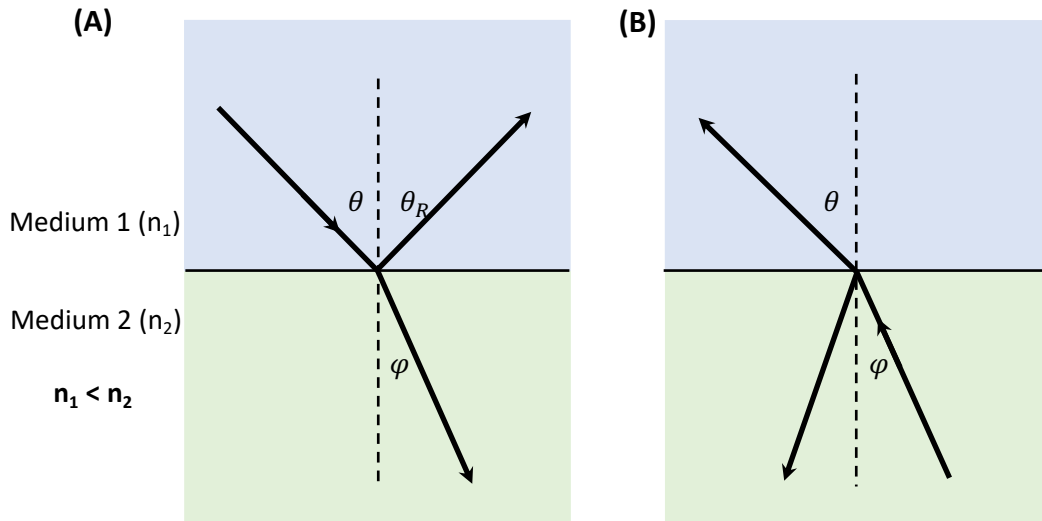


Figure 2.4: Reflection and refraction of incident light at an interface between medium 1 and medium 2. n_1 and n_2 are the refractive indices of the two media. Light incident from (A) the rarer medium to the denser medium and (B) the denser medium to the rarer medium.

2.2.1 Snell's Law

When light travels through a medium with a refractive index of n_1 and meets another medium with a refractive index of n_2 , the incident light at the interface splits into two components, reflected and refracted light as shown in Figure 2.4. The law of reflection, which is the first equality of Equation 2.4 explains that the angle of incidence (θ) is equal to the angle of reflection (θ_R) in the same medium [70]. The relationship between the angle of incidence, angle of refraction, and refractive indices of two media, is given by the law of refraction, also known as “Snell's Law”. The second equality of Equation 2.4 shows this relationship [70].

$$n_1 \sin \theta = n_1 \sin \theta_R = n_2 \sin \phi \quad (2.4)$$

2.2.2 Total Internal Reflection

When light is incident from a low refractive index medium, the angle of refraction (φ) is smaller than the angle of incidence (θ) (Figure 2.4(A)). For this instance, the refractive angle φ reaches its maximum value when the incident angle $\theta = 90^\circ$. From Snell's law, the maximum refraction angle at $\theta = 90^\circ$ is [70]:

$$\sin(\varphi_{max}) = n_1/n_2 . \quad (2.5)$$

However, when light is incident from a higher refractive index medium as shown in Figure 2.4(B), the refractive angle θ becomes larger than the incident angle φ . When the incident angle reaches φ_{max} , the refractive angle $\theta = 90^\circ$. With further increase in the incident angle φ , the refractive angle becomes $> 90^\circ$. In this situation the refractive light beam vanishes and the incident light is totally reflected at the interface [70]. Therefore, the phenomenon where the incident light beam is totally reflected at the interface is known as “total internal reflection”. In this instance, the incident angle φ_{max} is also referred to as the critical angle (φ_c). Si and Ge are two frequently used materials as the denser medium in spectro-electrochemical studies. The critical angle (φ_{max}) for Si and Ge is in the range of $\approx 20 - 30^\circ$ [35]. Therefore, the incident angle should be higher than 30° . The preferred angle of incidence is usually in the range of $60 - 80^\circ$ [35].

The naming conventions “external” and “internal” refer to the medium that the light enters: If light enters from a rarer medium to a denser medium, then the reflection is called “external reflection”. If light enters from a denser medium to a rarer medium the reflection is called “internal reflection”.

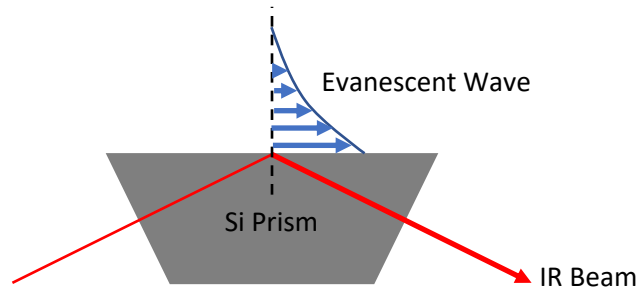


Figure 2.5: Schematic of the exponential decay of the evanescent wave along the z-axis of the interface at total internal reflection (The image is not to scale).

2.2.3 Evanescent Wave

During total internal reflection, incident and reflected waves are the only waves that are present at the interface of the denser and the rarer media. The transmitted wave that is propagating away from the surface is absent at the interface during total internal reflection [70, 71]. Boundary conditions explain the behaviour of the electromagnetic fields at an interface between a vacuum and a dielectric medium [72]. These conditions are derived following applications of Maxwell's equations and the Gauss and Stokes theorems [72]. Boundary conditions state that [70]: (1) The tangential component of the electric field of the electromagnetic wave is continuous at the interface although the normal component has a jump at the interface. (2) Tangential and normal components of the magnetic field are continuous at the interface. Accordingly, the presence of an electromagnetic wave at both sides of the interface is expected. The electromagnetic wave that is present at the rarer medium during total internal reflection is known as the “evanescent wave”. Due to energy conservation, the evanescent wave does not propagate away from the interface. This wave propagates parallel to the interface and exhibits an exponential decay along the normal axis of the interface as shown in Figure 2.5.

“Penetration depth” is the distance from the interface, where $1/e$ of the maximum

amplitude of the evanescent wave can be found. The relationship between the penetration depth (d_p) and the refractive indices of the media, incident angle and the wavelength of the light (λ) is expressed as [70]:

$$d_p = \frac{\lambda}{2\pi\sqrt{n_1^2\sin^2\theta - n_2^2}}. \quad (2.6)$$

According to Equation 2.6, d_p decreases with increasing incident angle. Typical d_p for a incident light with 1000 cm^{-1} wavelength is in the range of $1.4 - 5\ \mu\text{m}$ for media with $n_1 = 1.5$ and $n_2 = 1$ [70]. The incident angle for the above example varies from 45° to 90° .

2.2.4 Attenuated Total Reflection

As for total internal reflection, the interface is made up of two non-absorbing media [70]. However, in practical scenarios usually the rarer medium is an IR absorbing medium such as an aqueous or an organic solvent. When the rarer medium is an IR absorbing medium, a part of the electromagnetic energy of the evanescent wave is absorbed in the rarer medium. As a result, the evanescent wave is no longer parallel to the interface but has a slight angle to it. Further, the diminished energy of the evanescent wave is continuously replenished by leaking the incident electromagnetic energy through the interface. Therefore, the reflected wave at an interface with an absorbing rarer medium does not carry the total energy of the incident wave, but the energy is attenuated. This phenomenon is known as “attenuated total reflection” (ATR) and has practical usage in the context of electrochemistry.

2.3 Chemisorption of CO on Transition Metals

Understanding of CO chemisorption on metals is crucial for the investigation of surface morphology and electrochemical interfacial properties using CO_{ads} as a molecular probe. The Blyholder model [73], which was proposed almost 60 years ago, explains that the chemisorption of CO occurs through charge transfer from the filled CO 5σ orbital to empty metal orbitals (σ bond) and from filled metal orbitals to the CO $2\pi^*$ orbital (σ -donation/ π -backdonation). Using *ab initio* calculations, Hammer, Morikawa and Nørskov (HMN) have developed a more sophisticated model to describe CO chemisorption on transition metals in an atop-bound configuration (CO_{atop}) [74]. The HMN model for interaction between the density of states (DOS) of CO molecular orbitals with the DOS of a transition metal is illustrated in Figure 2.6.

According to the HMN model, when a CO molecule approaches a transition metal, CO states are broadened and shifted to lower energy due to the interaction with the *sp*-bands of the metal. Interaction between CO and the *d*-bands of the metal further results in splitting of the CO states into bonding and anti-bonding levels. The HMN model demonstrates that the hybridization between the *d*-bands of the transition metal and the CO $2\pi^*$ state makes a significant contribution to the total CO chemisorption energy. The degree of hybridization between metal *d*-bands and CO $2\pi^*$ depends largely on the energy of the center of the metal *d*-bands (ϵ_d). Hammer *et al.* have shown that the hybridization between metal *d*-bands and CO $2\pi^*$ increases with increasing ϵ_d , resulting in an increase in the CO chemisorption energy. ϵ_d depends on (1) the identity of the transition metal; ϵ_d increases from right to left in a row of transition metals in periodic table and (2) the crystallographic facet; low-index facets have a higher ϵ_d than high-index facets. Further, hybridization between metal *d*-bands and CO $2\pi^*$ increases with increasing coordination number of the CO molecule to the metal: Bridge-bound CO ($\text{CO}_{\text{bridge}}$) has a higher chemisorption energy compared to

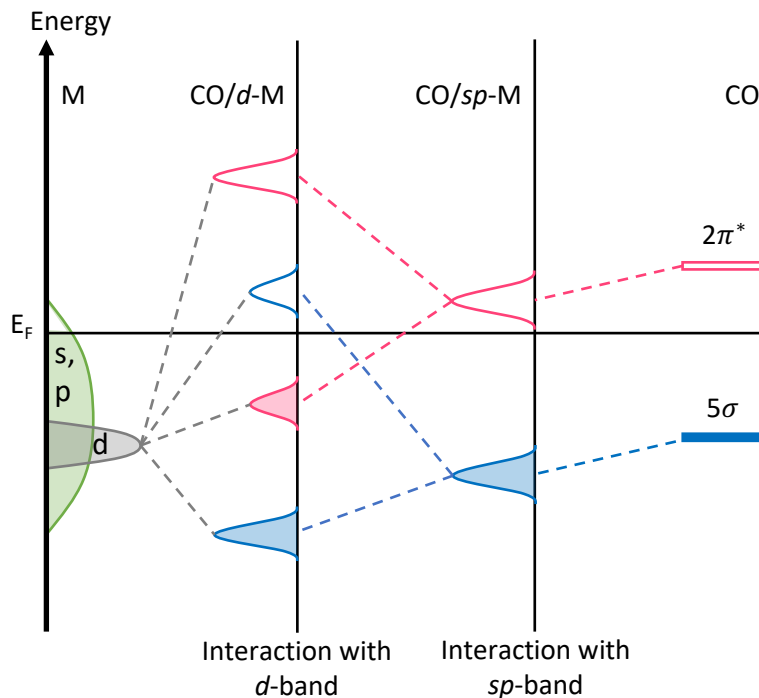


Figure 2.6: Schematic illustration of the electronic density of states (DOS) of sp and d -bands of a transition metal (left side) and the 5σ and $2\pi^*$ orbitals of CO in a vacuum (right side). The middle section shows the broadening and lowering of the energy of the CO states due to the interaction with the metal sp -band when CO is approaching the metal. These CO states further hybridize with the d -bands of the metal and split into bonding and anti-bonding orbitals. E_F : Fermi level energy, M: Transition metal. Reproduced from the Ref [75].

that of CO_{atop} .

In the HMN model, ϵ_d represents the average DOS of all five d -orbitals for a given transition metal. Rappe and coworkers have modified the HMN model to identify the influence of each d -orbital to the CO chemisorption energy separately [76, 77]. For instance, they have shown that CO chemisorption energy for CO_{atop} can be calculated more accurately by using only the DOS arising from the d_{xz} and d_{yz} (ϵ_{xzyz}) orbitals as these are the only two d -orbitals that interact with the CO $2\pi^*$ orbital when CO is bound in an atop configuration. They have further demonstrated that the CO chemisorption energy does not linearly scale with the energy of the collective d -bands center (ϵ_d). However, the CO chemisorp-

tion energy scales linearly with the energy of the d_{xz} and d_{yz} (ϵ_{xzyz}) orbitals, illustrating that orbital-specific analysis predicts the CO chemisorption energy more accurately than the basic HMN model.

In addition to these theoretical models, experimental investigations have also been carried out to understand the molecular orbitals involved in CO chemisorption on metals. Going along with the notion put forward by the theoretical models described above, X-ray emission spectroscopy (XES) studies have shown that both σ and π bonding between CO and metal result from hybridization of orbitals of CO and metal [78, 79]. XES studies have further suggested that the CO-metal σ -interaction involves 4σ and 5σ orbitals of CO and the formation of CO-metal π -bond involves hybridization of both 1π and $2\pi^*$ orbitals of CO with metal orbitals. For late transition metals, the π -bond was suggested to strengthen the CO-metal bonding by acting as an attractive force, while σ -interaction weakens the CO-metal bond by acting as a repulsive force. Fohlisch *et al.* have proposed that the equilibrium between these attractive π and repulsive σ contributions between metal and CO determines the CO chemisorption energy. XES studies carried out on nickel and copper metals have shown that the hybridization between metal and CO orbitals increases with increasing d -band energy [78]. Moreover, they have shown that the strength of π bonding between CO and nickel increases with increasing coordination of CO molecule to nickel [79].

2.4 Dependence of the C \equiv O Stretch Frequency on CO Chemisorption Energy

The C \equiv O stretch frequency of CO chemisorbed on metal surfaces is directly affected by the strength of the CO-metal bond. As noted in Section 2.3, for a given metal, the CO-metal bond strength can be influenced by (1) the coordination number of CO molecule

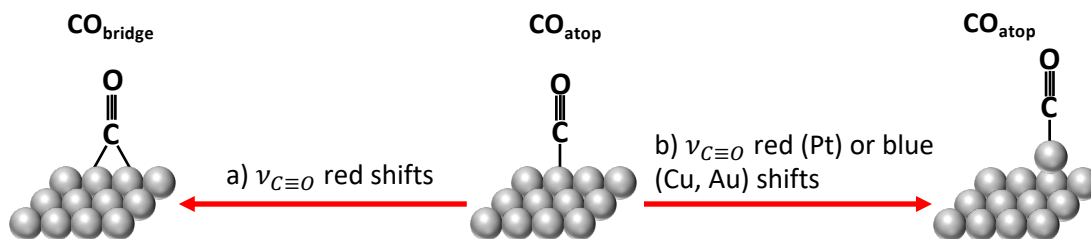


Figure 2.7: A schematic illustration of the dependence of the C≡O stretch frequency ($\nu_{C\equiv O}$) on (a) the coordination number of CO to the metal ($\nu_{C\equiv O}$ red shifts with increasing coordination number of CO) and (b) the coordination number of the metal atom on which CO is adsorbed. For Cu and Au, $\nu_{C\equiv O}$ blue shifts with decreasing coordination number of the metal atom while $\nu_{C\equiv O}$ red shifts on Pt.

(e.g., atop, 2-fold, 3-fold) and (2) the crystallographic facet, *i.e.* the coordination number of the metal atom on which CO is adsorbed (Figure 2.7). Table 2.1 summarizes experimentally observed C≡O stretch frequencies of CO_{ads} with related binding energies determined by either experimental or theoretical approaches at low CO coverage. According to the frequency data summarized in Table 2.1, CO_{atop} is generally observed in $\approx 2000 - 2100 \text{ cm}^{-1}$ and $\text{CO}_{\text{bridge}}$ (use to denote either 2-fold or 3-fold bound CO) is observed in $\approx 1800 - 1900 \text{ cm}^{-1}$ frequency ranges, respectively. This trend in the frequency of CO_{atop} and $\text{CO}_{\text{bridge}}$ follows the interpretation of the CO chemisorption on transition metals put forward by the theoretical models mentioned in Section 2.3: With increasing coordination number of CO molecule, hybridization between CO $2\pi^*$ and metal d -band increases. The increase in hybridization results in a weakening and correspondingly a red shift of the C≡O stretch frequency.

The values in Table 2.1 show that the C≡O stretch frequency is sensitive to different crystallographic facets as the CO chemisorption energy differs with coordination number of the metal atom. Mainly, the C≡O stretch frequency enables the recognition of high-index vs. low-index facets as C≡O stretch frequency exhibits an identifiable difference when CO is adsorbed on high-index facets compared to that on low-index facets. For

Table 2.1: C≡O Stretch Frequency as the CO Coverage Reaches Zero at Different Surface Facets with Corresponding CO Binding Energy Data

Facet	C≡O Stretch Frequency [†]	CO Binding Energy [‡]	Ref	
	(cm ⁻¹)	(eV)	†	‡
Cu(111)	2078 ^{a*}	0.49 ^{a*}	[80]	[81]
Cu(100)	2079 ^{a*}	0.53 ^{a*}	[80]	[81]
Cu(110)	2088 ^{a*}	0.56 ^{a*}	[80]	[81]
Cu(211)	2110 ^{a*}	0.61 ^{a*}	[80]	[81]
Cu(poly)	2105 ^{a*}	0.60 ^{a*}	[80]	[81]
Au(111)	2065 ^{a*}	0.16 ~ 0.34 ^{a#}	[82]	[83–86]
Au(100)	2073 ^{a*}	0.38, 0.46 ^{a#}	[82]	[84, 85]
Au(110)	2118 ^{a*}	0.53 ^{a#}	[87]	[84]
Au(211)	2122 ^{a*}	0.54 ^{a#}	[88]	[85]
Au(332)	2124 ^{a*}	0.65 ^{a#}	[89]	[90]
Pt(111)	2089 ^{a*}	-	[91]	
Pt(100)	2088 ^{a*}	-	[80]	
Pt(432)	2072 ^{a*}	-	[80]	
Pt(533)	2067 ^{a*}	-	[80]	
Pd(111)	1823 ^{b*}	1.47 ^{b*}	[92]	[93]
Pd(100)	1890 ^{c*}	1.58 ^{c*}	[94]	[93]
Pd(110)	1917 ^{c*}	1.73 ^{c*}	[95]	[93]
Pd(210)	1878 ^{c*}	1.52 ^{c*}	[92]	[93]

^a atop-bound CO ^b 2-fold bound CO ^c 3-fold bound CO
* experimental data # computational data

copper and gold, C≡O stretch frequency blue shifts with decreasing coordination number, therefore the frequency on defect/step sites is higher than the frequency on terrace sites. However, on platinum the opposite is observed, *i.e.* a red shift in the frequency with decreasing coordination number of the metal atom. The red shift of the C≡O stretch frequency with decreasing coordination number agrees well with theoretical models of CO chemisorption (Section 2.3).

Albeit the trend of C≡O stretch frequency observed on copper and gold, it is experimentally well established that on copper the C≡O stretch frequency blue shifts with decreasing coordination number and increasing CO binding energy [96–98]. Even though, the origin of this phenomenon is not well understood yet, early cluster model studies have suggested that frequency shift of CO adsorbed on copper also depends on the “wall effect” [99, 100]: With increasing CO binding energy, the bond distance between metal and CO decreases. With decreasing CO-metal bond length, C≡O bond oscillates at a higher rate as it feels a higher degree of repulsion from the charge distributed on the metal surface and this blue shifts the C≡O stretch frequency. The overall C≡O stretch frequency shift depends on the balance between the hybridization between CO $2\pi^*$ and metal d -bands and the “wall effect”. Additional theoretical and experimental efforts will be useful to more fully understand the blue shift of the C≡O stretch frequency with increasing CO binding energy observed on copper and gold.

2.5 Dependence of the C≡O Stretch Frequency on CO Coverage

In addition to the chemisorption energy, the C≡O stretch frequency is further influenced by the coverage of CO on the metal catalyst. Indeed, the changes of C≡O stretch frequency are a complex function of CO coverage and the distance between CO molecules. There

are two main mechanisms that affect the C≡O stretch frequency at saturation coverage: (1) Dynamical dipole coupling and (2) chemical interactions [80, 101]. The following paragraphs provide a concise discussion about dynamical dipole coupling and chemical interactions, which are of critical importance for the accurate interpretation of the C≡O stretch frequency of adsorbed CO on metal catalysts.

2.5.1 Dynamical Dipole Coupling

Dynamical dipole coupling induces frequency shifts and intensity transfer in the spectrum. Dynamical dipole coupling among adsorbed CO molecules can be described by the following Hamiltonian (in units of cm^{-1}) [102]:

$$H = \sum_{i=1}^n H_{ii} + \sum_{i<j}^n V_{ij} \quad (2.7)$$

where H_{ii} are the frequencies of the CO molecules in the absence of coupling (singletons) and V_{ij} is a function of the dynamical dipoles of the CO molecules, μ_i , and the distance between two CO molecules, r_{ij} ; *i.e.* $V_{ij} = f(\mu_i, \mu_j, r_{ij}^{-3})$. The average distance between CO molecules depends on their distribution among the available surface sites and on the absolute CO surface coverage. Because of the interaction term V_{ij} , the CO oscillators are no longer isolated, but are coupled to each other.

Diagonalization of H yields the new normal modes of the coupled system which results in a higher and a lower frequency compared to the singleton frequency as shown in Figure 2.8(A). The most intense modes of the coupled system are those in which the CO molecules oscillate in-phase: The low frequency mode is IR inactive as this has anti-phase oscillations (peaks in green dashed lines in Figure 2.8(A)), and the higher frequency mode is IR active with in-phase oscillations (peaks in dark blue solid and light blue dashed lines in Figure 2.8(A)). Due to these strong coupling effects, the integrated band area of CO

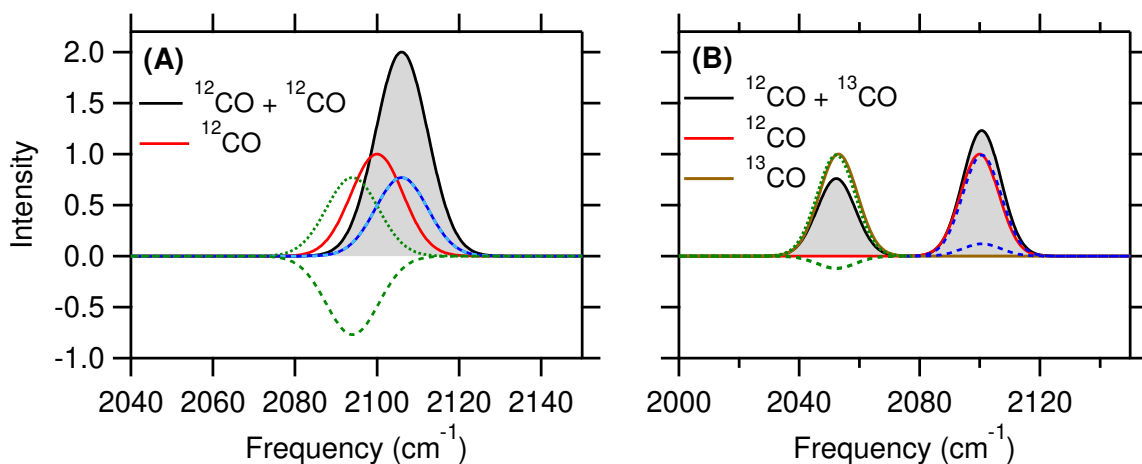


Figure 2.8: Dipole coupling between two (A) identical ¹²C¹⁶O and (B) ¹²C¹⁶O and ¹³C¹⁶O molecules (The model described in Ref [80] was used to get the normal modes and corresponding intensities). Singleton frequencies of ¹²C¹⁶O and ¹³C¹⁶O are 2100 and 2053 cm⁻¹, respectively [80]. Green dashed lines show the amplitude and phase of the two new normal modes at lower frequency. Dark blue solid and light blue dashed lines show the amplitude and phase of the two new normal modes at higher frequency. The addition of the amplitude and phase of each normal mode at corresponding frequencies gives rise to the observed IR band due to dynamical dipole coupling (black solid line with shaded area). A Gaussian distribution of the CO populations were simulated using an arbitrary line width.

adsorbed on metal catalysts does not follow Beer's law and does not reflect the true concentration of adsorbed CO (*e.g.*, Borguet *et al.* have shown that on a stepped Cu surface, beyond 0.2 monolayer (ML), the integrated intensity deviates from Beer's law [103]).

Isotopically different CO molecules are used to decrease the effect of dynamical dipole coupling. Coupling between isotopically different CO molecules gives rise to two IR bands with minimal frequency shifts compared to their singleton frequencies (Figure 2.8(B)). However, coupling between isotopically different CO molecules is incorporated with a significant spectral intensity transfer from the low to the high frequency band (a 24% of intensity transfer from ^{13}CO to the ^{12}CO is reported with coupling between ^{13}CO and ^{12}CO [80] as manifested in Figure 2.8(B)). As a result of dynamical dipole coupling, in the case of Cu or Au surfaces, it is expected that intensity transfers from CO adsorbed on terrace sites to CO adsorbed on defect (step, kink, edges) sites. Borguet *et al.* have shown that only 7% of the CO adsorbed on step sites dominates the $\text{C}\equiv\text{O}$ stretch band compared to the remaining 93% of CO adsorbed on terrace sites on copper due to dynamical dipole coupling [103]. Additionally, the fact that CO adsorbed on step sites dominates the spectra at saturation coverage was experimentally demonstrated in an electrochemical context [98].

2.5.2 Chemical Effects

Chemical interactions (or chemical effects), which are the second factor related to the CO coverage that influences the $\text{C}\equiv\text{O}$ stretch frequency, occur through changes in electronic distribution between metal and adsorbed CO molecules. These changes influence bond strength between CO and metal with increasing coverage (a detailed description is given in the Section 2.4). The direction of the $\text{C}\equiv\text{O}$ stretch frequency shift, *i.e.*, red shift or blue shift, due to chemical effects depends on the type of the underlying metal catalyst: On copper, chemical effects induce a red shift [101] on the $\text{C}\equiv\text{O}$ stretch frequency while on

palladium they blue shift the frequency [94].

Although the origin of the chemical effects is still under debate, there are attempts to explain this through the adaptation of the degree of electron filling in σ or π bonding between CO and metal with increasing CO coverage [101, 104].

Woodruff *et al.* [101] have proposed a model which follows the Blyholder and HMN models. As illustrated in the HMN model (a description of the HMN model is given in the Section 2.3), the CO $2\pi^*$ orbital splits into bonding and anti-bonding molecular orbitals due to the interaction with the d -band of the transition metal. With increasing coverage a broadening of the the $2\pi^*$ bonding orbital was suggested. Woodruff *et al.* have suggested that the relative energy level of the CO $2\pi^*$ bonding orbital with respect to the Fermi level of the metal defines the degree of electron filling which determines the strength of the C \equiv O bond. They proposed two scenarios are: (1) When the energy of the CO $2\pi^*$ bonding orbital is lower than that of the Fermi level, the degree of electron filling to the broaden $2\pi^*$ bonding orbital decreases with increasing CO coverage, resulting in a weakening of CO-metal bond and thus a blue shift in C \equiv O stretch frequency. (2) When the energy of the CO $2\pi^*$ bonding orbital is higher than that of the Fermi level, the degree of electron filling to the broaden $2\pi^*$ bonding orbital increases with increasing CO coverage, resulting in a strengthening of CO-metal bond and thus a red shift in C \equiv O stretch frequency. In the case of copper, it has been shown that the energy level of the $2\pi^*$ bonding orbital is higher than that of the Fermi level of the metal. Accordingly, on copper with increasing CO coverage, C \equiv O stretch frequency red shifts due to chemical effects. Even though this theory can explain the observed red shift in the C \equiv O stretch frequency of CO adsorbed on copper with increasing coverage, further investigations should be carried out to prove or disprove this model and to gain a better insight into the origin of the chemical effects.

2.6 Electrochemical Double Layer

In the 19th century, with his studies about the charge distribution of conductors, Helmholtz put forward the concept of the "electrochemical double layer (EDL)" [105]. At the boundary of two chemically distinct phases, such as a solid/liquid interface, equilibration of the chemical potentials lead to a potential drop across the interface [106, 107]. Further during electrocatalysis, applied potential, pH, chemical nature of the cations and anions in the electrolyte, and the properties of the electrode influence the arrangement of the ions at the electrolyte side of the interface [22, 106, 108]. In addition, interfacial water structure and surface adsorbed intermediates can modulate the properties of electrochemical interface [22, 29, 109–111]. As a result, electrode/electrolyte interfaces possess a complex nature as depicted in Figure 2.9 [22, 29, 109–111].

Early theoretical models that describe the EDL include (1) Helmholtz [105, 106], (2) Gouy-Chapmann (GC) [106], and (3) Gouy-Chapmann-Stern (GCS) models [106]. These classical theories present a primitive description of the double layer. However, it is important to have precise knowledge of these classical theories (Sections 2.6.1 and 2.6.2). Subsequent experiments were carried out by Grahme [112], Bockris [113] and Delahay [114] to further elucidate the structure and properties of the EDL. Recent explorations of the EDL employing modern experimental tools such as X-ray techniques [115, 116], vibrational Stark spectroscopy [29, 109, 117–119], scanning tunneling microscopy (STM) [120, 121] and theoretical calculations [122, 123] have further contributed to the understanding of the complex double layer structure under various conditions.

2.6.1 Helmholtz Model

The Helmholtz model assumes that the amount of the excess negative charge on the metal electrode is neutralized by the presence of an equal amount of positive charge at the elec-

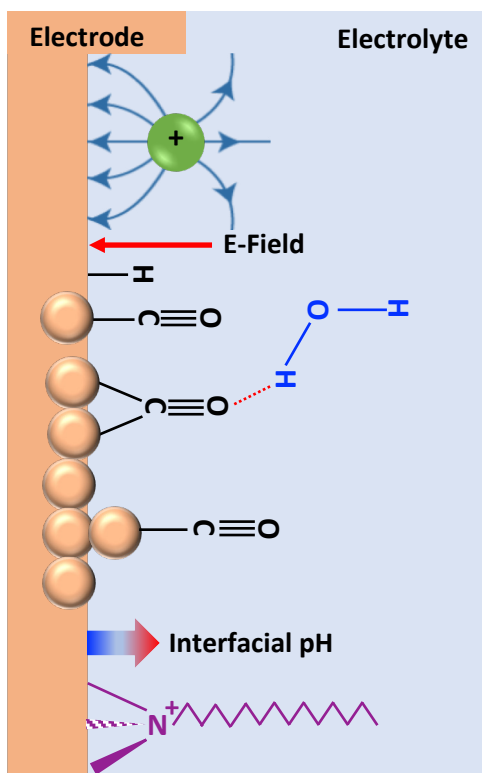


Figure 2.9: A simplistic view of an electrochemical double layer during an electrocatalytic process. Local electric field, interfacial pH, solvation environment, and proton donation can be influenced by adsorbed cations on the electrode, the interfacial water structure, anions near the interface, or other adsorbed molecular species. These characteristics can in turn can modulate the activity and selectivity of catalytic processes.

trolyte side [106]. The excess ions in the electrolyte form a compact layer at the surface of the metal as depicted in Figure 2.10(A). The closest distance from the metal surface where electrostatically adsorbed, solvated cations can be found is known as the “outer Helmholtz plane (OHP)”. A refined view of the Helmholtz model includes specifically adsorbed ions that form the “inner Helmholtz plane (IHP)” [106]. As a result of the formation of this compact layer of excess ions at the interface, the potential drops linearly across the interface as shown in Figure 2.10(A). The electrostatic description of the double layer structure in the Helmholtz model is the same as that of a parallel plate capacitor. Therefore, the relationship between the voltage (V) and the charge density (σ) can be expressed as [106]:

$$\sigma = \frac{\epsilon\epsilon_0}{d}V \quad (2.8)$$

where ϵ , ϵ_0 , and d are the dielectric constant of the medium, the permittivity of free space and the distance from the metal surface to the OHP. The differential capacitance of the double layer (C_{dl}) is [106]:

$$C_{dl} = \frac{\epsilon\epsilon_0}{d}. \quad (2.9)$$

This indicates that C_{dl} is constant and not a function of the applied potential. However, experimental evidence suggests otherwise, *i.e.* C_{dl} , varies with applied potential as well as with the concentration of the electrolyte [112]. Therefore, a more sophisticated model is needed to explain the true structure of the EDL.

2.6.2 Gouy-Champann-Stern (GCS) Model

This model depicts the EDL as a combination of a compact and diffuse layer as illustrated in Figure 2.10(B). The potential linearly drops over the compact layer and exhibits an exponential decay over the diffuse layer. The characteristic width of the diffuse layer

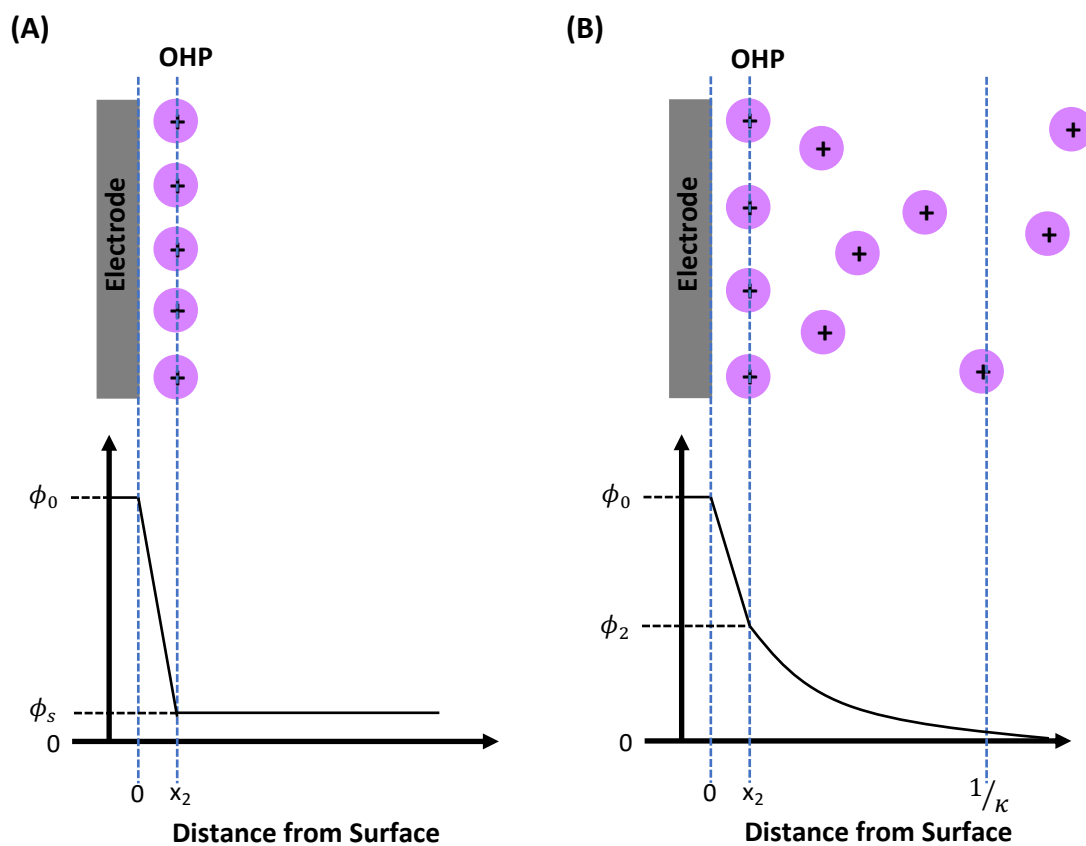


Figure 2.10: (A) Electrochemical double layer at a negatively charged metal/electrolyte interface as described by the Helmholtz model. Solvated cations form a compact layer near the surface of the metal electrode. The closest distance where solvated cations can be found is known as the OHP. (B) Electrochemical double layer structure proposed by the Gouy-Chapmann-Stern model, which consists of a OHP and a diffuse layer. The potential drop across the diffuse layer (ϕ_2) with respect to the potential at the bulk electrolyte is known as the zeta potential (ζ).

(Debye screening length) is given by $1/\kappa = 1/\sqrt{2F^2 z^2 c_0 / (\epsilon RT)}$ (Figure 2.10(B)) [106]. This indicates that the length of the diffuse layer decreases with increasing concentration of the electrolyte. Further, the capacitance of the diffuse layer is expressed as [106]:

$$C_{GC} = zF \sqrt{\frac{Dc}{2\pi RT}} \cdot \cosh\left(\frac{zF}{2RT}\zeta\right) \quad (2.10)$$

Here, z , F , D , c , R , T , and ζ represent the valency of ion, the Faraday constant, the dielectric constant, the concentration of the electrolyte, the gas constant, the absolute temperature, and the zeta-potential, respectively. Accordingly, the capacitance of the diffuse layer depends on both the concentration of the electrolyte and potential.

The combined capacitance of the compact and the diffuse layers defines the C_{dl} in the GCS model [106].

$$\frac{1}{C_{dl}} = \frac{1}{C_H} + \frac{1}{C_{GC}} \quad (2.11)$$

where C_H and C_{GC} are the capacitances of the Helmholtz plane and the diffuse layer, respectively. The Debye length decrease with increasing concentration as this depends on $\frac{1}{\sqrt{c_0}}$. Therefore, at high concentration of electrolytes (> 0.5 M) the potential drop mainly occurs over the Helmholtz plane. Further, for large charge densities ($|\phi_2| \geq 50/z$ mV) the potential drop cannot be explained as an exponential decay. Thus, the potential drops linearly over the compact part of the double layer.

2.6.3 Electric Field at an Electrochemical Interface

As a result of the potential drop across the EDL, an electric field is created at the interface. The electric field strength at the Helmholtz plane ($\vec{\mathcal{E}}$) can be expressed as:

$$\vec{\mathcal{E}} = -\frac{dV}{dx_2} \quad (2.12)$$

where dV and dx_2 are the potential drop over the Helmholtz plane and the position of this plane from the electrode surface, respectively. The strength of the electric field at the EDL influences the activity and selectivity of electrocatalytic processes [124, 125]. For a given applied potential, $\vec{\mathcal{E}}$ can be modulated through variation of the width of the Helmholtz plane. Indeed, experimental demonstrations show that $\vec{\mathcal{E}}$ can be tuned with the use of differently sized cations [29]. Li *et al.* have used quaternary alkyl ammonium cations with increasing chain lengths (methyl₄N⁺, ethyl₄N⁺, propyl₄N⁺, butyl₄N⁺) to modulate the electric field strength at the EDL during CO reduction reaction [29].

2.7 Stark Effect

The determination of the interfacial electric field during an electrocatalytic process can provide useful insight in understanding the parameters that influence the catalysis. Spectroscopic probes can be used to directly measure the strength and spatial distribution of the local electric field at the interface during a catalytic reaction. The vibrational Stark effect has emerged as a powerful molecular probe of the strength of the interfacial electric field [29, 109, 119, 126–128].

The vibrational Stark effect provides the dependence of the frequency shift of a vibrational mode associated with a dipole on the interfacial electric field [129]. Consider surface-adsorbed CO (CO_{ads}) as a molecular probe. When CO_{ads} is used as a molecular probe of an electrocatalytic interface, the vibrational Stark effect, *i.e.*, the potential dependence of the C≡O stretch frequency ($\omega(\phi)$) on the interfacial electric field ($\vec{\mathcal{E}}(\phi)$) can be expressed as [29]:

$$\omega(\phi) = \omega_{\text{PZC}} - \Delta\vec{\mu} \cdot \vec{\mathcal{E}}(\phi) \quad (2.13)$$

where ω_{PZC} is the C≡O stretch frequency at the potential of zero charge (*i.e.* in the ab-

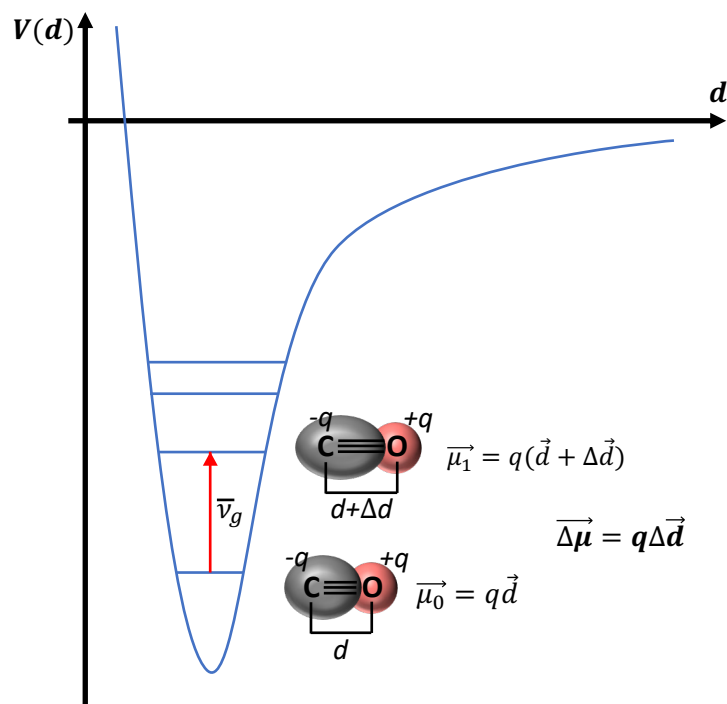


Figure 2.11: Anharmonic potential curve of CO molecule. Dipole moment of CO in the first vibrational excited state ($\vec{\mu}_1$) is slightly larger than that in the ground state ($\vec{\mu}_0$) as the length of the CO molecule is slightly larger in the excited vibrational state. Here q represents the charge. The difference in the dipole moment ($\Delta\vec{\mu}$) gives rise to a shift in the vibrational frequency of CO ($\Delta\nu$) in the presence of an externally applied electric field ($\vec{\epsilon}(\phi)$) with the relationship $\Delta\nu = -\Delta\vec{\mu} \cdot \vec{\epsilon}(\phi)$. Adapted with permission from Ref [129]. Copyright 2015 American Chemical Society.

sence of an interfacial electric field) and $\Delta\vec{\mu}$ is the change in the dipole moment between ground state and vibrationally excited state. $\Delta\vec{\mu}$ is known as the vibrational Stark tuning rate which is given in the units of $\text{cm}^{-1}/(\text{V cm}^{-1})$. Anharmonicity of the CO molecule causes a change in the bond length of $\text{C}\equiv\text{O}$ from ground state to vibrationally excited state (Figure 2.11). This change in the $\text{C}\equiv\text{O}$ bond length causes a change in the dipole moment and thus results in the vibrational Stark tuning rate. The vibrational Stark tuning rate for a particular molecule can be calculated using theoretical methods, and $\Delta\vec{\mu}$ of CO adsorbed on a copper surface in vacuum has been determined to be $1.3 \times 10^{-6} \text{ cm}^{-1}/(\text{V cm}^{-1})$. Therefore, interfacial electric field ($\vec{\varepsilon}(\phi)$) during an electrocatalytic process can be directly calculated with the knowledge of ω_{PZC} using Equation 2.13.

2.8 Properties of the Electrochemical Double Layer Beyond the Electric Field

The electrochemical double layer has a complex structure during an electrochemical process as depicted in Figure 2.9 [29, 110, 111]. The strength of the local electric field at the interface can be further modulated by the adsorption of cations on the electrode. Indeed, a promotion of the CO reduction reaction on copper electrode has been observed in the presence of Cs^+ cation compared to the presence of Li^+ [49]. Gunathunge *et al.* have attributed this promotion of CO reduction to an increase in the local electric field which decreases the activation barrier for the reduction of CO [109]. The local pH is another important parameter of the EDL that affects the electrocatalytic reactions. The local pH can be altered by the adsorbed cations on the electrode [130], formation of organic thin films [110], solutions species present near the surface such as HCO_3^{2-} , to name a few. Further, the interfacial water structure plays a crucial role in determining the properties of electrocatalytic processes as this exerts control over proton donation, promotion of cou-

pling of surface adsorbed intermediates, and the solvation of ions present at the interface. Often, these EDL properties evolve with the applied potential. Therefore, a comprehensive understanding of EDL properties under *operando* conditions is essential to improve the activity and selectivity of catalytic processes that are enabled through electrochemical interfaces.

Chapter 3

Spectroscopic Observation of Reversible Surface Reconstruction of Copper Electrodes under CO₂ Reduction

3.1 Introduction

Electrochemical CO₂ reduction to hydrocarbons holds high importance in mitigating global warming and as an alternative sustainable route for fuel and commodity chemical synthesis [41, 131–136]. Additionally, CO₂ reduction stands out as an attractive solution for the intermittency problem of the renewable energy sources when it is powered by renewable energy [41, 131–136]. Copper is a prototypical catalyst for CO₂ reduction, because this is the only pure metal that can convert CO₂ into hydrocarbons with a high current density of $\approx 5 \text{ mA cm}^{-2}$ [134, 137]. However, electrochemical reduction of CO₂ on copper catalyst suffers from poor product selectivity due to simultaneous hydrogen evolution at negative potentials and also due to the production of an array of hydrocarbons (Khul *et al.* have detected 15 hydrocarbon products during electrochemical CO₂ reduction on polycrystalline copper electrode [10]). Further, a higher overpotential, a larger potential compared to the thermodynamic potential, is required to produce hydrocarbons [10, 138–140]. Therefore, the development of a commercially viable catalyst for CO₂ reduction requires improvements in product selectivity and overpotential. An in-depth understanding

of the molecular level picture of the electrochemical double layer under CO₂ reduction conditions is essential in achieving high selectivity towards hydrocarbons and in reduction of the overpotential.

Morphology of the copper catalyst exerts a profound effect in determining the activity and selectivity of CO₂ reduction reaction (CO₂RR) [41, 132, 141–144]. For instance, Loiudice *et al.* have shown that the product selectivity towards ethylene formation increases by 4 times when the size of the nano-cubes increases by 24 to 44 nm [145]. Since copper has a weak cohesive energy compared to other metals such as platinum, copper can easily undergo reconstruction during CO₂RR [45–47, 96]. The surface-adsorbed intermediates, local pH and applied potential can affect the surface reconstruction. Therefore, it is important to understand the morphological changes of the copper catalyst especially under reaction conditions, in order to understand the key factors that influence the activity and selectivity of CO₂RR.

Among many techniques, surface enhanced IR absorption spectroscopy in attenuated total reflection (ATR-SEIRAS) configuration show high potential as an *in-situ* probing technique of the electrocatalyst. Since surface adsorbed CO (CO_{ads}) is an on-pathway intermediate during CO₂RR this can be used as a molecular probe of the surface morphology during electrocatalysis [36, 64, 146]. Indeed, CO_{ads} is an ideal molecular probe of the surface morphology as the frequency of C≡O stretch band depends on the coordination number of the metal atom on which it is bound (Chapter 2, Section 2.4).

Herein, using ATR-SEIRAS we show that copper surface undergoes reversible surface reconstruction under CO₂/CO reduction reaction conditions. Surface reconstruction of copper gives rise to, surface-adsorbed CO stabilized nano-scale copper clusters. Formation of new copper clusters manifests it self by the appearance of a new IR band at a higher frequency. Our analysis further reveal that CO adsorbed more strongly on these new surface sites than on the initial surface sites that are available before the surface re-

construction.

3.2 Results

To probe the surface morphology of copper electrode during CO₂RR, IR spectra of atop-bound CO (CO_{atop}) was collected in 0.1 M KHCO₃ electrolyte saturated with carbon monoxide. Figure 3.1 shows the potential dependence of the C≡O stretch band of CO_{atop}. At potentials more positive than -0.8 V vs. standard hydrogen electrode (SHE), a band centered at $\approx 2050\text{ cm}^{-1}$ is observed. Unless noted otherwise, all the potentials in Chapter 3 are referenced against SHE. A second band centered at $\approx 2080\text{ cm}^{-1}$ is observed at potentials more cathodic than -0.8 V. These two bands can be modeled by two Gaussian functions as exhibited in Figure 3.1 by blue and red color traces, respectively. We label the IR bands appear at ≈ 2050 and $\approx 2080\text{ cm}^{-1}$ as the low frequency band (LFB) and the high frequency band (HFB). Figure 3.2 shows the integrated band area of LFB and HFB as a function of applied potential. Increment of the LFB band area occurs through a wider potential range, while a steep increment is observed for the HFB band. As shown in the gray color shaded area in Figure 3.2, the onset of the HFB band area occurs when the LFB band area has reached a significant magnitude ($\approx 100\text{ mOD cm}^{-1}$).

To investigate whether this trend observed in LFB and HFB is reversible, C≡O stretch spectra were collected at decreasing cathodic potentials after reaching -1.10 V during the first cathodic scan. Comparison of the spectra collected during cathodic and anodic scans show that the trend observed in LFB and HFB is reversible (Figure 3.3(A)). The agreement in the integrated band area of LFB and HFB during cathodic and anodic scans further confirms the potential dependence of LFB and HFB bands are reversible (Figure 3.3(B)).

When bicarbonate is used as the electrolyte during CO₂RR/CORR, carbonate or bicarbonate anions in the solution desorb from the catalytic surface with increasing cathodic

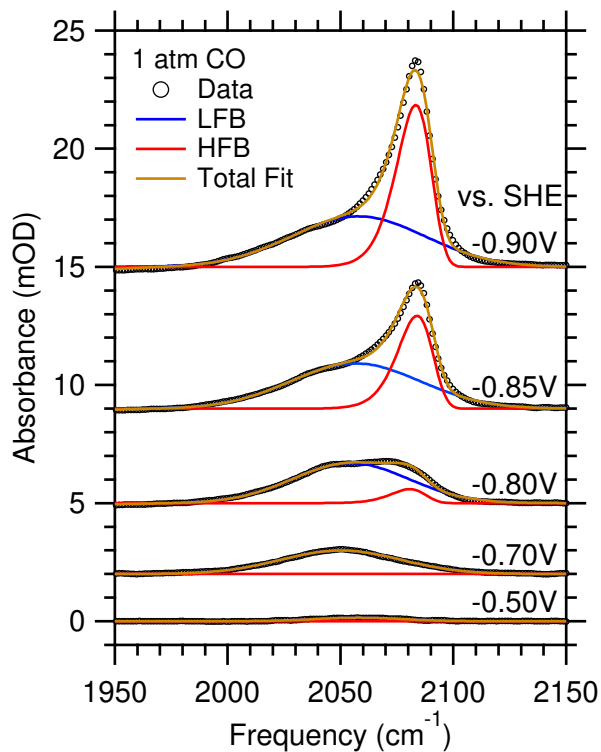


Figure 3.1: Potential dependence of C≡O stretch band of CO_{atop} on copper during CO reduction in 0.1 M KHCO₃ electrolyte. LFB and HFB traces show Gaussian fittings for low frequency band and high frequency band, respectively. Total fit is the summation of LFB and HFB. Reproduced from Ref [30].

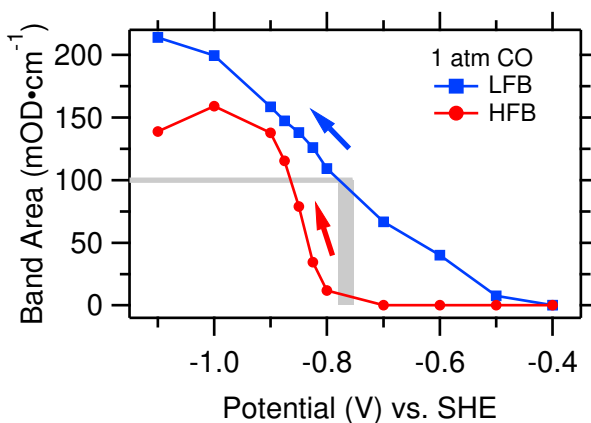


Figure 3.2: Potential dependence of the integrated band areas of LFB and HFB of the C≡O stretch band as shown in Figure 3.1. Reproduced from Ref [30].

potentials [147]. Desorption of these anions gives rise to a negative IR band $\approx 1540 \text{ cm}^{-1}$ as shown in Figure 3.4(A). Figure 3.4(B) shows the integrated band area of carbonate band. Interestingly, when overlap carbonate band area with the integrated band areas of LFB and HFB, it follows the trend of LFB. However, carbonate band area does not reflect the total CO_{atop} band area which is the summation of the band areas of LFB and HFB.

Kinetics of the LFB and HFB were explored by time resolved ATR-SEIRAS spectroscopy. IR spectra of $\text{C}\equiv\text{O}$ stretch band were collected during a potential step experiment from -0.70 to -1.10 V and holding the potential at -1.10 V. Figure 3.5(A) shows the time dependence of the $\text{C}\equiv\text{O}$ stretch spectra. At time < 0.4 s, LFB is observed $\approx 2050 \text{ cm}^{-1}$ and HFB is observed with increasing time. Figure 3.5(B) shows the integrated band area of LFB and HFB observed in Figure 3.5(A) as a function of time. Area of the LFB can be fitted by a double exponential function with time constants (τ) 0.3 and 1.3 s. In contrast, the HFB band can be fitted by a single exponential function with $\tau = 1.3$ s. This shows that both LFB and HFB has similar kinetics ($\tau = 1.3$ s) after HFB appears at ≈ 0.4 s. Further, this indicates that LFB and HFB are linearly related by:

$$A_{\text{HFB}} = m(E, \theta) \times A_{\text{LFB}} - b \quad (3.1)$$

where A_{HFB} and A_{LFB} are the integrated band areas of LFB and HFB, respectively. Factor $m(E, \theta)$ depends on the applied potential (E) and CO coverage (θ) while b is a constant. The inset of the Figure 3.5(B) shows A_{LFB} with $b = 100 \text{ mOD cm}^{-1}$ and $m = 1.4$.

3.3 Discussion

It is very well established that CO_{atop} adsorbed on copper electrodes give an IR band in the range of $\approx 2000\text{--}2100 \text{ cm}^{-1}$ [141, 146, 148, 149]. Further, CO_{atop} on highly-coordinated terrace sites of copper exhibits $\approx 30 \text{ cm}^{-1}$ lower frequency compared to the CO_{atop} on

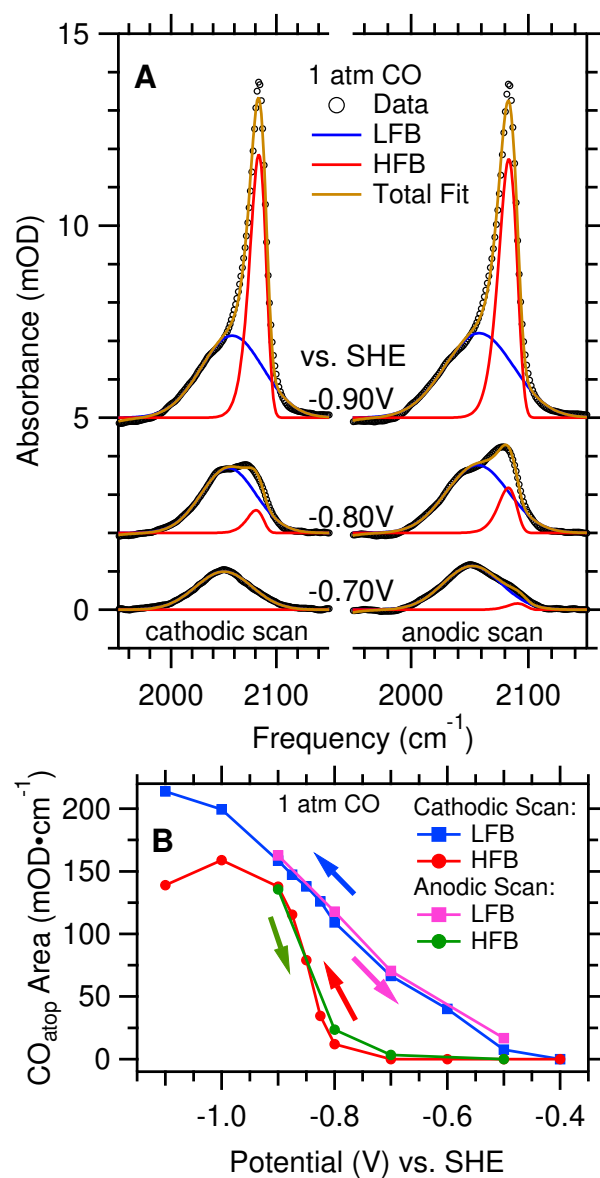


Figure 3.3: (A) Representative potential dependence of C≡O stretch spectra during a cathodic scan (left) and an anodic scan (right) after reaching the most cathodic potential of -1.1 V vs. SHE. LFB, HFB, and Total fit have the same meaning as in Figure 3.1. (B) Comparison of integrated band areas of LFB and HFB during cathodic and anodic scans. Reproduced from Ref [30].

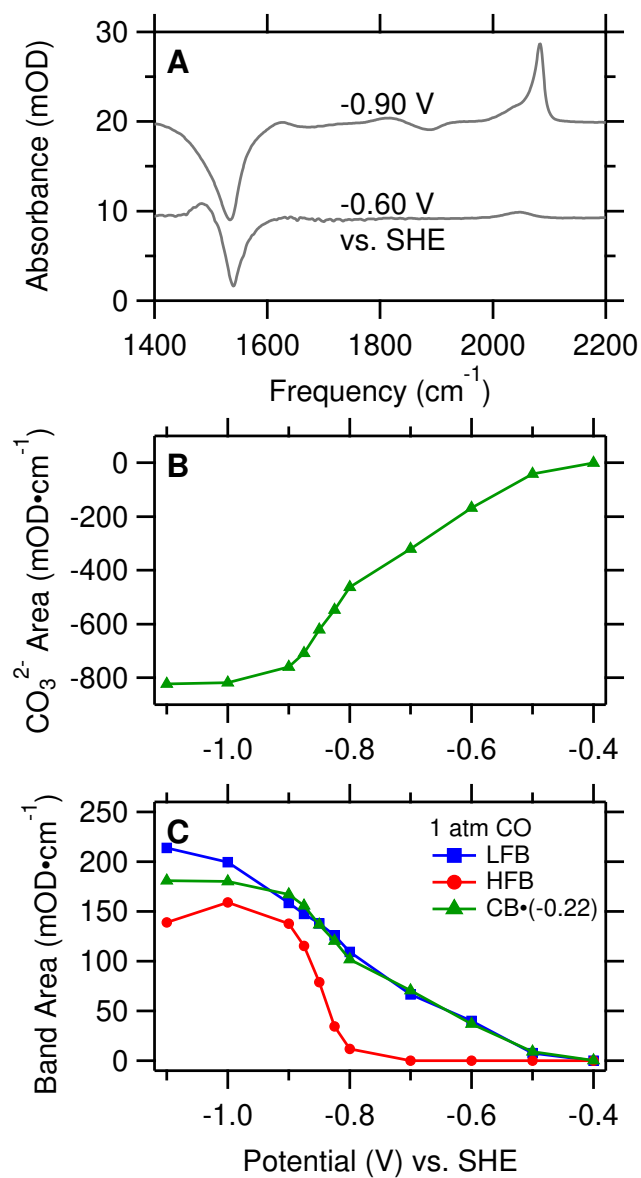


Figure 3.4: (A) Representative potential dependence of the carbonate and C≡O stretch bands. (B) Potential dependence of the integrated band area of carbonate band. (C) Comparison of the integrated band areas of LFB and HFB from Figure 3.2 and carbonate band (carbonate band area is scaled by -0.22 as indicated). Reproduced from Ref [30].

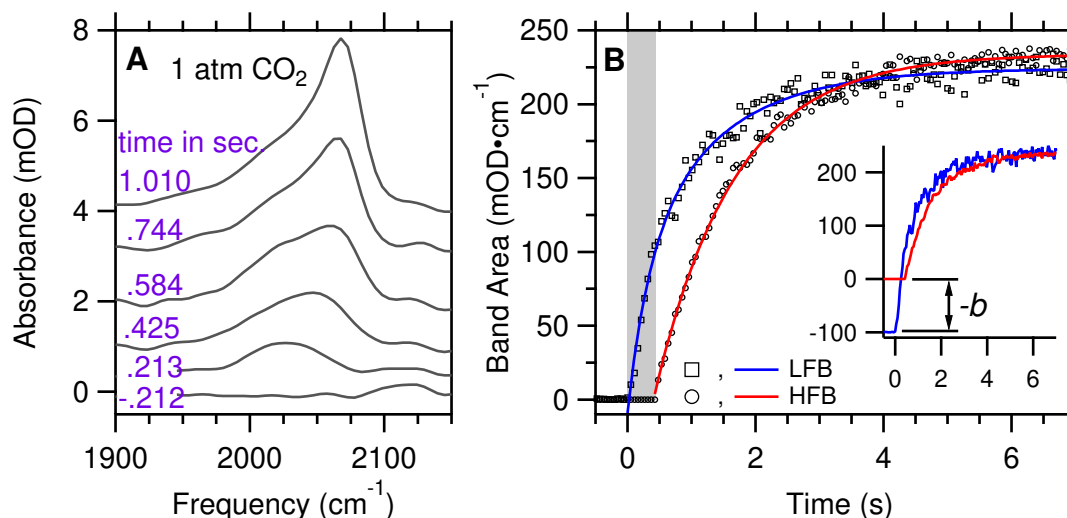


Figure 3.5: (A) Time evolution of C≡O stretch band during a potential jump from -0.70 to -1.10 V vs. SHE. (B) Integrated band areas of LFB (black circles) and HFB (black squares) of the spectra shown in (A). The exponential fittings for the LFB and HFB are shown in blue and red color traces, respectively. The inset shows the LFB multiplied by $m = 1.4$ and offset by $b = 100$ mOD cm⁻¹.

under-coordinated defect sites (A detailed description is given in Chapter 2, Section 2.3 and 2.4). For an instance, Hori *et al.* have shown that during electrochemical CO reduction, CO adsorbed on Cu(100) terrace sites show an IR band within 2040 – 2056 cm⁻¹ [97]. Koga *et al.* have investigated the IR spectroscopy of CO_{atop} during electrochemical CO reduction on stepped single crystal electrodes. With this study, Koga *et al.* have shown that CO_{atop} IR band appears $\approx 2080 \pm 8$ cm⁻¹. With that knowledge we assign the LFB and HFB bands (Figure 3.1) to CO_{atop} adsorbed on highly-coordinated terrace and under-coordinated defect copper sites, respectively.

The observed trends in the integrated band areas of LFB, HFB, and carbonate band and also the linear dependence of the integrated band areas of LFB and HFB can be explained by the following hypothesis of “Surface Reconstruction”. Following the literature precedence [45, 96], we propose that copper surface undergoes surface reconstruction during CO reduction reaction once the CO_{atop} has reached a threshold coverage. This reconstruction of the copper surface includes the formation of CO-stabilized under-coordinated

copper clusters. CO_{atop} adsorbed on these newly formed copper clusters gives rise to an IR band $\approx 2080 \text{ cm}^{-1}$.

Surface reconstruction hypothesis is validated by the following observations. First, as shown in Figure 3.2, HFB band only appears once LFB area has reached 100 mOD cm^{-1} area. This is further confirmed by the time resolved IR data shown in Figure 3.5(B). In addition, linear dependence of the integrated band areas of LFB and HFB given by Equation 3.1 is now apparent. When the potential is stepped to a -1.10 V , CO coverage increase with time. Once the CO coverage of LFB has reached the threshold coverage, which is $b = 100 \text{ mOD cm}^{-1}$, surface reconstruction takes place. After the surface reconstruction, HFB area increases as a function of potential and CO coverage ($m(E, \theta)$). The factor $m(E, \theta)$ describe the degree of surface reconstruction. Most importantly the data shown in Figure 3.3 demonstrated that this surface reconstruction is reversible.

Second, the linear decrease in the carbonate band does not follow the sudden substantial increase of the total CO_{atop} band area with the appearance of the HFB. This is because, HFB is a result of CO adsorbing on newly formed under-coordinated copper cluster with surface reconstruction. The absence of these newly formed surface sites before surface reconstruction, does not give a chance for carbonate to adsorb on these sites. Therefore, carbonate band area does not reflect the CO_{atop} band area increment with the appearance of HFB.

Third, observation of the broad LFB and a narrow HFB (Figure 3.1) further supports our hypothesis. On a polycrystalline copper surface there can be a combination of different terrace sites which gives away a broad width for the LFB. However, surface reconstruction can form sites with a particular coordination number. CO adsorbed on these newly formed sites with a particular coordination number, has a narrower band width representing the homogeneity of the surface sites.

Fourth, and the most powerful evidence comes from the surface-enhanced Raman scat-

tering (SERA) data collected on copper during CO reduction. Two bands at ≈ 360 and 280 cm^{-1} are simultaneously observed with the CO_{atop} band. These bands are assigned to Cu-CO stretch and frustrated rotation of CO_{atop} , respectively [150, 151]. A significant enhancement of these two bands are observed with the appearance of the HFB band. Further, the integrated band area of ≈ 360 and 280 cm^{-1} bands follows the trend of the integrated band area of HFB (Figures 6 and 7 of Ref [30]). These observations confirm the formation of nano-scale clusters with surface reconstruction that would enhance the SERS effect [152].

It is noteworthy to mention that the integrated band areas of LFB and HFB can be influenced by the dynamical dipole coupling between surface adsorbed CO (Chapter 2, Section 2.5). The effect of CO coverage on LFB and HFB are discussed in length in Chapter 5. Even though, dynamical dipole coupling exerts an effect on the integrated band areas of LFB and HFB, it fails to explain the SERS observation of intensity enhancement of ≈ 360 and 280 cm^{-1} bands. Surface reconstruction hypothesis, as described in the preceding paragraphs is the only effect that can explain the bulk of the observations.

3.4 Conclusions

By investigating the CO_{atop} IR band during CO reduction on copper, we show that copper catalyst undergoes reversible surface reconstruction during electrocatalysis. The surface reconstruction forms under-coordinated copper clusters within nano-meter scale. The adsorption energy of CO bound to these under-coordinated copper clusters are different from that of CO bound to highly-coordinated copper sites as exhibited by the different IR frequencies. We emphasize that this difference in binding energy of CO can be within 10 s of meV (Chapter 2, Table 2.1) which can give rise to a significant difference in the product selectivity and activity. Therefore, reversible surface reconstruction should be given a

higher attention in future CO₂RR/CORR studies.

3.5 Materials and Methods

Materials. NH₄F (40 wt.% in H₂O) and HF (48 wt.%) were purchased from Fisher Scientific. CuSO₄·5H₂O (99.999%; trace metals basis), Na₂EDTA (99.0–101.0%; ACS Reagent), 2,2-bipyridine (≥ 99%; ReagentPlus), HCHO (35 wt.%; 10% methanol as stabilizer), NaOH (99.99%; trace metals basis), and KHCO₃ (99.95%; trace metal basis) were acquired from Sigma Aldrich. Polycrystalline diamond pastes and alumina slurries were procured from South Bay Technologies (San Clemente, CA) or Electron Microscopy Sciences (Hatfield, PA). High purity water (18.2 MΩ cm) derived from a Barnstead Nanopure Diamond system (APS Water Services; Lake Balboa, CA) was used for all experiments. He (Ultra High Purity), CO (99.999%) were purchased from Air Gas.

Cu Thin Film Preparation. Reflecting plane of a 60° Si prism was polished successively with 6, 1, 0.5 μm diamond pastes for 5-10 min each. The polished surface was then rinsed under a constant stream of Nanopure water for ~ 10 min with a wet Kimwipe. Next, the Si prism was sonicated in water, acetone and water for 10, 5, and 5 min in each, respectively. Subsequently, The Si surface was etched by immersing the surface in an aqueous solution of 40 wt.% NH₄F (25° C) for 30 s. Prism was rinsed with Nanopure water before immersing it in a seeding bath for 1.5 min prepared with 750 μM CuSO₄ and 5 wt. % HF. Cu seeded Si surface was rinsed with Nanopure water. Then, this surface was immersed in a deposition bath of 0.25 M HCHO, 0.02 M CuSO₄, 20 mM Na₂EDTA, and 0.3 mM 2,2-bipyridine (pH~ 12, T= 54 – 55°C) for 3.5 min. The resistance across the Cu film deposited on the Si prism was measured (10-30 Ω). Si prism with the Cu film was assembled into the cell and it was blanketed with 4 mL of 0.1 M KHCO₃ electrolyte. The Cu film was cleaned using voltammetric cycles from –0.035 to –0.605 V vs. Ag/AgCl at

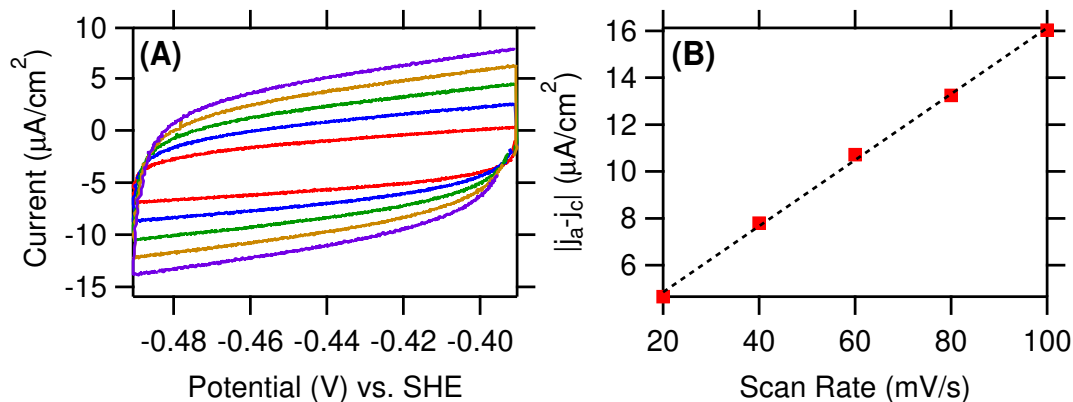


Figure 3.6: (A) Representative CVs collected at 20 (red), 40 (blue), 60 (green), 80 (yellow), and 100 (purple) mV/s scan rates to measure the double layer capacitance of the Cu film. (B) Red squares show the Double layer charging current vs. scan rate. Black dashed line is a fit to the data. The roughness of the Cu film was calculated by dividing the slope of the plot (B) by a factor of 2 and the double layer capacitance of a smooth Cu foil which is $28 \mu\text{F cm}^{-2}$ [153].

a scan rate of 50 mV/s in He saturated electrolyte. Roughness of the Cu film was measured by cycling the potential between -0.6 and -0.7 V vs. Ag/AgCl at scan rates of 20, 40, 60, 80, and 100 mV/s as shown in Figure 3.6. Measured roughness for Cu films is about 10-12 times higher than that of a smooth polycrystalline Cu foil.

ATR-SEIRAS Measurements. ATR-SEIRAS measurements were collected in the Krerschman configuration with a nitrogen-purged Bruker Vertex 70 FTIR spectrometer (Billerica, MA) equipped with an MCT detector (FTIR-16; Infrared Associates; Stuart FL). The FTIR instrument was interfaced with an ATR accessory (VeeMax III; Pike Technologies; Madison, WI) equipped with a customized electrochemical cell machined from polyetheretherketone (PEEK). Steady-state measurements were collected at 4 cm^{-1} spectral resolution and 40 kHz scanner velocity. The reference spectrum was recorded at -0.505 V vs. Ag/AgCl. The sample potential was reached by scanning the potential from reference potential at 10 mV/s scan rate. To ensure that the steady-state has reached, each potential was held for 60 s before collecting the spectrum. The change in the optical

density was calculated using the equation, $\Delta\text{mOD} = -10^3 \cdot \log(\text{SB}_S/\text{SB}_R)$, where SB_S and SB_R are sample single beam and reference single beam spectra, respectively.

Time-resolved FTIR measurements were carried out with a 16 cm^{-1} spectral resolution and a 160 kHz scanner velocity. The time resolution was $\approx 0.53\text{ s}$. Reference potential was applied for 60 s before stepping the potential to the sample potential which is triggered by the forward motion of the interferometer mirror. The first spectrum collected at the reference potential was used as the reference.

Electrochemical Methods for ATR-SEIRAS Measurements. Experiments were carried out in a single compartment cell. Figure 3.7 shows a schematic of the electrochemical cell with Pt wire counter electrode (99.95%; BASi Inc.; West Lafayette, IN), and leak-less Ag/AgCl reference electrode (ET072-1; eDAQ, Colorado Spring, CO). The Ag/AgCl electrode was calibrated against saturated calomel electrode (CHI 150; CH Instruments Inc.; Austin, TX) prior to each experiment. Electrochemical cell was cleaned in an aqueous acid solution (30 wt.% H_2SO_4 , 30 wt.% HNO_3) for one hour followed with sonication in Nanopure water for another one hour, prior to each experiment. Potential was applied using a VersaStat3 potentiostat and VersaStudio software (AMETEK; Berwyn, PA). Measured solution resistance was negligible for all the experiments.

3.6 Acknowledgements

We gratefully acknowledge the financial support by the National Science Foundation (award no.: 1565948). C. M. G expresses gratitude to Xiang Li and Paul Hicks for collecting and analysing SERS data. C. M. G. further thanks to Jingyi Li and Vincent Ovalle for their support in collecting SEIRAS data.

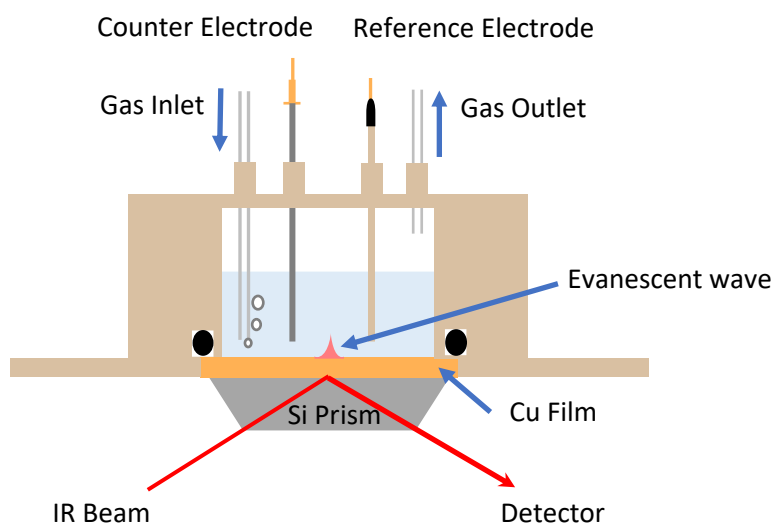


Figure 3.7: A schematic of the PEEK single compartment cell with the Pt counter electrode, leakless Ag/AgCl reference electrode and the thin Cu film as the working electrode.

3.7 Original Publication

This chapter has been published: Gunathunge, C. M.* , Li, X.* , Li, J., Hicks, R. P., Ovalle, V. J. & Waagele, M. M, *J. Phys. Chem. C* **121**,12337–12344 (2017). * These authors contributed equally to this work.

Chapter 4

Existence of an Electrochemically Inert CO Population on Cu Electrodes in Alkaline pH

4.1 Introduction

Chapter 3 demonstrates the utilization of surface-adsorbed CO (CO_{ads}) as a molecular probe of the dynamics of the copper catalyst under CO_2/CO reduction reaction ($\text{CO}_2\text{RR}/\text{CORR}$) conditions. Theoretical and experimental studies have shown that reduction of CO_{ads} is the potential limiting step in the CO_2 reduction reaction [133, 138, 154, 155]. Therefore, it is crucial to understand the electrochemical reactivity and surface diffusion of CO_{ads} on copper catalyst. CO can bind to catalyst surface in different configurations, such as atop-bound CO, 2-fold, 3-fold, 4-fold bridge-bound and hollow CO. These different binding configurations exhibits distinct $\text{C}\equiv\text{O}$ stretch frequencies as they are related with different CO binding energies (Chapter 2, Section 2.3, 2.4).

Density functional theory (DFT) calculations have shown these different binding configurations of CO on copper catalyst [42, 156, 157], although spectroscopic investigations have extensively studied atop-bound CO (CO_{atop}) [30, 146]. Therefore, it is often difficult to build up a correlation between the spectroscopic studies and theoretical studies to make inferences about the reactivity of CO_{atop} in different binding configurations. This calls

for the need of thorough experimental and DFT investigations of differently bound CO species.

In spectroscopy, C≡O stretch of the CO_{atop} on copper is observed in the frequency range of 2000 – 2100 cm⁻¹ [30, 146, 158]. Several spectroscopic studies have also reported an IR band in the frequency range of 1800 – 1900 cm⁻¹ which is attributed to the C≡O stretch frequency of bridge-bound CO (CO_{bridge}) [109, 146, 159, 160]. Nevertheless, a systematic investigation of the electrochemical reactivity and potential dependence of the CO_{bridge} has not been carried out. The presence of CO_{bridge} in spectroscopic studies is detected in alkaline pH. Interestingly, recent experimental studies have shown that the selectivity towards C₂₊ hydrocarbons is promoted in alkaline pH [161–165]. These observations bring about the following questions: (1) Is CO_{bridge} an on-pathway intermediate that produces C₂₊ hydrocarbons in alkaline pH? (2) Does CO_{bridge} modulate or effect the adsorption energies of CO_{atop} and/or hydrogen?

By employing surface-enhanced infrared absorption spectroscopy in attenuated-total reflection (ATR-SEIRAS) configuration and DFT calculations of copper/electrolyte interface in alkaline pH, we provide a comprehensive and systematic investigation of electrochemical reactivity and dynamics of CO_{bridge}. We show that, (1) CO_{atop} converts into CO_{bridge} below saturation coverage of CO. (2) Unlike CO_{atop}, CO_{bridge} is an irreversibly adsorbed species which can only be removed by the oxidation of copper catalyst. (3) CO_{bridge} does not affect the CO_{atop} coverage. This study highlights that the common notion of CO_{ads} is an on-pathway intermediate during CO₂ reduction reaction demands further investigation.

4.2 Results and Discussion

Potential Dependence of CO_{ads} and Assignment of CO Vibrational Bands.

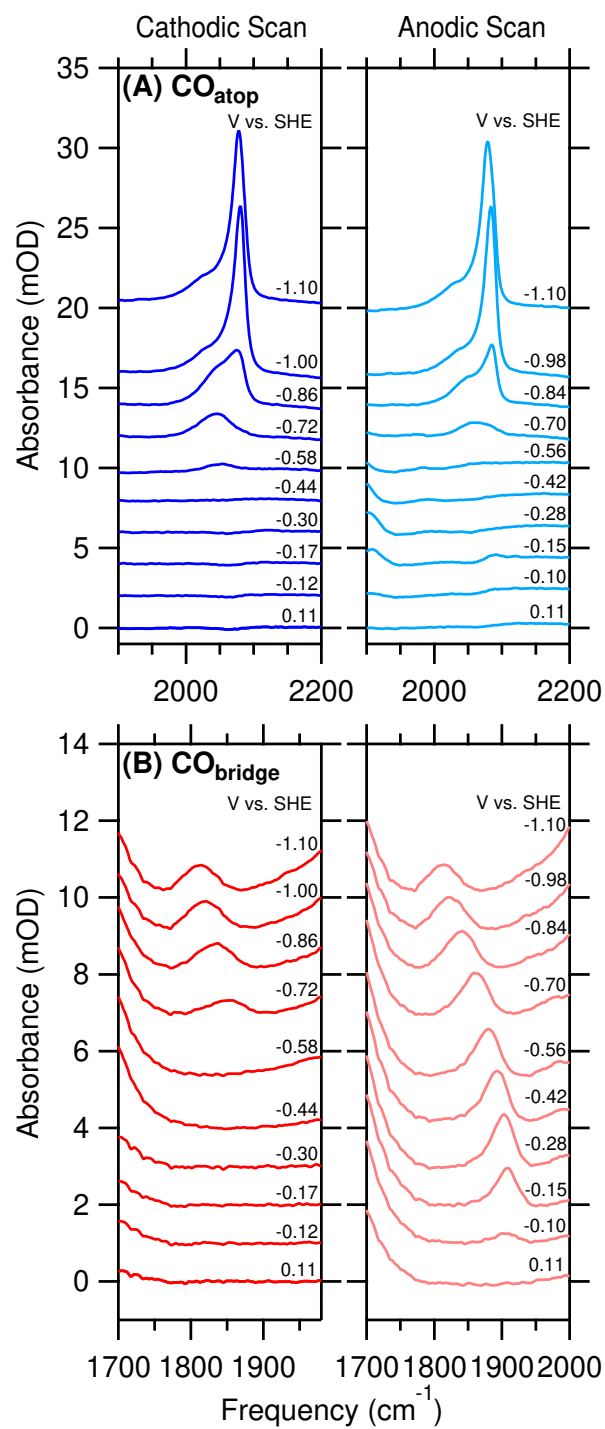


Figure 4.1: Representative IR spectra of the C≡O stretch mode of (A) CO_{atop} and (B) CO_{bridge} collected during a cyclic voltammetric scan in 0.05 M Li₂CO₃ (pH 11.4) at a scan rate of 10 mV/s. Cathodic forward and anodic reverse scans are shown in left and right panels, respectively. Reproduced from Ref [64].

To explore the potential dependence of the CO_{ads} on copper electrode surface-enhanced IR spectroscopy (SEIRAS) data were collected on a thin rough copper film deposited on a Si ATR prism using an electroless deposition method. Experiments were carried out in CO saturated 0.05 M Li_2CO_3 electrolyte by scanning the potential from 0.11 to -1.1 V vs. standard hydrogen electrode (SHE) at a scan rate of 10 mV/s. All the potentials in this Chapter are referenced against SHE, unless otherwise noted. Figure 4.1 shows the IR spectra collected during the cathodic forward scan and anodic reverse scan. $\text{C}\equiv\text{O}$ stretch mode observed in the frequency range $2000 - 2100 \text{ cm}^{-1}$ (Figure 4.1(A)) is due to atop-bound CO (CO_{atop}). Integrated band area of CO_{atop} is shown in Figure 4.2(A) in left ordinate. Agreeing well with the previous publications, CO_{atop} band area exhibits an onset potential ≈ -0.6 V and a good reversibility during forward and reverse scans [30, 146].

A second IR band is observed in the frequency range $\approx 1800 - 1900 \text{ cm}^{-1}$ and this is attributed to bridge-bound CO ($\text{CO}_{\text{bridge}}$). To unambiguously assign this IR band we have employed density functional theory (DFT) calculations. DFT revealed that the IR band in frequency regime $\approx 1800 - 1900 \text{ cm}^{-1}$ can be due to 3-fold bridge CO on Cu(111) and/or 2-fold bridge CO on Cu(100). Corresponding integrated band area is shown in Figure 4.2(A) in right ordinate. $\text{CO}_{\text{bridge}}$ shows a similar onset potential of -0.6 V as CO_{atop} . But unlike CO_{atop} , band area of $\text{CO}_{\text{bridge}}$ persist during the reverse scan until the copper surface is oxidized at -0.1 V.

Time and pH Dependencies of CO Populations.

To further investigate the dynamics and reactivity of CO_{atop} and $\text{CO}_{\text{bridge}}$ bands, potential polarization experiments were carried out. Electrolyte was saturated with CO while holding the Cu film at a potential of -0.5 V for 20 min. The potential was then jumped and held at -1.1 V for 25 min, which gives a saturation CO coverage [30, 109]. Integrated band areas of CO_{atop} and $\text{CO}_{\text{bridge}}$ during this time are shown in Figure 4.3(A) in gray color shaded area. CO_{atop} band area increases within few seconds and then stays

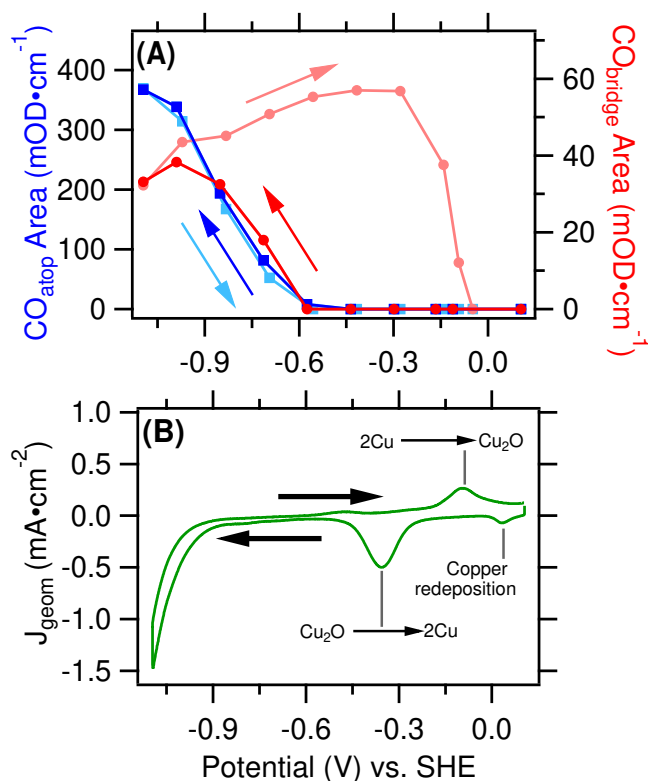


Figure 4.2: (A) Integrated band areas of CO_{atop} (left ordinate, blue color squares) and CO_{bridge} (right ordinate, red color circles) bands shown in Figure 4.1 as a function of applied potential. (B) Geometric current density during the potential scan (Geometric area of the Cu electrode is $\approx 1.9 \text{ cm}^2$). CV peaks are assigned according to the published data [42, 166]. Arrows indicate the direction of potential scan. Reproduced from Ref [64].

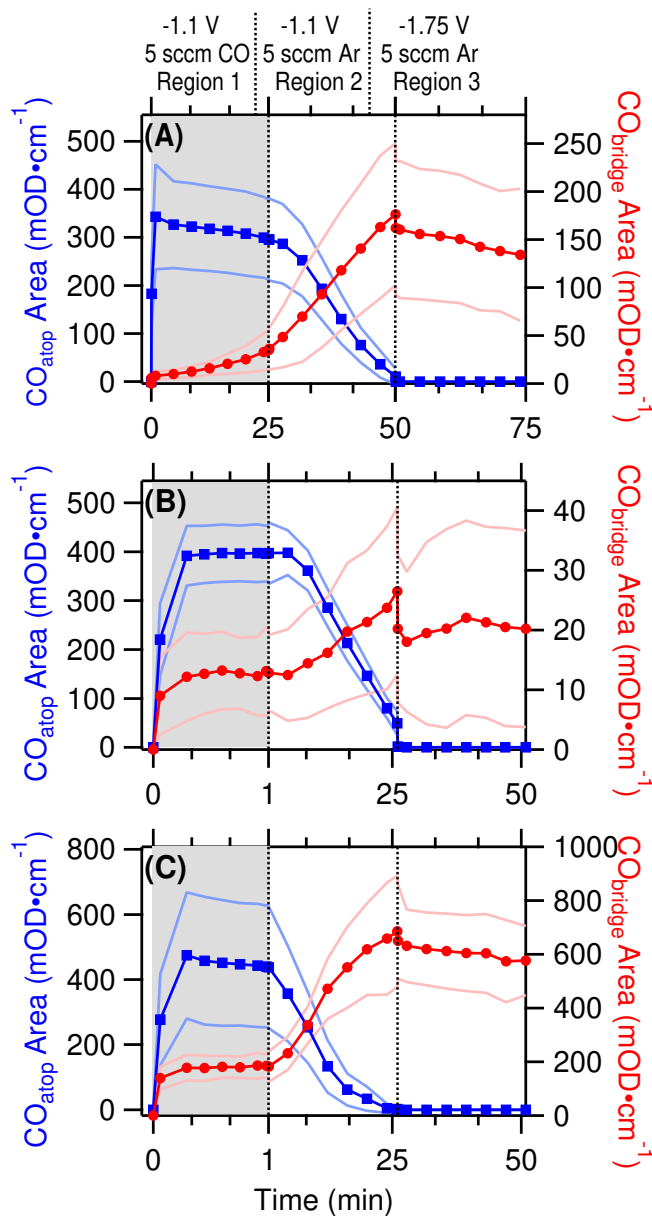


Figure 4.3: Integrated band areas of CO_{atop} (blue squares) and $\text{CO}_{\text{bridge}}$ (red circles) as a function of time during potential polarization experiments. Region1: -1.1 V potential with CO purging at 5 sccm rate. Region2: -1.1 V potential with Ar purging at 5 sccm rate. Region3: The potential was jumped and held at -1.75 V with Ar purging at 5 sccm rate. (A) and (B) Experiments were carried out in 0.05 M Li_2CO_3 (pH 11.4) with polarization times of 25 and 1 min in Region1, respectively. (C) Experiment was carried out in 0.1 M LiOH (pH 12.4) with a 1 min polrization time in Region1. Reproduced from Ref [64].

relatively constant during this period. $\text{CO}_{\text{bridge}}$ band area exhibits a minute increase up to $\approx 45 \text{ mOD cm}^{-1}$.

After initial 25 min, while holding the potential at -1.1 V , Ar gas was purged at 5 sccm rate (Figure 4.3(A) Region2). The amount of dissolved CO in the electrolyte decreases with Ar purging. Since, CO_{atop} is in dynamic equilibrium with the CO in the solution [36, 146, 159], CO_{atop} band area decreases with Ar purging. Yet, a gradual increase in the $\text{CO}_{\text{bridge}}$ is observed during this period. When the potential is jumped to -1.75 V (Figure 4.3(A) Region3), CO_{atop} band area goes to zero coverage while $\text{CO}_{\text{bridge}}$ band area remains relatively constant. These observations show that: (1) Below saturation coverage CO_{atop} converts into $\text{CO}_{\text{bridge}}$ species and (2) $\text{CO}_{\text{bridge}}$ is electrochemically inactive unlike CO_{atop} .

In order to acquire further information about the time dependence of CO_{atop} and $\text{CO}_{\text{bridge}}$ bands, the same experiment was carried out but with a decreased initial polarization time in Region1 from 25 to 1 min (Figure 4.3(B), gray color shaded area). The decrease in the initial polarization time has a great influence in the $\text{CO}_{\text{bridge}}$ band area as this only increases up to $\approx 25 \text{ mOD cm}^{-1}$ at the end of the Region2. This indicates that the conversion of CO_{atop} to $\text{CO}_{\text{bridge}}$ is driven by the changes of the interface that occur in tens of minutes scale. Hydrogen evolution can increase the interfacial pH during a cathodic polarization [167, 168]. In addition, spectroscopic studies of CO_{ads} on Ni, Co, and Pt have shown that $\text{CO}_{\text{bridge}}$ is favoured in alkaline pH [169–172].

To examine whether the increase in local pH has an effect on the formation of $\text{CO}_{\text{bridge}}$, we have carried out the experiment shown in Figure 4.3(B), now in 0.1 M LiOH which has a higher local pH of 12.4. Figure 4.3(C) shows the integrated band areas collected in 0.1 M LiOH electrolyte. 0.1 M concentration of LiOH is used in order to keep the concentration of the cation the same with 0.05 M Li_2CO_3 . Confirming our hypothesis that $\text{CO}_{\text{bridge}}$ population increases with increasing pH, $\text{CO}_{\text{bridge}}$ band area is 25 times higher in 0.1 M

LiOH compared to that in 0.05 M Li_2CO_3 at the end of the Region2.

Possible Origins of Observed CO Surface Dynamics.

We consider three possible origins to explain the conversion of CO_{atop} to $\text{CO}_{\text{bridge}}$ below saturation coverage of CO under cathodic polarization conditions. First scenario is an increase in the charge density of the electrode that favors the binding of $\text{CO}_{\text{bridge}}$ over CO_{atop} . It is shown that on Ni, Co, Pt, and Rh with increasing cathodic potential the preference towards $\text{CO}_{\text{bridge}}$ increases. This is because, with increasing cathodic potential back donation of electron from metal to $2\pi^*$ orbital of CO increases [170–173]. Since $\text{CO}_{\text{bridge}}$ has a higher back donation compared to CO_{atop} , the preference towards the bridge over atop is expected.

Increment in pH affects the potential of zero charge of the metal in SHE scale as; $E_{z,SHE} = E_{z,pH=0} - 0.059 \times pH$ [174]. Therefore, on the reversible hydrogen electrode (RHE) scale, potential of zero charge is invariant ($E_{z,RHE} = E_{z,SHE} + 0.059 \times pH = \text{constant}$). This dependence of the $E_{z,SHE}$ is due to the adsorption of hydroxide groups with increasing pH [174]. But, in the presence of CO, CO_{ads} replace adsorbed hydroxide and as a result $E_{z,SHE}$ is invariant with pH but $E_{z,RHE}$ shifts to more positive potentials with increasing pH [170–173]. Consequently, for a given applied RHE potential, the charge density at the electrode $\sigma = E_{RHE} - E_{z,RHE}$ increases with increasing pH. As described above, an increase in the charge density would prefer $\text{CO}_{\text{bridge}}$ over CO_{atop} .

This electrostatic description can not explain the surface dynamics that we observed in this study. First, same SHE potential is applied in all cases and if the preceding explanation is accurate, potential of zero charge should be constant. Accordingly, the surface charge density would not change for the same SHE potential. Second, under the assumption that $E_{z,SHE}$ follows the theoretical pH dependence, the charge density of the electrode would decrease with increasing pH.

The observed surface dynamics can also arise from a reconstruction of the Cu surface

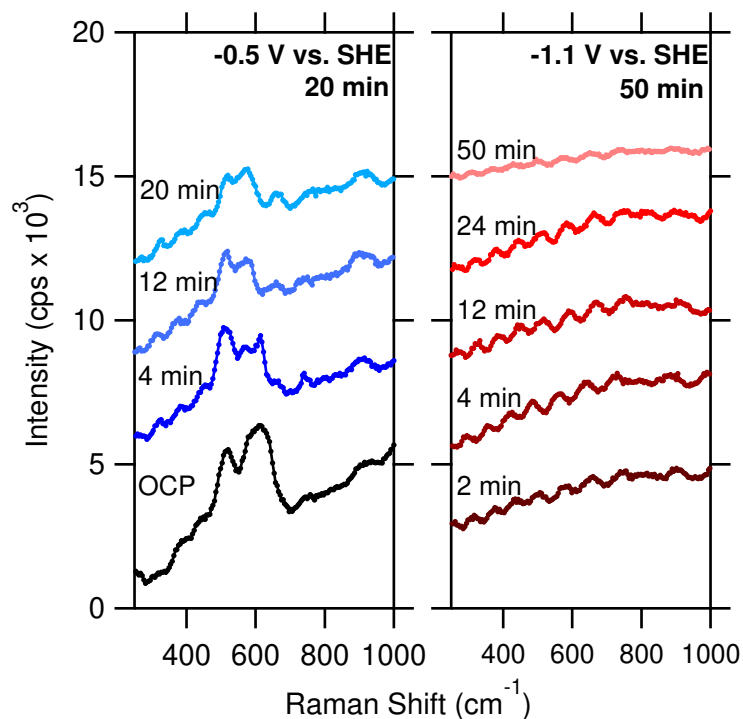


Figure 4.4: SERS data of Cu electrode in Ar-purged 0.05 M Li_2CO_3 at (A) -0.5 V and (B) -1.1 V. The black spectrum in (A) is collected at open circuit potential. Two major peaks at 517 and 610 cm^{-1} are assigned to Cu_2O . Reproduced from Ref [64].

under cathodic polarization. The slow reduction of surface adsorbed copper oxides can induce a reconstruction of the surface which can favor the binding of $\text{CO}_{\text{bridge}}$. To investigate the presence of surface adsorbed copper oxides, we have collected surface-enhanced Raman scattering (SERS) data on copper electrode in Ar-saturated 0.05 M Li_2CO_3 (Figure 4.4). SERS data show that after 2 min at -1.1 V copper oxides are absent on the surface. Therefore, reconstruction of copper with slow reduction of copper oxides can not be the reason that would give rise to the observed surface dynamics of CO_{ads} species.

Kim *et al.* have employed *in-situ* scanning tunneling microscopy to image the copper surface under cathodic polarization [46, 47]. They have observed that in alkaline pH with tens of minutes scale polycrystalline copper reconstruct to Cu(111) and then to Cu(100). Our data show that an increase in the local pH favors the binding of CO in bridge configuration. Taken together the most probable explanation for the observed CO population

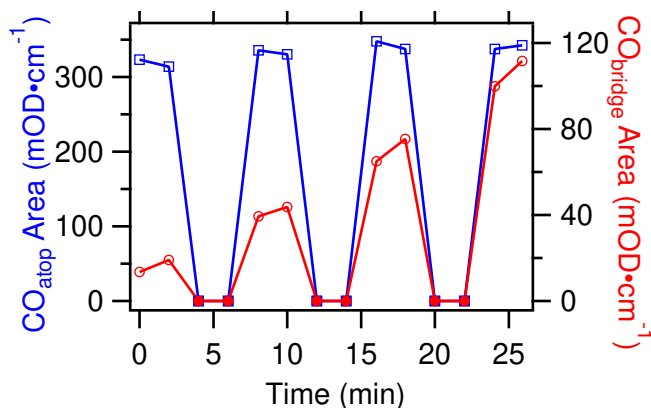


Figure 4.5: Integrated band areas of CO_{atop} (blue squares) and $\text{CO}_{\text{bridge}}$ (red circles) at the turning potentials of -1.1 and 0.11 V during consecutive CVs. Data were collected in CO-saturated 0.05 M Li_2CO_3 at a scan rate of 10 mV/s. Hollow and solid symbols represent the band area at -1.1 and 0.11 V, respectively. Reproduced from Ref [64].

dynamics is the pH induced surface reconstruction of copper. $\text{Cu}(100)$ and $\text{Cu}(111)$ sites formed during surface reconstruction can irreversibly bind CO in 2-fold or 3-fold bridge configurations.

Insensitivity of CO_{atop} Coverage to $\text{CO}_{\text{bridge}}$ Population.

Accumulation of irreversibly adsorbed $\text{CO}_{\text{bridge}}$ on the copper surface can influence the binding of CO_{atop} and hydrogen [50, 157]. To investigate this prospect, we have carried out consecutive CVs between 0.11 and -0.11 at a scan rate of 10 mV/s in CO-saturated 0.05 M Li_2CO_3 . Figure 4.5 shows the integrated band areas of CO_{atop} and $\text{CO}_{\text{bridge}}$ at turning potentials of the CVs. With increasing cycle number the $\text{CO}_{\text{bridge}}$ band area increases while the CO_{atop} band area persists. This observation demonstrates that the $\text{CO}_{\text{bridge}}$ population does not affect the binding energy or block the sites of CO_{atop} . This further manifests that the CO coverage on copper is much more less than an one monolayer coverage at this potential, as also shown by theoretical studies [50]. Further, CO_{atop} and $\text{CO}_{\text{bridge}}$ can adsorb on different surface sites. However, the narrowing of the $\text{CO}_{\text{bridge}}$ band with the removal of CO_{atop} (Figure 4.1) hints that these two species interact.

Origin of the Electrochemical Inertness of $\text{CO}_{\text{bridge}}$.

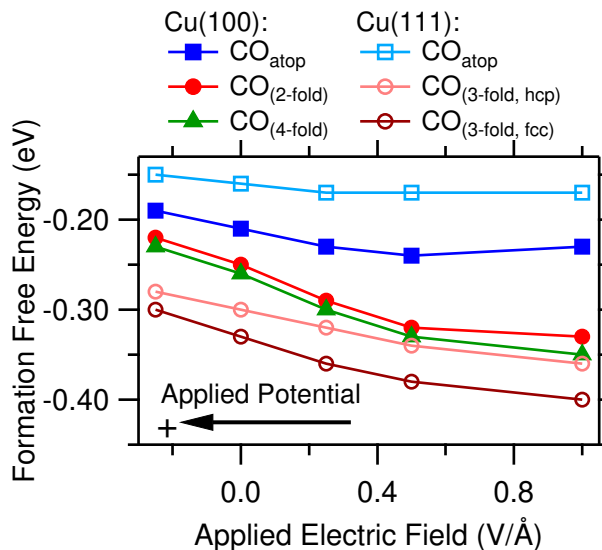


Figure 4.6: Formation energy of CO at different adsorption sites on Cu(111) and (100) as a function of applied electric field. A more positive electric field indicates that the potential has become more cathodic. Reproduced from Ref [64].

To examine the origin of the electrochemical inertness of the $\text{CO}_{\text{bridge}}$, we employed DFT calculations. Here, Cu(111) and (100) surface facets were used as model copper surfaces. Figure 4.6 shows the formation energy of CO_{atop} and $\text{CO}_{\text{bridge}}$ as a function of applied electric field. When the electric field is increased from -0.25 to 1 V/\AA° the formation energy of CO_{atop} stays approximately constant, while this becomes more negative for $\text{CO}_{\text{bridge}}$. This shows that the $\text{CO}_{\text{bridge}}$ becomes more stable with increasing cathodic potential.

Further, we calculated the activation barrier for the water-assisted hydrogenation of CO_{atop} and $\text{CO}_{\text{bridge}}$ to CHO (Figure 4.7). The calculated formation energy for the 2-fold or 4-fold CHO is invariant with applied electric field. Taken together, as shown in Figure 4.7, activation barrier for the formation of CHO from CO_{atop} does not depend on the applied electric field. In contrast, since the formation energy of $\text{CO}_{\text{bridge}}$ decreases with increasing electric field, the activation barrier for the production of CHO from $\text{CO}_{\text{bridge}}$ increases with increasing electric field/cathodic potential. Accordingly, the stabilization

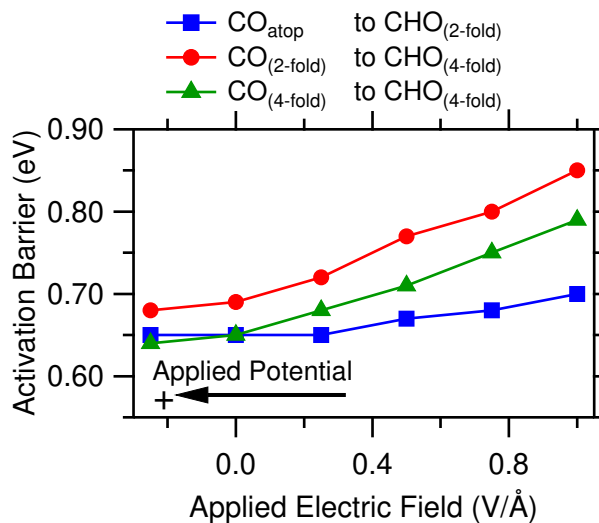


Figure 4.7: Activation barrier for the water-assisted hydrogenation of CO to CHO on Cu(100) as a function of applied electric field. A more positive electric field indicates that the potential has become more cathodic. Reproduced from Ref [64].

of CO_{bridge} with increasing cathodic potential can be the origin of the electrochemical inertness of CO_{bridge} on copper electrode.

4.3 Conclusions

Herein, we show that a bridge-bound CO population is observed on copper in alkaline pH under cathodic polarization that can be due to 3-fold bridge CO on Cu(111) and/or 2-fold bridge CO on Cu(100). pH induced surface reconstruction of copper electrode that occurs over a time scale of tens of minutes forms Cu(111) and (100) sites that preferentially and irreversibly bind CO in bridging configuration. In contrary to the shared understanding that the surface-adsorbed CO is an on-pathway intermediate during CO₂ reduction reaction, we show that CO_{bridge} is an electrochemically inactive species. The electrochemical inertness could arise from the stabilization of CO_{bridge} with increasing cathodic potential as shown by the DFT calculations. Even though, CO_{bridge} does not affect the CO_{atop} population, further experimental efforts are required to assess CO_{bridge}'s effect on product selectivity

during CO₂ reduction reaction.

4.4 Materials and Methods

Materials. NH₄F (40 wt% in H₂O), HF (48 wt%), and Li₂CO₃ (99.999%; trace metals basis) were purchased from Fisher Scientific. CuSO₄·5H₂O (99.999%; trace metals basis), Na₂EDTA (99.0-101.0%; ACS Reagent), 2,2-bipyridine (≤99%; ReagentPlus), HCHO (35 wt%; 10% methanol as stabilizer), NaOH (99.99%; trace metals basis), and LiOH·H₂O (99.95%; trace metals basis) were procured from Sigma-Aldrich. Polycrystalline diamond pastes were purchased from South Bay Technologies (San Clemente, CA) or Electron Microscopy Sciences (Hatfield, PA). Ar (Ultra High Purity) and CO (99.999%) were acquired from Air Gas. For all experiments, high purity water (18.2 MΩ cm) derived from a Barnstead Nanopure Diamond system (APS Water Services; Lake Balboa, CA) was used.

Cu Thin Film Deposition. Cu thin films were chemically deposited on a 60° Si ATR prism (Pike Technologies; Madison, WI) following a similar method described in Chapter 3. After the Cu film deposition, it was assembled to an electrochemical cell and blanketed with 4 mL of either 0.05 M Li₂CO₃ or 0.1 M LiOH. The electrolyte was then purged with Ar gas at 5 sccm for 20 min. Next, the Cu electrode was cleaned by cycling the potential between −0.13 to −0.6 V vs. Ag/AgCl at 50 mV/s scan rate. Following this, CVs were collected from −0.6 to −0.7 V at 20, 40, 60, 80, and 100 mV/s scan rates to determine the roughness factor of the Cu film (Details of the roughness factor determination of Cu thin films are given with the Figure 3.6).

Electrochemical methods for ATR-SEIRAS Measurements. Experiments were carried out in a single-compartment polyetheretherketone (PEEK) cell (Figure 3.7). The electrochemical cell was cleaned in an acid bath (30 wt% HNO₃ + 30 wt% H₂SO₄) for 1 hour

followed with sonication in Nanopure water for another 1 hour. A Au wire (99.999%, 0.5 mm thick, Alfa Aesar) and a Ag/AgCl (RE-5B, 3 M NaCl, BASi Inc., West Lafayette, IN) were used as counter and reference electrodes respectively. Potential was applied using a VersaStat3 potentiostat (AMETEK; Berwyn, PA). 85% of the solution resistance was compensated *in-situ*.

ATR-SEIRAS Measurements. ATR-SEIRAS measurements were collected with a nitrogen-purged Bruker Vertex 70 FTIR spectrometer (Billerica, MA) equipped with a liquid nitrogen-cooled MCT detector (FTIR-16; Infrared Associates; Stuart, FL). Spectra were collected with 4 cm^{-1} spectra resolution and 40 kHz scanner velocity. The change in the optical absorbance was calculated using the relationship; $\Delta mOD = -10^3 \log(S/R)$, where S and R represent the sample and reference single beam spectra, respectively.

SERS Measurements. SERS data were collected in a Horiba Scientific Xplora Raman microscope using a water immersion objective (NA = 1.0, WD = 2.0 mm; LUMPLFLN-60X/W; Olympus Inc.; Waltham, MA) wrapped in a 0.006 mm thick Teflon sheet with a drop of water interfacing the objective and the sheet. Excitation source was a 638 nm laser. Data were collected with 600 lines/mi as the grating, 300 μm hole, 100 μm slit, and an acquisition time of 25 s. Raman spectroscopy was calibrated with a Si as the standard prior to each experiment.

SERS were collected on a Cu film chemically deposited on a Si wafer. The Cu film was assembled in to a home-built Teflon cell. The cell was cleaned prior to each experiment following the cleaning procedure of the PEEK cell explained above. Then, a 50 mL of 0.05 M Li_2CO_3 was purged with Ar for ~ 30 min before the experiment. Cu film was electrochemically cleaned using the CV method described above. This was followed by the CV data collection for roughness factor determination. The Cu film was kept at open circuit potential for ~ 2 min before applying -0.5 V vs. SHE. The Raman spectra were collected at every 2 min while holding the potential at -0.5 V vs. SHE for 20 min. Then

the potential was jumped to -1.1 V vs. SHE and held at this potential for 50 min while collecting Raman spectra at every 2 min.

4.5 Acknowledgements

We gratefully acknowledge the financial support by the National Science Foundation (award no.: 1565948). C. M. G expresses gratitude to Vincent Ovalle for his support in data collection. C. M. G. further thanks Prof. Michael J. Janik and Dr. Yawei Li for carrying out DFT calculations.

4.6 Original Publication

This chapter has been published: Gunathunge, C. M., Ovalle V. J., Li. Y., Janik M. J. & Waegele, M. M, *ACS Catal.* **8**,7507–7516 (2018).

Chapter 5

Revealing the Predominant Surface Facets of Rough Cu Electrodes under Electrochemical Conditions

5.1 Introduction

Rough metal electrodes exhibit high catalytic activity and selectivity towards hydrocarbon formation, especially towards C_{2+} hydrocarbons, during electrocatalytic CO_2/CO reduction reaction ($CO_2RR/CORR$) [175–178]. For an instance, Hoang *et al.* have shown that Faradaic efficiency (FE) for ethylene formation is 40% on a rough copper nanowire catalyst at -0.5 V vs. reversible hydrogen electrode (RHE), while FE for ethylene formation is only 1% on a smooth polycrystalline copper catalyst at the same applied potential [177]. Electrodeposition [177, 179–181], reduction of copper oxide phases [43, 162, 178, 182–185], deposition of nanoparticles [145, 175, 186–188], usage of a porous support [189, 190], and halide induced surface reconstruction [163, 176, 191–194] are some of the techniques that are employed to prepare rough metal electrodes.

It is challenging to identify atomic level characteristics of rough metal electrodes that give rise to the observed high catalytic activity and selectivity under operating conditions. *In-situ* probing of the catalyst morphology can be achieved by employing powerful techniques such as electrochemical scanning tunneling microscopy (ESTM), *in-situ* X-

ray absorption spectroscopy (XAS), surface-interrogation scanning tunneling microscopy (SI-SEM), *in-situ* atomic force microscopy (AFM), surface-enhanced infrared absorption spectroscopy (SEIRAS) and, surface-enhanced Raman scattering (SERS). However, all the above mentioned techniques can not be used as routine procedures to probe atomic level morphology of rough metal electrodes. Yet, SEIRAS is an uncomplicated technique that has demonstrated it self as a powerful approach for the investigation of atomic level morphology when coupled with a suitable molecular probe, such as surface-adsorbed CO [36, 64, 146]. As elaborated in Chapter 3 and 4, C≡O stretch frequency of atop-bound CO (CO_{atop}) is an ideal probe of the atomic level morphology of rough metal electrodes as this frequency is influenced by the coordination number of the metal atom on which CO_{atop} is bound. Although, acute attention must be paid when interpreting the data observed during SEIRAS due to following factors.

Due to experimental constraints, such as stability of thin film metal catalysts, SEIRAS or SERS data were collected in short time scales (few minutes) compared to product detection electrolysis experiments (tens of minutes). Reconstruction of catalyst surface during pro-longed electrolysis [30, 46, 47] hinders the direct correlation of atomic morphology data collected using spectroscopic techniques to electrolysis data. Further, with increasing CO coverage the C≡O stretch frequency is influenced by the CO coverage effects, dynamical dipole coupling and chemical effects (Chapter 2, Section 2.5). Therefore, C≡O stretch frequency no longer reports on the atomic morphology of the catalyst with increasing CO coverage. But, the C≡O stretch frequency can be used as a probe of the atomic level morphology of the catalyst in the limit of low CO coverage. Even at low CO coverage, Cu(100) and Cu(111) give rise to a similar C≡O stretch frequencies albeit their different binding energies (Chapter 2, Table 2.1). Yet, Cu(100) exhibits good catalytic activity and selectivity towards ethylene, while Cu(111) shows a poor CO_2 reduction catalytic activity and selectivity [132, 195].

Herein, to overcome the above mentioned problems, we combine SEIRAS with differential electrochemical mass spectrometry (DEMS). Simultaneous observation of C≡O stretch frequency of CO_{atop} and onset potentials of products formed during the CORR, allows the formation of a rigorous connection between structure property and catalytic activity. We show that the potential dependence of the C≡O stretch frequency at low CO coverage limit is a powerful indicator of the atomic level morphology of rough metal catalysts.

5.2 Results and Discussion

Copper Thin-Film Electrodes.

Here, we investigate two distinctly prepared rough copper thin films that are frequently employed in SEIRAS studies. First film is a thin rough copper film deposited on a Si attenuated-total reflection (ATR) prism using an electroless deposition method (Cu-Si) [30, 146, 196]. Second film is a thin rough copper film electrochemically deposited on a gold underlayer on a Si ATR prism (CuAu-Si) [196–198]. Thickness of the copper film is ≈ 80 nm for Cu-Si measured using atomic force microscopy (AFM) images, and is ≈ 8 nm for CuAu-Si film measured by monitoring the charge passed during the electrochemical deposition of Cu on Au overlayer [198]. AFM images of Cu-Si (Figure 2.1) and CuAu-Si (Figure 5.1) films show that these films are made up of interconnected metal islands with ≈ 80 and ≈ 40 nm particle sizes, respectively. The roughness of the films measured using electrochemical capacitance measurements are ~ 10 and ~ 5 for Cu-Si and CuAu-Si films, respectively, compared to the roughness of a smooth polycrystalline Cu foil [153].

Even though, Cu-Si and CuAu-Si films are frequently used in SEIRAS studies, direct product detection of these two films were not carried out as these thin films tend to peel off with pro-longed electrolysis. Therefore, without any scientific basis, it is assumed that

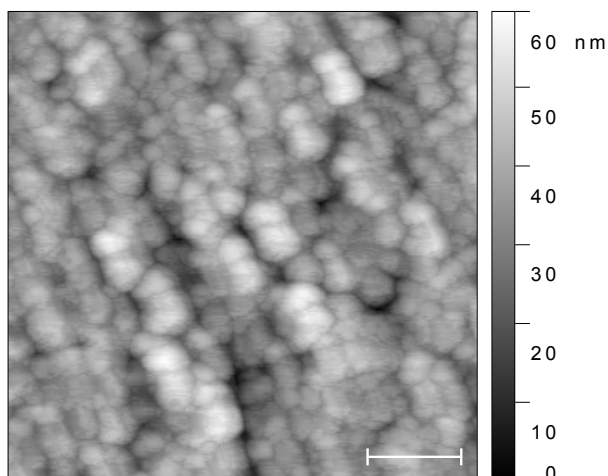


Figure 5.1: An AFM image of a CuAu-Si film. The scale bar is 200 nm. Image was acquired in a $1 \times 1 \mu\text{m}^2$ area with a Si cantilever (Nanosensors; Neuchatel, Switzerland; PPP-NCHR 10 M, 7 nm tip radius, 330 kHz resonance frequency, and 42 Nm^{-1} spring constant) at a 0.5 Hz scan rate in non-contact mode on a Park XE-100 AFM system (Park Americas; Santa Clara, CA). Reproduced from Ref [158].

these films possess similar activity and selectivity towards hydrocarbon production during $\text{CO}_2\text{RR}/\text{CORR}$ as copper foils which are more frequently used in electrolysis studies. Herein, we carried out product analysis on Cu-Si and CuAu-Si films by combining DEMS and SEIRAS.

Onset Potentials for CO Reduction Products on Cu-Si and CuAu-Si.

Figure 5.2 shows the combined DEMS and SEIRAS cell setup. Experiments were carried out in CO -saturated 0.1 M potassium phosphate at $\text{pH} \approx 7$. Before collecting DEMS and SEIRAS data, Cu thin films were subjected to three cyclic voltammograms (CVs) between -0.6 and -1.2 V vs. Ag/AgCl at 10 mV/s scan rate. Unless otherwise noted all the potentials in Chapter 5 are referenced against Ag/AgCl . These CVs were carried out to ensure the removal of copper oxides present on Cu thin films. The DEMS and SEIRAS data collection was carried out in CO -saturated electrolyte while scanning the potential from -0.6 to -1.8 V at 1 mV/s scan rate.

Figure 5.3 shows the partial current densities and the onset potentials for hydrogen,

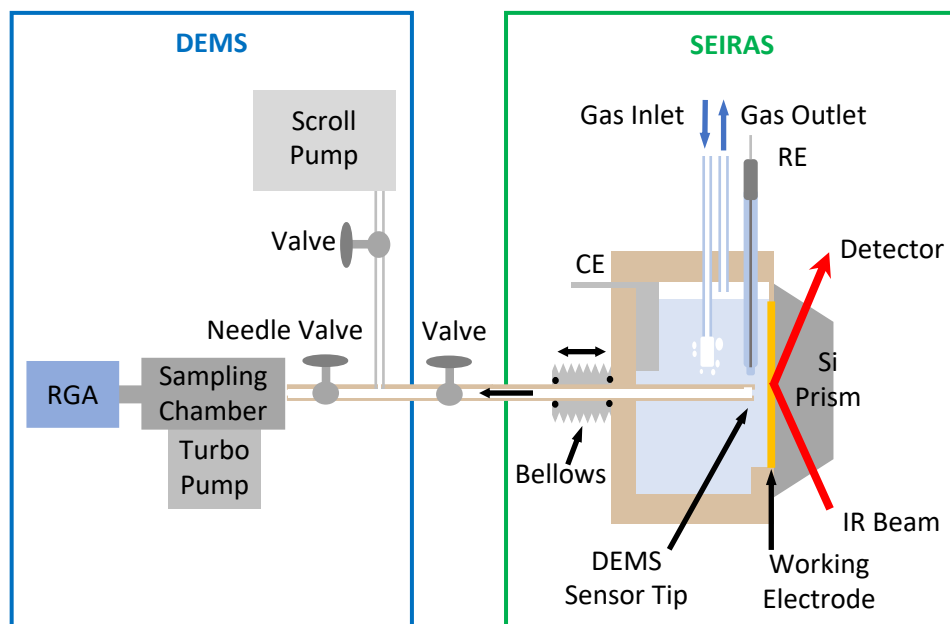


Figure 5.2: DEMS/SEIRAS setup. RGA, CE, and RE denote residual gas analyzer, counter electrode, and reference electrode, respectively. The sampling tip was inserted through a polytetrafluoroethylene (PTFE) bellows and connected to a micrometer, enabling the fine adjustment of the tip-electrode distance. Reproduced from Ref [158].

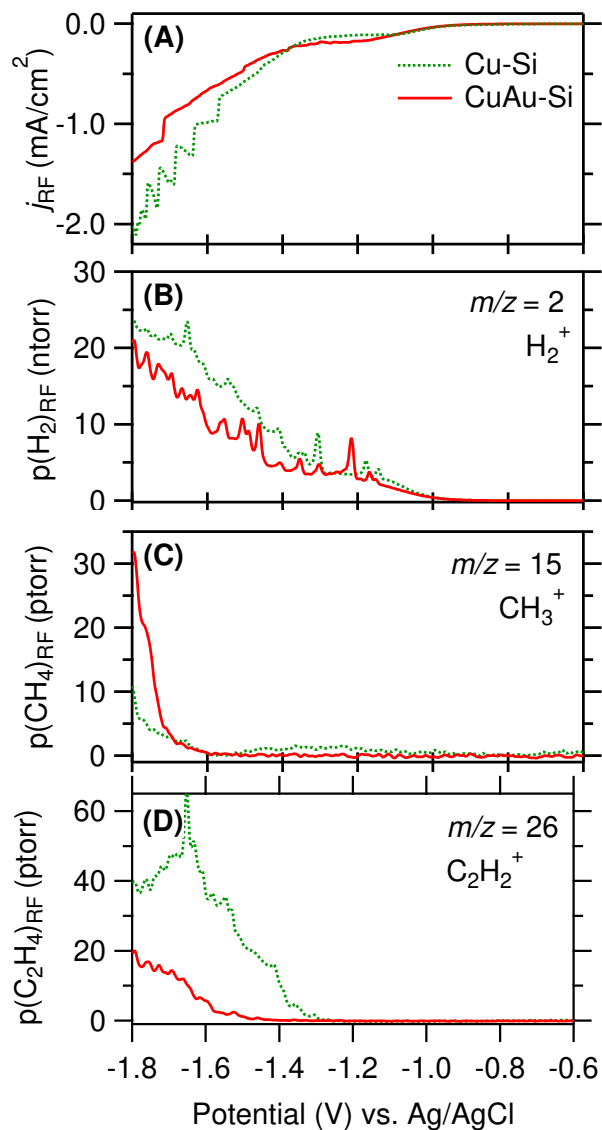


Figure 5.3: DEMS collected on Cu-Si and CuAu-Si in CO saturated 0.1 M potassium phosphate buffer (PH = 7). (A) Electrochemical current densities. (B) H_2^+ ($m/z = 2$), (C) CH_3^+ ($m/z = 15$), and (D) $C_2H_2^+$ ($m/z = 26$) partial pressures. All the signals in the figure are divided by the roughness factor of the respective film. Reproduced from Ref [158].

methane, and ethylene evolved during CORR. The onset potential for hydrogen (~ -1.2 V) and methane (~ -1.7 V) are similar on both Cu-Si and CuAu-Si films. In contrast, the onset potential of ethylene exhibits a $\sim 200 \pm 65$ mV cathodic shift on CuAu-Si film compared to that on Cu-Si film: On Cu-Si the onset potential is ~ -1.4 V and on CuAu-Si this is ~ -1.6 V. Here, the onset potential is defined as the potential at which 10% of the partial pressure at -1.8 V is observed. The disparate onset potential could arise from a dissimilar surface properties of Cu-Si and CuAu-Si films.

A difference in catalytic activity can also arise due to different local pH values at Cu-Si and CuAu-Si catalysts [199–201]. To explore this possibility, the same experiments were carried out in 0.1 M KOH electrolyte at a pH 12.85. At this pH, a significant drift in local pH due to hydrogen evolution is not expected [147, 202]. Observation of the same trend in the onset potential of ethylene formation in 0.1 M KOH electrolyte as in 0.1 M potassium phosphate, excludes the possibility of different local pH giving rise to difference in catalytic activity on Cu-Si and CuAu-Si films.

Another rationale for the observed difference in the ethylene onset potential is the exposure of gold or the formation of copper/gold alloys on CuAu-Si film [203, 204]. The $\text{C}\equiv\text{O}$ stretch frequency is sensitive to the identity of the metal catalyst. Therefore, we utilized the $\text{C}\equiv\text{O}$ stretch frequency of CO_{atop} to test if the gold is exposed on CuAu-Si film. The collected SEIRAS data do not show any evidence for the exposed gold on surface.

Additionally, DEMS data collected with Ar saturated electrolyte do not show any signal for hydrocarbon products. These control experiments suggest that the most probable explanation for the observed difference in ethylene onset potential on Cu-Si and CuAu-Si films, is the disparate properties of catalyst's morphology.

$\text{C}\equiv\text{O}$ Stretch Spectra of CO_{atop} on Cu-Si and CuAu-Si.

Highest coverage of CO on both Cu-Si and CuAu-Si films are observed at ≈ -1.3 V.

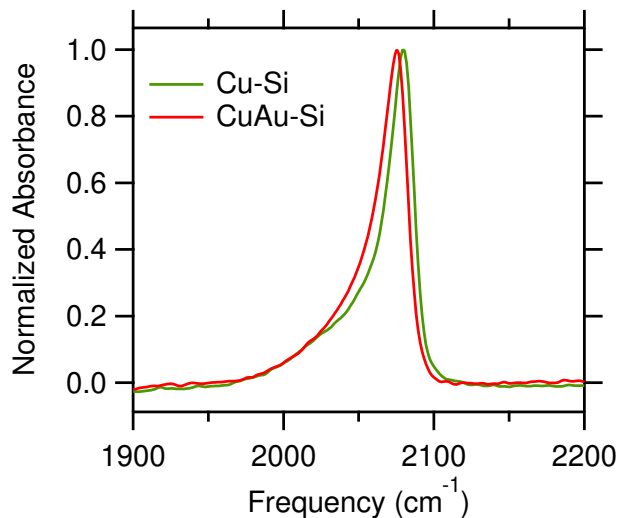


Figure 5.4: Normalized absorbance of CO_{atop} band on Cu-Si and CuAu-Si films at saturation coverage at -1.3 V. The spectra were concurrently collected with the DEMS data shown in Figure 5.3. Reproduced from Ref [158].

Inspection of $\text{C}\equiv\text{O}$ stretch spectra of CO_{atop} at this potential, as shown in Figure 5.4, tells that it only exhibits a minute difference on two Cu films disregard the large difference in catalytic activity. At large CO coverage, the $\text{C}\equiv\text{O}$ stretch frequency can be convoluted with dynamical dipole coupling and chemical effects (Chapter 2, Section 2.5). Therefore, we explored the $\text{C}\equiv\text{O}$ stretch frequency at low coverage limit, *i.e.* at low cathodic potentials on Cu-Si and CuAu-Si thin films.

As shown in Figure 5.5, the potential dependence of the $\text{C}\equiv\text{O}$ stretch band at low cathodic regime display significant differences on two Cu thin films. On Cu-Si bellow ≈ -0.95 V, a band at ≈ 2045 cm^{-1} is observed. Appearance of a second band ≈ 2080 cm^{-1} can be observed at potentials above ≈ -0.95 V. By careful analysis Gunathunge *et al.* have attributed these low frequency band (LFB) at ≈ 2045 cm^{-1} and high frequency band (HFB) at ≈ 2080 cm^{-1} , to CO_{atop} adsorbed on highly-coordinated terrace sites and under-coordinated defect sites (Chapter 3) [30]. Interestingly, an IR band at ≈ 2080 cm^{-1} dominates at all potentials on CuAu-Si film. This observation undoubtedly suggests that Cu-Si and CuAu-Si films possess disparate morphological proprieties.

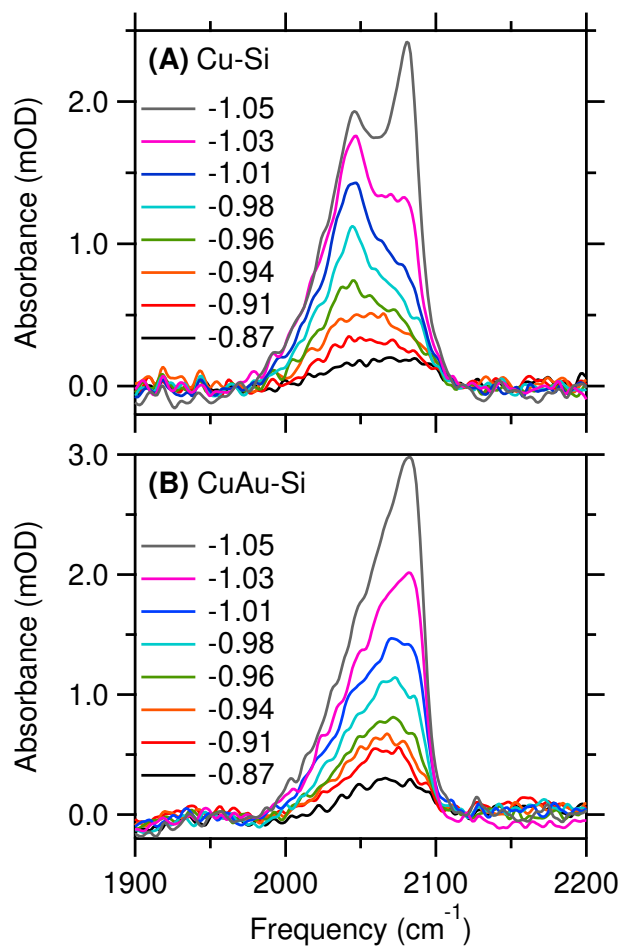


Figure 5.5: Potential dependence of the C≡O stretch of CO_{atop} on (A) Cu-Si and (B) CuAu-Si films. The annotation indicates the potential in V vs. Ag/AgCl. The spectra were collected concurrently with the DEMS data shown in Figure 5.3. Reproduced from Ref [158].

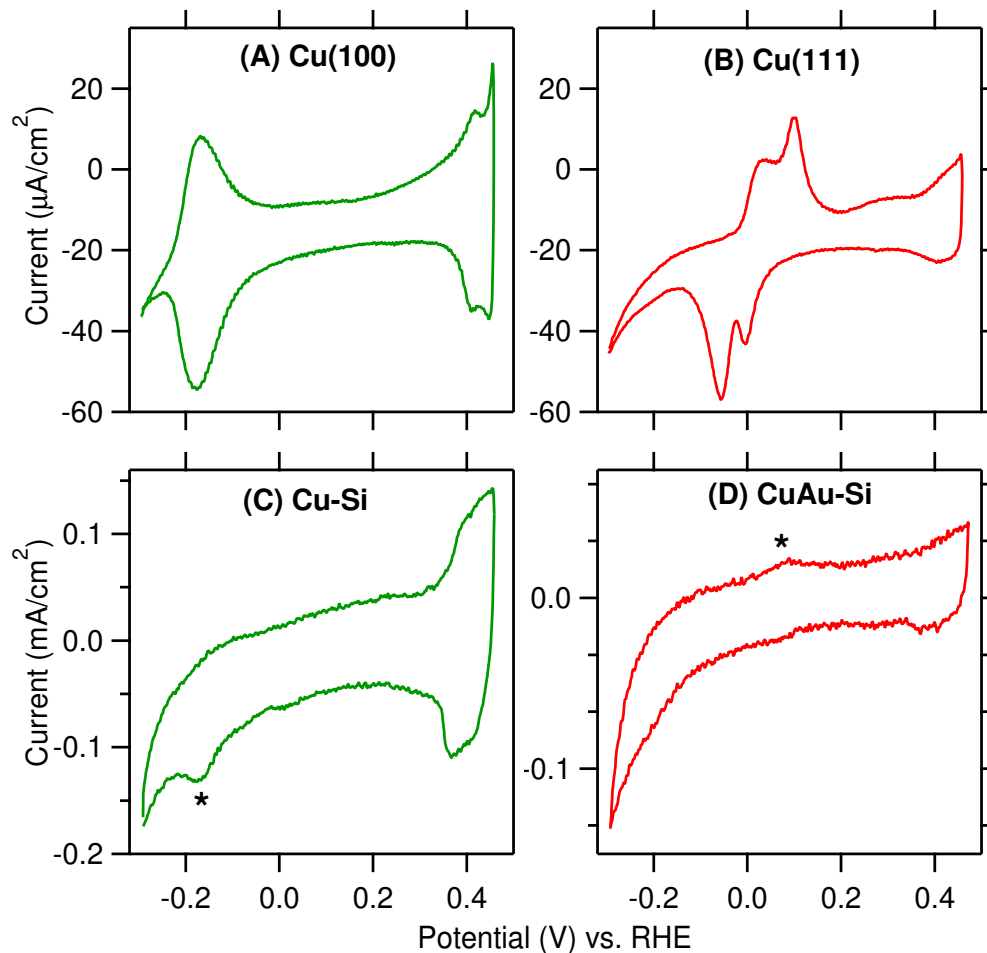


Figure 5.6: Cyclic voltammetry (CV) collected on (A) Cu(100) and (B) Cu(111) single crystals. CV collected on (C) Cu-Si and (D) CuAu-Si thin films. All the CVs were collected in Ar-saturated 0.1 M KOH at a scan rate of 50 mV/s. Geometric current density is shown in the pannels. Reproduced from Ref [158].

Cyclic Voltammetric Characterization of Surface Facets of Cu-Si and CuAu-Si.

To further characterize the Cu-Si and CuAu-Si films, a cyclic voltammetric (CV) characterization was employed. CVs collected on copper single crystal electrodes in alkaline electrolyte show characteristic hydroxide adsorption/desorption waves [205–208]. The peak potentials of these waves are unique for a given single crystal surface facet. Figure 5.6 (A) and (B) show the CVs collected on Cu(100) and Cu(111) single crystals, respectively, in Ar saturated 0.1 M KOH at a scan rate of 50 mV/s. For the purpose

of comparison of CV data collected in this study with published data, potential in here is reported against reversible hydrogen electrode (RHE). Cu(100) exhibits two waves at -0.17 V due to hydroxide adsorption and desorption. The nature and the peak potential of hydroxide adsorption/desorption waves of Cu(111) are distinct from that of Cu(100) and appears between -0.2 and 0.2 V. At potentials more positive than 0.3 V, copper surface is oxidized to Cu_2O . The oxidation/reduction current density in this more anodic potential regime is higher in Cu(100) compared to that in Cu(111). Our data agrees well with the published data on Cu(100) and Cu(111) [205–208].

The same CVs were then collected on Cu-Si and CuAu-Si films (Figure 5.6 (C) and (D)). On Cu-Si, a wave at -0.17 V (marked with an asterisk) is observed during the cathodic scan, where hydroxide desorption wave is observed on Cu(100). On CuAu-Si, a wave (*) at the potential range where the hydroxide adsorption is detected on Cu(111), is observed. In addition, comparison of the current density at more anodic potentials than 0.3 V indicates that Cu-Si bears a resemblance to that of Cu(100) and CuAu-Si display a similarity to that of Cu(111). The absence of the peaks during respective reverse scans on Cu-Si and CuAu-Si films can be due to small amplitudes of these peaks and sloping baseline of the CVs. The CV characterization data therefore indicate that Cu-Si surface possesses (100) surface facets while the predominant surface facet on CuAu-Si is Cu(111).

Indeed, it has being shown that polycrystalline copper shows a similar catalytic activity to that of Cu(100) single crystal [141]. Further, ESTM studies have shown that polycrystalline copper surface undergoes reconstruction during electrolysis and forms Cu(100) surface facets [46]. These observations can validate the presence of Cu(100) surface facets on Cu-Si film. Contradicting to these observations, CV characterization suggests the presence of Cu(111) facets on CuAu-Si film. CVs taken on the Au underlayer of CuAu-Si film (Figure 5.7) indicate the presence of Au(111), which is also shown in published data [209]. Hence, the presence of (111) facets on CuAu-Si can be due to the semi-epitaxial growth

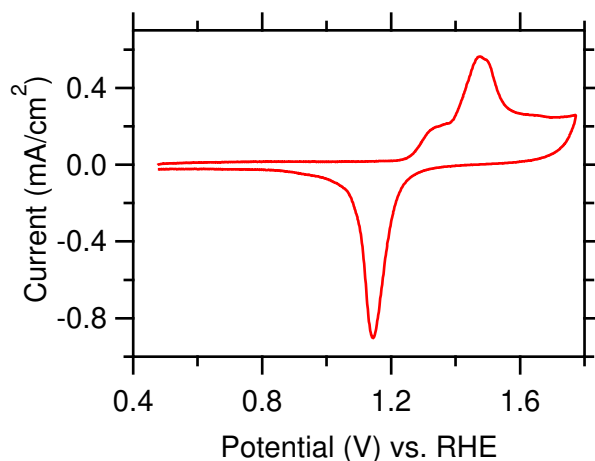


Figure 5.7: A CV collected on electroless deposited Au underlayer of CuAu-Si film in Ar-saturated 0.1 M H_2SO_4 at 50 mV/s scan rate. Geometric current density is shown in the figure. Reproduced from Ref [158].

of ≈ 8 nm thick Cu layer on Au(111) underlayer [210].

Effect of Dynamical Dipole Coupling on the $\text{C}\equiv\text{O}$ Stretching Band of CO_{atop} .

Figure 5.4 suggests that $\text{C}\equiv\text{O}$ stretch band at saturation coverage is governed by dynamical dipole coupling. To minimize the dynamical dipole coupling and to estimate the true coverage of CO_{atop} on Cu-Si and CuAu-Si films, IR data were collected in an isotopic mixture of CO (A detailed description of dynamical dipole coupling and isotopic dilution to minimize this effect is given in Chapter 2, Section 2.5). Figure 5.8 shows the normalized absorbance of CO_{atop} band at -1.3 V in a mixture of 10% $^{12}\text{C}^{16}\text{O}$ + 90% $^{13}\text{C}^{18}\text{O}$ and in an isotopically pure $^{12}\text{C}^{16}\text{O}$ on both Cu thin films. LFB_{HI} and HFB_{HI} indicate the LFB and HFB of the heavy isotope, $^{13}\text{C}^{18}\text{O}$. Asterisk denote the LFB of the $^{12}\text{C}^{16}\text{O}$ in the isotopic mixture. The absence of the HFB band of $^{12}\text{C}^{16}\text{O}$ in isotopic mixture thoroughly confirms that the spectra at saturation coverage is influenced by the dynamical dipole coupling.

Dynamical dipole coupling among isotopically different molecules does not show a frequency shift, although manifest it self as an intensity borrowing from the lower frequency band to the higher frequency band (Chapter 2, Section 2.5). Therefore, comparison of the intensity of the HFB_{HI} and (*) bands (indicated by arrows in the Figure 5.8) on

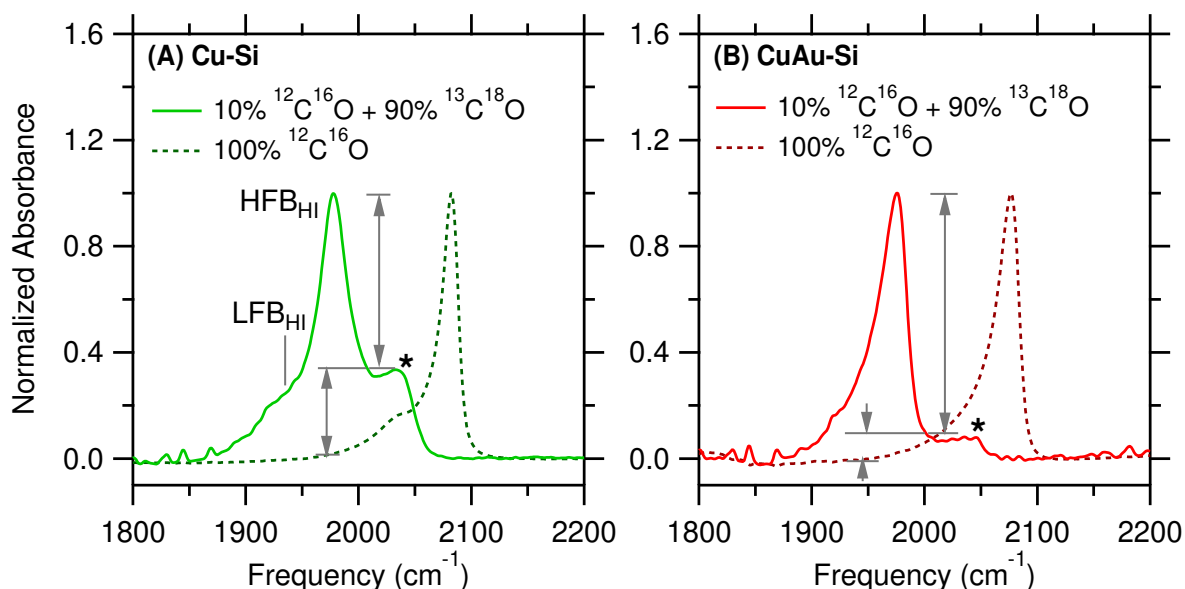


Figure 5.8: Normalized absorbance of CO_{atop} collected in an isotopic mixture of 10% $^{12}\text{C}^{16}\text{O}$ + 90% $^{13}\text{C}^{18}\text{O}$ (solid line) and in isotopically pure $^{12}\text{C}^{16}\text{O}$ (dashed line) on (A) Cu-Si and (B) CuAu-Si films at -1.3 V. Reproduced from Ref [158].

Cu-Si and CuAu-Si can provide an estimate of the relative coverage of CO on these thin films. Data show that the amplitude of the (*) band, which is the LFB of $^{12}\text{C}^{16}\text{O}$, is $\sim 30\%$ relative to that of HFB_{HI} on Cu-Si, while this is only $\sim 10\%$ on CuAu-Si films. This observation demonstrates that dynamical dipole coupling is higher on Cu-Si film compared to that on CuAu-Si film. A higher dynamical dipole coupling could arise from a higher CO coverage, therefore suggesting that the relative CO coverage on Cu-Si is higher than the CO coverage on CuAu-Si film.

Interpretation of the Potential Dependence of the $\text{C}\equiv\text{O}$ Stretch Spectra of CO_{atop} on Cu-Si and CuAu-Si.

CV characterization data demonstrate that the predominant surface facet on Cu-Si is Cu(100) and that on CuAu-Si is Cu(111). Here, by employing a simple Boltzmann relationship we interpret the disparate potential dependence of the $\text{C}\equiv\text{O}$ stretch spectra on Cu-Si and CuAu-Si films. Even though polycrystalline copper have a variety of surface

sites such as terrace, kink, step edges, defects, the model only considers two distinct type of surface facets, terrace and defect sites. This can be rationalize by successful modeling of the C≡O stretch band with two Gaussian functions (Figure 3.1).

Relative occupancy of CO_{atop} on terrace and defect sites is governed by Boltzmann relationship [158]:

$$\frac{N_{\text{defect}}}{N_{\text{terrace}}} = \frac{g_{\text{defect}}}{g_{\text{terrace}}} \exp\left(+\frac{\Delta E}{kT}\right) \quad (5.1)$$

where g_{defect} and g_{terrace} are the degeneracies of the two surface sites, k is the Boltzmann constant, and T is the absolute temperature. $\Delta E = E_{\text{defect}} - E_{\text{terrace}}$ is the difference between the binding energies of CO_{atop} on defect and terrace sites and the binding energies are defined as positive quantities in here.

According to the Equation 5.1, the distribution of CO_{atop} on terrace and defect sites are influenced by two factors. The first one is the degeneracies of terrace and defect sites. On CuAu-Si the higher C≡O stretch frequency of $\approx 2080 \text{ cm}^{-1}$ at potentials $< -1.0 \text{ V}$ can arise form the presence of a larger defect site density. If this is true, then the CO_{atop} coverage on CuAu-Si should be higher than that on Cu-Si film, since the adsorption energy of CO on defect sites is larger than on terrace sites [81]. However, isotope dilution experiments suggest otherwise. Therefore, the disparate potential dependence of C≡O stretch data may not arise due to differences in the first factor related to g_{defect} and g_{terrace} .

The second factor that influences the distribution of CO_{atop} is the difference in CO binding energies on defect and terrace sites. ΔE on CuAu-Si which possesses Cu(111) and defect sites is 0.11 eV [81] and ΔE on Cu-Si which has Cu(100) and defect site is 0.07 eV [81]. The calculated probability distribution using these ΔE values show that Cu-Si has five times higher probability to occupy a terrace site compared to that of CuAu-Si. Higher probability to find CO_{atop} on terrace sites on Cu-Si is manifested as an appearance

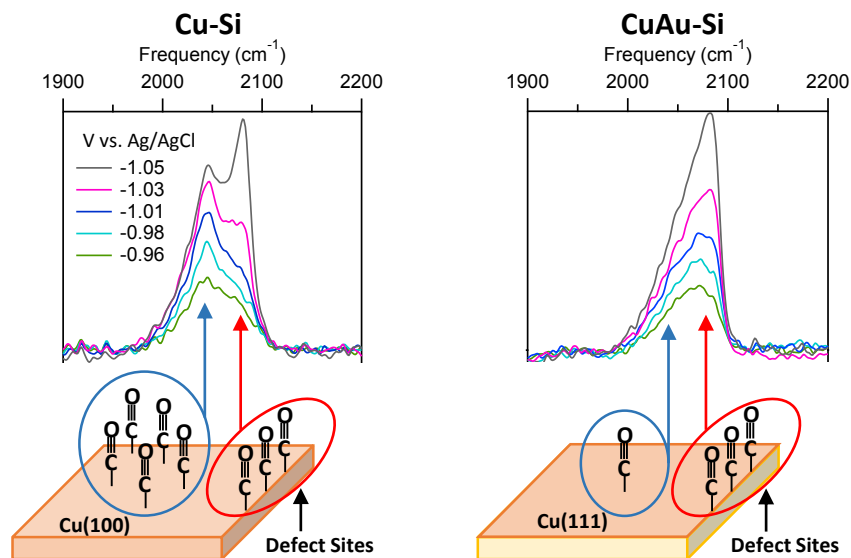


Figure 5.9: Schematic summarizing the key findings. (Left) Cu-Si film that possesses (100) and defect sites has a higher probability of finding CO_{atop} on terrace sites, therefore giving a separate IR peak at $\approx 2045 \text{ cm}^{-1}$. (Right) CuAu-Si film that possesses (111) and defect sites has a lower coverage of CO_{atop} on terrace sites. Thus, a separate IR peak is not observed for CO_{atop} adsorbed on Cu(111) terrace sites. Reproduced from Ref [158].

of a separate IR band at $\approx 2045 \text{ cm}^{-1}$. However, the low coverage of CO_{atop} on (111) terrace sites on CuAu-Si film is not sufficient to develop a separate band for terrace sites. This conclusion is summarized in Figure 5.9.

Interpretation of the Onset Potential Difference in Ethylene on Cu-Si and CuAu-Si.

Previous publications have shown that the onset potential of ethylene formation is more cathodic in copper catalysts with predominant Cu(111) facets compared to that on copper catalysts with (100) as the predominant facet [132, 142, 199]. Further, Hori *et al.* have shown that the FE for ethylene formation during CO_2RR in 0.1 M KHCO_3 on Cu(111) electrode is five times lower than that on Cu(100) [195]. These evidence further confirm our assignment of predominant surface facets on Cu-Si and CuAu-Si films: the predominant surface facet on Cu-Si is (100) while Cu(111) is the ubiquitous surface facet on CuAu-Si film.

5.3 Conclusions

With concurrent product and structure analysis performed using a combined DEMS-SEIRAS setup, we show that two frequently employed rough thin copper films in SEIRAS investigations exhibit distinct catalytic activities during CORR. Onset potential of ethylene on CuAu-Si film is $\sim 200 \pm 65$ mV more cathodic than that on Cu-Si film. SEIRAS data collected with an isotopic mixture of CO revealed that the C \equiv O stretch spectra of CO_{atop} at saturation coverage is dominated by the dynamical dipole coupling. In addition, these data suggest that Cu-Si has a relatively higher CO_{atop} coverage compared to that of CuAu-Si which is disclosed by the presence of a higher dynamical dipole coupling on Cu-Si film.

A distinct potential dependence of the C \equiv O stretch band of CO_{atop} is observed on Cu-Si and CuAu-Si at low CO coverage limits (< -1.0 V). This distinct potential dependence indicates the presence of two different predominant surface facets on the two copper thin films with different CO binding energies. With a Boltzmann relationship we show that the difference in the potential dependence of the C \equiv O stretch band can be due to the presence of a terrace site with a higher CO binding energy on Cu-Si, and a lower CO binding energy terrace site on CuAu-Si.

The CV characterization enclosed that Cu-Si has (100) and CuAu-Si has (111) as the predominant surface facets together with defect sites. Our study highlights that the potential dependence of the C \equiv O stretch band of CO_{atop} at low CO coverage can be used as an indicator of the atomic level morphology of rough metal catalysts under operating conditions. Further, this study emphasizes the complexity associated with interpreting C \equiv O stretch spectra.

5.4 Materials and Methods

Materials. Chemicals for Cu or Au thin film deposition on Si: NH_4F (40 wt.% in H_2O), HF (48 wt.%), $\text{NaAuCl}_4 \cdot 2\text{H}_2\text{O}$ (99.99%; metals basis), Na_2SO_3 (98.5%; for analysis, anhydrous), $\text{Na}_2\text{S}_2\text{O}_3 \cdot 2\text{H}_2\text{O}$ (99.999%; trace metal basis), and NH_4Cl (99.999%; metal basis) were purchased from Fisher Scientific (Waltham, MA). $\text{CuSO}_4 \cdot 5\text{H}_2\text{O}$ (99.999%; trace metal basis), EDTA-Na_2 (99.0 – 101.0%; ACS Reagent), 2,2-bipyridine ($\geq 99\%$; ReagentPlus), HCHO (35 wt.%; 10% methanol as stabilizer), and NaOH (99.99%; trace metals basis) were acquired from Sigma Aldrich (St. Louis, MO). Polycrystalline diamond pastes and alumina slurry were procured from Ted Pella (Redding, CA) or Electron Microscopy Sciences (Hartfield, PA).

Chemicals for electrochemical measurements: KH_2PO_3 , $\geq 99.995\%$, TraceSELECT, metals basis; K_2HPO_3 , $\geq 99.999\%$, TraceSELECT, metals basis; KOH , 99.99%, trace metals basis, Sigma Aldrich. High-purity water for electrolyte preparation was derived from a Barnstead Nanopure Diamond system.

Ar (ultra high purity), N_2 (ultra high purity), and CO (99.999%) were obtained from Air Gas (Radnor, PA). Doubly labeled $^{13}\text{C}^{18}\text{O}$ (99 atom % ^{13}C , 95 atom % ^{18}O) was purchased from Sigma Aldrich.

$\text{Cu}(100)$ and $\text{Cu}(111)$ single crystals ($5 \times 5 \times 1$ mm) were purchased from MTI Corporation (Richmond, CA).

Cu-Si Film Preparation. Cu-Si film was deposited on a 60° Si ATR prism following a similar method described in Chapter 3, Methods and Materials.

CuAu-Si Film Preparation. The total reflecting surface of a 60° Si ATR prism was polished with 6 and 1 μm diamond pastes for 5 min each. Then, this was polished with 1 μm alumina slurry for another 5 min. The polished Si surface was rinsed under running Nanopure water stream while wiping it with a wet Kim-wipe for ~ 1 min. The Si prism

was then sonicated in water and in acetone alternatively for 5 time for 5 min in each. Subsequently, the Si prism was etched by immersing the surface in a 40% NH_4F solution for 90 s. The deposition of the Au layer was carried out by immersing the etched surface in a mixture of 2 : 1 plating solution and 2% HF solution at 60°C for 120 s. The plating solution contained 15 mM $\text{NaAuCl}_4 \cdot 2\text{H}_2\text{O}$, 150 mM Na_2SO_3 , 50 mM $\text{Na}_2\text{S}_2\text{O}_3 \cdot 2\text{H}_2\text{O}$, and 50 mM NH_4Cl . Then, the Au film was washed away by adding few drops of an aqua regia on to the Au film. After rinsing the surface well with Nanopure water, it was immersed again in the 2 : 1 mixture of plating solution and 2% HF solution for another 120 s. This was carried out to increase the adhesion of the Au film to the Si prism. Usually this step was repeated for 2 times to get a homogeneous and stable Au film. After the deposition the resistance across the film was measured and the measured resistance is 8 – 10 Ω .

Au film was then assembeled into a single compartment electrochemical cell with a Au wire as the counter electrode, Ag/AgCl as the reference electrode, and blanketed with 4 mL of 0.1 M H_2SO_4 . Five CVs were collected from 0 to 1.5 V at 50 mV/s scan rate in Ar saturated H_2SO_4 . Subsequently, the Cu deposition was carried out by adding 5.75 mM of Cu_2SO_4 to the electrolyte. The film was held at -0.2 V until the desired amount of charge passed (≈ 40 mC). The electrolyte was stirred at ~ 400 rpm during the deposition.

Pre-Treatment of Cu-Si and CuAu-Si Films Prior to DEMS and FTIR Experiments. Cu-Si and CuAu-Si were pre-treated before the collection of DEMS-FTIR data to remove copper oxides. First, the electrolyte was purged with Ar gas at 5 sccm rate for 20 min at open circuit potential (OCP). Then, 5 CV cycles were collected form -0.17 to -0.6 V at 50 mV/s scan rate. Following this, CVs were collected from -0.6 to -0.7 V at 20, 40, 60, 80, and 100 mV/s scan rates to determine the roughness factor of the film (Details of the roughness factor determination of Cu thin films are given with the Figure 3.6). Next, 3 CVs were collected from -0.6 to -1.2 V at 10 mV/s scan rate. The film was never exposed to oxidative potentials or subjected to OCP after these CVs. Then, the film was

held at -0.6 V for pH 7 electrolyte and at -0.8 V for pH 12.85 electrolyte for 20 min while purging CO at 5 sccm rate.

DEMS-SEIRAS Experiments. DEMS-SEIRAS experiments were carried out in a single compartment cell as shown in Figure 5.2. The porous Teflon tip was placed at $\sim 100\mu\text{m}$ distance from the working electrode. DEMS setup is described in elsewhere [29]. Prior to each experiment the cell was cleaned by immersing it in a mixture of 30 wt% H_2SO_4 and 30 wt% HNO_3 for 1 hour followed by sonication in Nanopure water for another 1 hour. Then the cell was assembled with a Pt foil as the counter electrode and a Ag/AgCl as the reference electrode. 6 mL of freshly prepared 0.1 M potassium phosphate or 0.1 M KOH was used as the electrolyte. Concurrent DEMS and SEIRAS data were collected while scanning the potential from -0.6 to -1.8 V at 1 mV/s scan rate in 0.1 M potassium phosphate or from -0.8 to -1.8 V in 0.1 M KOH. ATR-FTIR parameters were described in elsewhere [30].

Isotope Dilution Experiments. Isotope dilution experiments were carried out in a home-built two-compartment SEIRAS cell which is shown in Figure 5.10. The cell was subjected to a cleaning prior to each experiment as described in the previous section. Isotopic mixture of 90% $^{13}\text{C}^{18}\text{O}$ + 10% $^{12}\text{C}^{16}\text{O}$ was achieved by purging $^{13}\text{C}^{18}\text{O}$ at 4.5 sccm and $^{12}\text{C}^{16}\text{O}$ at 0.5 sccm. Potential was scanned from -0.6 to -1.4 V at 2 mV/s rate while collecting spectral data.

CV Characterization Experiments. Epoxy was used to cover the back side of the Cu(100) and Cu(111) single crystals. Then, the surface of the single crystals were cleaned electrochemically in an acid solution of $\text{H}_3\text{PO}_4:\text{H}_2\text{SO}_4:\text{H}_2\text{O} = 10 : 5 : 2$. A potential of 2.3 V vs. Cu was applied for 2 s followed by 30 s at open circuit potential and another 2 s at 2.3 V. The electrodes were then thoroughly rinsed with high-purity water before they were immersed in an Ar-saturated 0.1 M KOH solution. CVs of Cu(100) and Cu(111) were collected in a single compartment cell while the electrolyte was purged with Ar gas

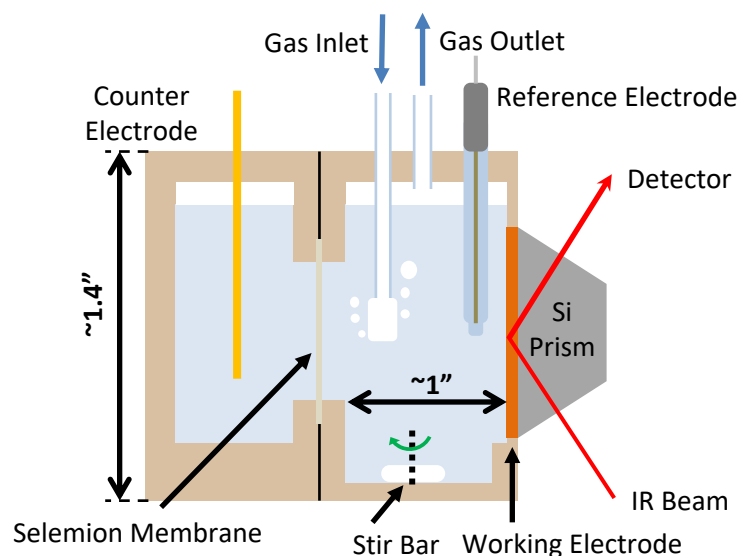


Figure 5.10: Schematic of the home-built two-compartment polyetheretherketone (PEEK) SEIRAS electrochemical cell. Reproduced from Ref [158].

at a rate of 5 sccm. The electrolyte was stirred. Ten CV cycles were collected from -0.3 to 0.45 V vs. RHE at a 50 mV/s scan rate and the 10^{th} cycle is shown in Figure 5.6. CVs of the Cu-Si and CuAu-Si films were collected in Ar-saturated 0.1 M KOH in the cell shown in Figure 5.10 under stirring of the electrolyte. The Cu-Si and CuAu-Si films were pre-treated by applying five CVs with turning potentials of -0.13 and -0.7 V at a scan rate of 50 mV/s. Then, 10 CVs were collected from -0.3 to 0.45 V vs. RHE at a 50 mV/s scan rate while Ar was purged at a rate of 5 sccm. The 10^{th} cycle is shown in Figure 5.6.

5.5 Acknowledgements

We greatly acknowledge the financial support by the National Science Foundation CAREER award (award no.: CHE-1847841). C. M. G expresses gratitude to Jingyi Li and Julie J. Hong for their support in collecting SEIRAS data and CuAu-Si film preparation. C. M. G. further thanks to Xiang Li for her assistance in collecting DEMS data.

5.6 Original Publication

This chapter has been published: Gunathunge, C. M., Li, J., Li, X., Hong, J. J. & Waagele, M. M, *ACS Catal.* **10**, 6908–6923 (2020).

Chapter 6

Probing Promoting Effects of Alkali Cations on the Reduction of CO at the Aqueous Electrolyte/Copper Interface

6.1 Introduction

Electrochemical interfacial properties often evolves under electrocatalytic conditions. This dynamic nature of the interfacial properties influence the activity and selectivity of electrocatalytic processes in a multitude of ways. Chapter 3-5 demonstrate the utilization of surface-enhanced infrared absorption spectroscopy (SEIRAS) combined with surface-adsorbed CO (CO_{ads}) as a molecular probe to infer the atomic level morphology and catalyst structure under operating condition. Herein, we focus on the examination of the properties of the electrolyte side during CO reduction reaction at a copper/electrolyte interface.

Indeed there are experimental evidence that show cations residing in an electrochemical interface exerts a great influence on determining the activity and selectivity of electrocatalytic processes [9, 49, 211–213]. For instance, Singh *et al.* have shown that the Faradaic efficiency (FE) for desired hydrocarbon products increases from $\sim 10\%$ to $\sim 70\%$ when the cation is switched from Li^+ to Cs^+ , during CO_2 reduction on copper electrode at -1 V vs. reversible hydrogen electrode (RHE) [130]. Interestingly, the ethylene to methane product ratio also increase by a factor of 3 when cation is switched from Li^+ to Cs^+ [130].

Even though, cation effects on CO₂ reduction have been demonstrated, the origin of these effects is still unclear. A better usage of cation effects to modify the activity and selectivity of electrocatalytic processes requires a thorough understanding of the origin of these effects.

Frumkin's theory is a frequently used explanation of the observed cation effects [211]. Frumkin's theory states that the adsorption of inert cations (such as Li⁺ and Cs⁺) shifts the zeta-potential (ζ) to a more positive potential. ζ potential is the potential drop across the diffuse layer measured at the outer Helmholtz plane with respect to the bulk potential of the electrolyte (Figure 2.10). Consequently the activation barrier for the charge transfer decreases with increasing ζ potential. As a result the theory predicts an acceleration of CO₂ reduction reaction with increasing tendency for cations to adsorb on the catalyst.

This theory however does not predict the influence of cation adsorption on the coverage of CO_{ads}, which is a crucial on-pathway intermediate during CO₂ reduction that leads to the potential-limiting step of the reaction [41, 133, 135, 136, 156]. CO_{ads} coverage can impact the adsorption energies of intermediates and activation barrier of the elementary steps through interaction with the electric field created at the interface via adsorption of cations [49, 50, 125]. This is due to CO's significant dipole moment and polarizability. Therefore, it is crucial to understand the cation effects on CO_{ads} coverage as this directly influence the catalytic activity and selectivity of CO₂ reduction reaction.

Herein, using surface-enhanced IR absorption spectroscopy in attenuated-total reflection configuration (ATR-SEIRAS) we investigate the effect of alkali cations (Li⁺, K⁺, and Cs⁺) on atop-bound CO (CO_{atop}) on copper electrode during CO reduction reaction. We show that the CO_{atop} reduction is \approx 10 times faster in Cs⁺ cation than in Li⁺ cation containing electrolyte. We demonstrate that this increase in the reduction rate is due to an increment in the interfacial electric field in the presence of larger cations which decreases the activation barrier for hydrogenation of CO_{atop}. The increase in the CO_{atop} reduction

rate leads to a mass transport limitation and thus a faster decrease in the CO_{atop} coverage at potentials ≈ -1 V vs. RHE in two large cations, Cs^+ and K^+ , compared to that in Li^+ . Additionally, we show that Cs^+ and K^+ specifically adsorb on copper and leads to a significant surface reconstruction.

6.2 Results and Discussion

Dependence of IR Spectra of CO_{atop} on Cation Identity.

To investigate the cation effect on CO_{atop} coverage during CO reduction reaction, we collected IR spectra during a cyclic voltammetric (CV) scan from -0.38 to -1.48 V vs. standard hydrogen electrode (SHE) in CO-saturated 0.1 M bicarbonate solutions of Li^+ , K^+ , and Cs^+ . All the potentials in this Chapter are referenced against SHE unless otherwise noted. Figure 6.1 shows the $\text{C}\equiv\text{O}$ stretch mode in the frequency range from $2000 - 2100 \text{ cm}^{-1}$ where $\text{C}\equiv\text{O}$ stretch mode for CO_{atop} is observed [97, 98, 141, 148, 149, 196]. A prominent IR band for CO_{atop} is observed in the presence of all 3 cations during both cathodic forward scan and anodic reverse scan. Note here, D_2O was used as the electrolyte to observe IR bands in a wide window of frequencies and the pH^* of the electrolytes before the experiments were 8.7 ± 0.1 .

Dependence of CO Coverage on Cation Identity.

Figure 6.2 shows the normalized integrated band area of CO_{atop} band observed during CV scans shown in Figure 6.1. During forward scan, in Li^+ containing electrolyte, CO_{atop} band area increases with increasing cathodic potential from ≈ -0.6 to -1.0 V, then stay approximately constant within -1.0 to -1.3 V. A slight decrease of the CO_{atop} area is observed when the potential is scanned to more cathodic potentials. In contrary to this observation, normalized CO_{atop} band area in K^+ and Cs^+ containing electrolytes, exhibits a maximum at -1.1 V and then a drastic decrease of the band area almost up to zero at

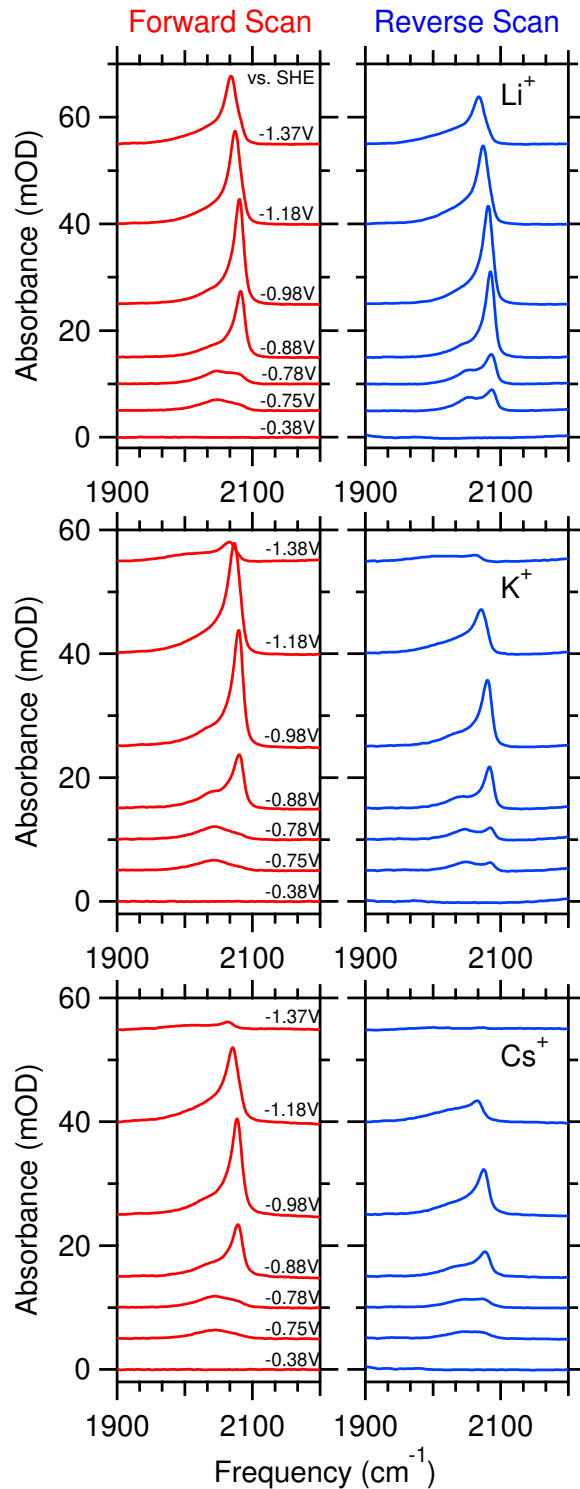


Figure 6.1: Representative IR spectra of the $\text{C}\equiv\text{O}$ stretch mode of CO_{atop} collected in CO -saturated 0.1 MDCO_3 ($M = \text{Li}^+, \text{K}^+, \text{Cs}^+$) during a cyclic voltammetric scan from -0.38 to -1.48 V vs. SHE at 2 mV/s scan rate. IR spectra collected during cathodic forward scan (left panels) and anodic reverse scan (right panels) are shown. Reproduced from Ref [109].

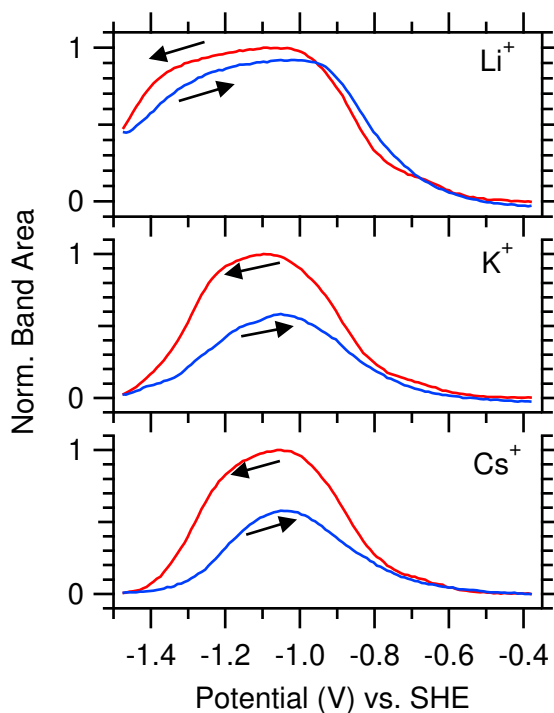


Figure 6.2: Normalized integrated band area of CO_{atop} shown in Figure 6.1 in 0.1 MDCO_3 ($M = \text{Li}^+, \text{K}^+, \text{Cs}^+$) as indicated in the panels. Red and blue traces represent data collected during cathodic forward and anodic reverse scans, respectively. The arrows indicate the direction of the potential scan. Reproduced from Ref [109].

more cathodic potentials. Normalized CO_{atop} band areas during forward and reverse scans show a little hysteresis in Li^+ containing electrolyte while a substantially larger hysteresis is observed in K^+ and Cs^+ containing electrolytes.

The observed substantial decline of the CO_{atop} band area at large cathodic potentials during the forward scan in the presence of K^+ and Cs^+ can be due to: (1) An increase in the CO reduction rate. (2) A reconstruction of the copper surface in the presence of larger cations. (3) Desorption of CO from the surface. (4) A combination of the factors 1 – 3.

Promotion of CO Reduction Kinetics by Cs^+ .

Investigation of the kinetics of CO reduction in the presence of Li^+ and Cs^+ cations was carried out by stepping the potential from a saturation coverage of CO at -1.04 V to a reaction potential at -1.51 V. Figure 6.3 shows the time dependence of the CO_{atop}

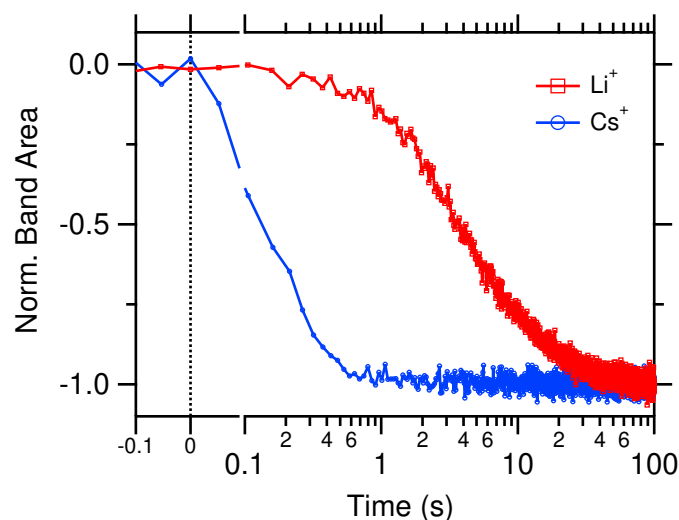


Figure 6.3: Time dependence of the normalized band area of CO_{atop} following a potential step from saturation coverage of CO at -1.04 V to a reaction potential of -1.51 V vs. SHE. Data were collected in CO-saturated 0.1 M bicarbonate solutions as indicated. Reproduced from Ref [109].

band area following this potential step. This data indicate that CO_{atop} reduction kinetics are ≈ 10 times faster in the presence of Cs^+ containing electrolyte compared to that of Li^+ containing electrolyte.

The bulk pH^* of 0.1 M LiDCO_3 and CsDCO_3 immediately before the experiment was 9.0 ± 0.1 . To assess whether the local pH changes in these two cations containing electrolytes give rise to the observed cation effects, we carried out the same experiment but with ± 20 mV differences in reaction potential. Observation of the similar kinetic trend as shown in Figure 6.3 confirms that the observed promotion of the CO reduction rate in Cs^+ is not due to local pH changes but due to cation effects.

Dependence of Interfacial Electric Field Strength on Cation Identity.

We hypothesize that the promotion of CO reduction in the presence of Cs^+ cation can be due to an increase in the interfacial electric field that reduces the kinetic barrier for further reduction of surface-adsorbed CO.

Our hypothesis is based on recent theoretical studies that has demonstrated: (1) Lo-

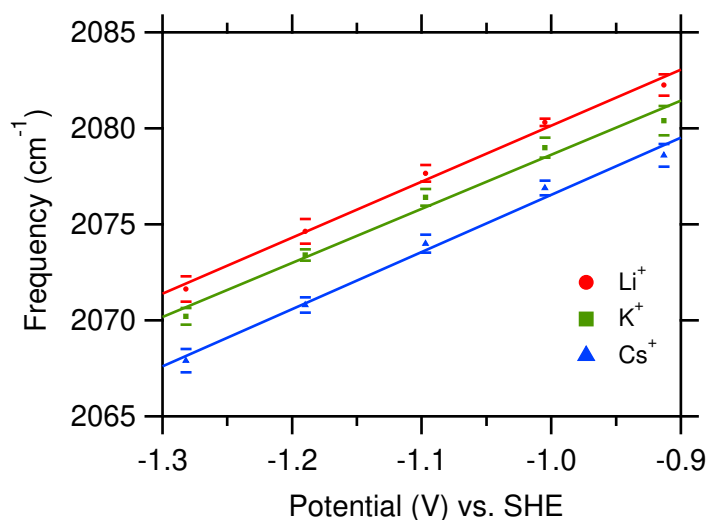


Figure 6.4: $\text{C}\equiv\text{O}$ stretch frequencies as a function of potential collected in CO-saturated 0.1 M bicarbonates of Li^+ , K^+ , and C^+ containing electrolytes. The error bars show ± 2 standard deviation calculated from 3 independent experiments. Solid lines are linear fits to the experimental data. Reproduced from Ref [109].

calized electric fields generated by surface-adsorbed cations decrease the kinetic barrier for the conversion of CO_{ads} to CHO [50]. (2) Surface-adsorbed CO dimer experiences a large ion-induced stabilization, suggesting a reduction of thermodynamic overpotential for reaction that leads to C_{2+} products [49].

Frequency of CO_{atop} was used as a probe of the interfacial electric field. The vibrational frequency of $\text{C}\equiv\text{O}$ stretch mode is sensitive to the double layer properties and specifically depends on the electric field at the interface according to the Stark effect (Chapter 2, Section 2.7) [169, 214, 215]. CO_{atop} IR band shown in Figure 6.1 is composed of two IR bands due to CO adsorbed on highly-coordinated terrace sites (low frequency band, $\approx 2050 \text{ cm}^{-1}$) and due to CO adsorbed on under-coordinated defect sites (high frequency band, $\approx 2080 \text{ cm}^{-1}$) [30]. The frequency of the high frequency band of CO_{atop} can be read unambiguously and are shown in Figure 6.4 as a function of applied potential. Figure 6.4 shows the frequency of CO_{atop} at potentials where a clear high frequency band is observed.

In the given potential range in Figure 6.4, CO coverage in Li^+ decreases by $\approx 10\%$ while CO coverage in K^+ and Cs^+ decreases by $\approx 70\%$. However, the slope of the Figure 6.4, which is the electrochemical Stark tuning rate, is $\approx 30 \text{ cm}^{-1}\text{V}^{-1}$ in the presence of all 3 cations. This indicates that the frequency of CO_{atop} is not affected by the coverage effects such as dynamical dipole coupling, but is influenced by the local electric field at the interface.

Even though, all 3 cations possess similar electrochemical Stark tuning rate, the slope is shifted to lower frequencies by 1.4 and 3.7 cm^{-1} when moving from Li^+ to K^+ and Cs^+ containing electrolytes, respectively. The decrease in the frequency with increasing cation size suggests that surface-adsorbed CO molecules experience a greater electric field that shift their $\text{C}\equiv\text{O}$ stretch frequency to lower energy. $\text{C}\equiv\text{O}$ stretch frequency data and CO reduction kinetic data together show that the CO reduction promotion in larger cation arises due to a greater interfacial electric field created with adsorption of these cations.

Specific Adsorption of Cations.

Inspection of the normalized integrated band area in Figure 6.2 shows that the hysteresis in band area between forward and reverse scans increases with increasing size of the cation. Cations can adsorb on the catalyst's surface through specific adsorption [50, 125, 211, 216], where the cation chemisorb on the surface or through electrostatic adsorption [49], where the solvated cations reside close to the surface. Further, it has been shown that the tendency of alkali cations to reside in the electrochemical double layer increases with increasing size of the cation [49, 211, 216]. Taken together our data suggest that the hysteresis of the band areas between forward and reverse scans, could arise from the specific adsorption of K^+ and Cs^+ cations on the copper electrode. Since adsorption of ionic species can induce surface reconstruction [217–220], the specific adsorption of larger cations may induce a surface reconstruction giving rise to the observed hysteresis of the CO_{atop} band area with K^+ and Cs^+ cations.

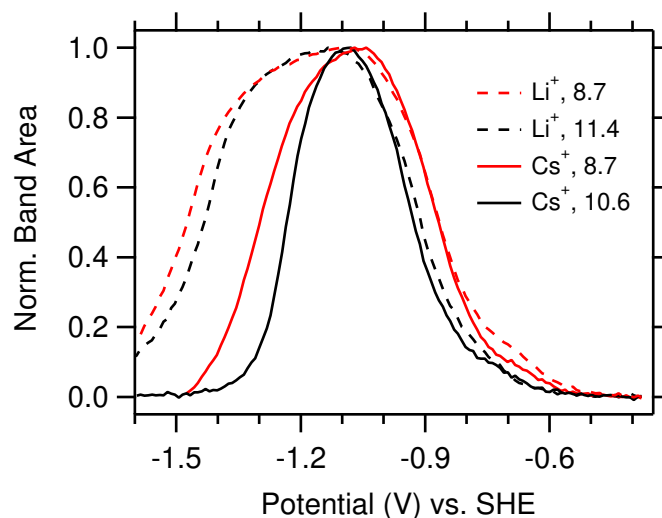


Figure 6.5: Normalized integrated band area of CO_{atop} in 0.1 M Li^+ and Cs^+ bicarbonate (pH^* 8.7) and 0.05 M Li^+ and Cs^+ carbonate (pH^* 11.4 and 10.6, respectively.) Reproduced from Ref [109].

This irreversible surface reconstruction however do not affect the CO reduction rate as we have observed a significant CO_{atop} band area during the reverse scan and as well as in consecutive CV scans. Further, repeated kinetic experiments did not show a reduction of the CO_{atop} band area, suggesting that surface reconstruction through cation adsorption does not occur at the time scale of kinetic experiments.

pH-Dependence of CO Coverage.

The local pH at the electrochemical interface can be influenced by the cation identity [130, 211, 221]. To investigate whether this change in the local pH with cation identity exerts an effect on the CO reduction rate, we carried out additional experiments in 0.05 M Li_2CO_3 and Cs_2CO_3 . The bulk pH^* of these two electrolytes were 11.4 and 10.6, respectively. Figure 6.5 shows the normalized integrated band areas of CO_{atop} in bicarbonate and carbonate solutions Li^+ and Cs^+ cations as indicated.

Local pH at the electrochemical interface during cation adsorption is affected by the ζ -potential [211]. According to Frumkin's theory, a rise in ζ -potential results an increase in the local pH according to the following relationship [211]:

$$\Delta pH_{local} = \frac{\Delta \zeta F}{2.303RT} \quad (6.1)$$

where F , R , and T are Faraday constant, ideal gas constant, and the absolute temperature, respectively. It is shown that an increase in the ζ potential less than 60 mV, results an increase in the local pH less than 1 pH unit [211]. The difference in the bulk pH* of the Li⁺ bicarbonate and carbonate electrolytes is 2.7. By making the reasonable assumption that the local pH for a given cation follows its bulk pH, comparison of the CO_{atop} band area (red and black dotted lines) at large cathodic potentials show that there is only a minute difference. Therefore, even large local pH changes only exhibit a minute effect on CO_{atop} coverage.

However, comparison of the CO_{atop} band area at the same pH (8.7) but in different cations (red dotted line and red solid line) present that the switching cation from Li⁺ to Cs⁺ shifts the decline in the CO_{atop} band area by \approx 200 mV to more positive potentials. Taken together, the data demonstrate that even though local pH change can have a small effect on the CO coverage, it is not the dominant mechanism that give rise to the promotion of CO reduction in Cs⁺ containing electrolyte.

A recent theoretical and experimental studies have shown that, hydrated Cs⁺ cation acts as a better buffer compared to hydrated Li⁺ cation [130, 221]. Hence, the local pH in the presence of Cs⁺ is lower than in the presence of Li⁺ cation. Comparison of the normalized band area of CO_{atop} in Figure 6.5 for the same cation (red and black traces) indicate that CO coverage declines with increasing pH. Following this observation, given that hydrated Cs⁺ is a good buffer, we would expect a higher CO coverage in the presence of Cs⁺. However, the opposite is observed suggesting that in our case local pH change is not the major factor that effect the CO coverage.

Effect of Cations on Surface-Bound CO Electrogenerated by the Reduction of CO₂.

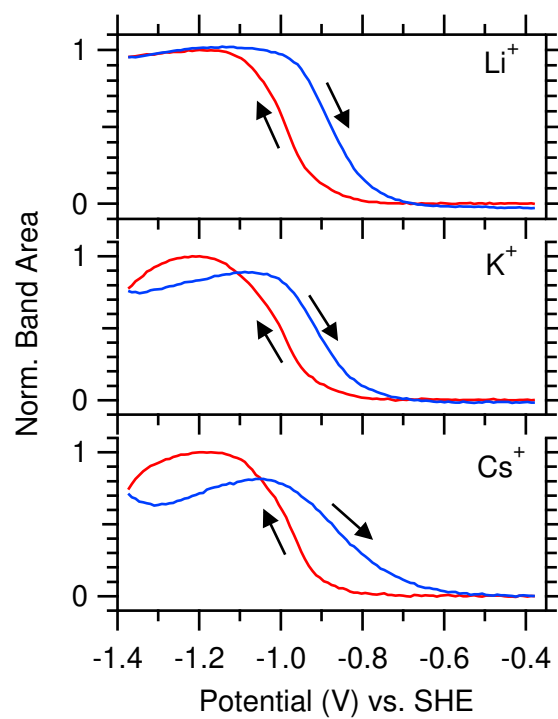


Figure 6.6: Normalized integrated band area of CO_{atop} electrogenerated from reduction of CO_2 . Experiments were carried out in CO_2 -saturated 0.1 M alkali metal bicarbonate solutions ($\text{pH}^* 6.8 \pm 0.1$) as indicated. Reproduced from Ref [109].

All the experiments discussed up to now were carried out in CO-saturated bicarbonate or carbonate electrolytes with slightly alkaline pH*. To examine whether the same trend is observed in neutral pH with electrogenerated CO from CO₂ reduction, we compared the integrated band area of CO collected in CO₂ saturated alkali metal bicarbonate solutions at pH* 6.8. Figure 6.6 shows that normalized integrated band area of CO_{atop} follow the same trend as observed in Figure 6.2. But, the decrease in the CO_{atop} band area at high cathodic potentials is less pronounced, as the bulk concentration of CO₂ is ≈ 30 higher than that of CO.

6.3 Conclusions

In this study we show that CO coverage on copper electrode during CO₂/CO reduction reaction is greatly influenced by the identity of the alkali metal cation. The CO coverage is greatly declined at cathodic potential ≈ -1.4 V vs. SHE, in the presence of K⁺ and Cs⁺ cations while this is relatively stable in the presence of Li⁺. By employing time-resolved surface sensitive IR spectroscopy, we show that CO reduction kinetics are ≈ 10 times faster in Cs⁺ cation compared to that in Li⁺ cation. The shift in the frequency to lower values with increasing cation size suggests that the promotion of CO reduction rate can arise from an increase in the local electric field in the presence of larger cations. We further show that K⁺ and Cs⁺ cations can specifically adsorb on the catalyst and induce a surface reconstruction.

6.4 Materials and Methods

Materials. NH₄F (40 wt.% in H₂O), HF (48 wt.%), Cs₂CO₃ (99.995%; trace metals basis), Li₂CO₃ (99.999%; trace metals basis), and Cu foil (99.8%; metals basis, 0.025 mm

thick) were purchased from Fisher Scientific. $\text{CuSO}_4 \cdot 5\text{H}_2\text{O}$ (99.999%; trace metals basis), Na_2EDTA (99.0-101.0%; ACS Reagent), 2,2-bipyridine ($\geq 99\%$; ReagentPlus), HCHO (35 wt.%; 10% methanol as stabilizer), NaOH (99.99%; trace metals basis), KHCO_3 (99.95%; trace metal basis), and D_2O (99.9 atom %D) were purchased from Sigma Aldrich. Polycrystalline diamond pastes were purchased from South Bay Technologies (San Clemente, CA) or Electron Microscopy Sciences (Hatfield, PA). Ar (Ultra High Purity), CO (99.999%), CO_2 (5.0 research grade) were purchased from Air Gas. For all experiments, high purity water (18.2 M cm) derived from Barnstead Nanopure Diamond system (APS Water Services; Lake Balboa, CA) was used.

Cu Thin Film Deposition. A thin Cu film was deposited on a 60° Si prism using an electroless deposition techniques described in Chapter 3. After the Cu film deposition, it was assembled with a single compartment electrochemical cell and blanketed with 4 mL of either of 0.1 M MDCO_3 ($\text{M} = \text{Li}^+, \text{K}^+, \text{Cs}^+$) or 0.05 M M_2CO_3 ($\text{M} = \text{Li}^+, \text{Cs}^+$). Then, the electrolyte was purged with Ar gas for 20 min at 5 sccm rate. Cu film was electrochemically cleaned afterwards by cycling the potential between -0.13 and -0.6 V vs. Ag/AgCl at 50 mV/s scan rate. Immediately following this, electrochemical double layer capacitance measurements were collected by cycling the potential between -0.6 and -0.7 V vs. Ag/AgCl at 20, 40, 60, 80, and 100 mV/s scan rates, to determine the roughness factor of the Cu film (Details of the roughness factor determination of Cu thin films are given with the Figure 3.6). The resistance of the Cu film after deposition is $2 - 10 \Omega$ and the roughness factor is ≈ 10 .

Electrochemical Measurements. Electrochemical measurements were carried out using a VersaStat3 potentiostat (AMETEK; Berwyn, PA). The single compartment cell was assembled using a Ag/AgCl (RE-5B 3 M NaCl; BASi Inc.; West Lafayette, IN) and a Au wire (99.999%, Alfa Aesar) as the reference and counter electrodes, respectively. The Ag/AgCl reference electrode was calibrated against a saturated calomel electrode (CHI

150; CH Instruments Inc.; Austin, TX) prior to each experiment. The PEEK electrochemical cell was cleaned by immersing this in an acid solution (30 wt.% H₂SO₄ and 30 wt.% HNO₃) for 1 hour followed by sonication in Nanopure water for another 1 hour.

0.1 M bicarbonate solutions of Li⁺ and Cs⁺ cations were prepared by bubbling CO₂ at 10 sccm rate for 1 hour through 0.05 M Li₂CO₃ and Cs₂CO₃ solutions. 0.1 M KD₂CO₃ was prepared by hydrogen-deuterium exchange through dissolving KHCO₃ in water and subsequently evaporating the water.

ATR-SEIRAS Measurements.

The PEEK electrochemical cell was mounted on a commercial ATR accessory (VeeMax III; Pike Technologies; Madison, WI). Spectra were recorded with a nitrogen-purged Bruker Vertex 70 FTIR spectrometer (Billerica, MA) equipped with a liquid nitrogen-cooled MCT detector (FTIR-16; Infrared Associates; Stuart, FL). The change in optical density was calculated according to $\Delta mOD = -10^3 \log(S/R)$, with S and R referring to the single beam sample spectrum and single beam reference spectrum, respectively. The spectral resolution and the scanner velocity were 4 cm⁻¹ and 40 kHz, respectively, for CV experiments. During kinetic experiments, the spectral resolution and the scanner velocity were 16 cm⁻¹ and 160 kHz, respectively.

6.5 Acknowledgements

We gratefully acknowledge the financial support by the National Science Foundation (award no.: 1565948). C. M. G expresses gratitude to Vincent Ovalle for his support in data collection.

6.6 Original Publication

This chapter has been published: Gunathunge, C. M., Ovalle V. & Waegele, M. M, *Phys. Chem. Chem. Phys.* **19**, 30166 (2017).

Chapter 7

Summary and Future Perspective

In this thesis, we demonstrate that the properties of electrochemical interfaces evolve under applied potential and these dynamic interfacial properties govern the activity and selectivity of electrocatalytic processes. We overcome the challenge of *in-situ* probing of the interfacial properties by employing surface-enhanced IR absorption spectroscopy (SEIRAS) with surface-adsorbed CO (CO_{atop}) as a molecular probe. We illustrate strategies for the interpretation of the IR frequency data on the basis of the theories of CO chemisorption on transition metals, dynamical dipole coupling, chemical interactions between CO_{ads} , and the vibrational Stark effect. This approach enables the employment of the $\text{C}\equiv\text{O}$ stretch frequency as a powerful *in-situ* molecular probe of catalytic interfaces during catalytic operation. Improving catalysts for electrochemical processes is at the heart of achieving commercially viable catalysts for crucial reactions such as CO_2 reduction, CO oxidation, and biomass conversion. Understanding the interfacial properties under reaction conditions is key towards achieving this goal.

The studies presented in this thesis demonstrate that IR spectroscopy of CO_{ads} provides molecular-level insights into complex electrocatalytic interfaces. We showed that careful analysis of the lineshape of the broad CO_{atop} IR band enables the recognition of CO_{atop} adsorbed on surface sites with different coordination numbers (low frequency band, LFB $\approx 2050 \text{ cm}^{-1}$ and high frequency band, HFB $\approx 2080 \text{ cm}^{-1}$). Prudent investigation of

spectral properties such as peak frequency, lineshape, and integrated band areas of LFB and HFB, enables the identification of *in-situ* dynamics of the catalyst and double layer properties. We further demonstrated that the exploration of the potential dependence of the frequency, integrated band area, and lineshape of CO_{atop} and $\text{CO}_{\text{bridge}}$ during both cathodic and anodic potential scans reveals the origin of observed differences in activity and selectivity during CO_2RR at distinct reaction conditions, the knowledge which assist to forward the development of catalysts. In addition, a thorough inspection of the spectral bands such as bands arising from interfacial water or bicarbonate, together with the CO_{ads} band, gives rise to a comprehensive view of the electrochemical double layer.

As viewed throughout this thesis, advancements in ATR-SEIRAS have progressively contributed to comprehend electrocatalytic reactions within the past decade. Here we propose particular directions of possible improvements to the ATR-SEIRAS field, to strengthen the utilization of this technique in practical electrocatalysis.

- The majority of ATR-SEIRAS studies in electrocatalysis have been carried out on pure metal catalysts namely copper, platinum, palladium, rhodium, ruthenium, nickel, and silver thin films deposited on ATR prisms [197, 222–224]. Moving onward, the field can explore metal alloys or bimetallic catalysts as these catalysts have shown improved catalytic activity and selectivity in electrocatalytic processes [180, 225, 226]. There are handful of ATR-SEIRAS studies on metal alloy catalysts: $\text{Pt}_{0.27}\text{Fe}_{0.73}$ [227] and $\text{Pt}_{0.5}\text{Ru}_{0.5}$ [228] deposited on Si-ATR prisms using sputtering techniques and $\text{Pd}_{0.8}\text{Au}$ nanowires [229] and $\text{Pd}@\text{Pd}_3\text{Au}_7$ nanocubes [230] drop-casted on chemically deposited Au thin film on Si-ATR prisms. Exploration and development of the sputtering or chemical deposition techniques to acquire rough metal alloy thin films could open up a new avenue in usage of ATR-SEIRAS in electrocatalysis.

- Further amplifying the enhancement effect of ATR-SEIRAS to achieve increased sensitivity and time resolution is beneficial to its application in electrochemical investigations. Higher order of enhancement enables the detection of interfacial species with small absorption cross-section or lower population during catalytic operation. Moreover, with a better signal-to-noise ratio in fewer average scans, a faster time resolution can be achieved for capturing short-lived intermediates. It has been demonstrated that nanostructures, *e.g.* nanoantennas, varying in shapes, patterns, and materials, generate nanometer scale electromagnetic fields [231]. The resulting resonant SEIRAS can reach an enhancement factor of 10^5 , maximizing the sensitivity of this technique. One limitation of coupling this technique to electrochemical studies is the disperse nature of such nanostructures. To surmount this challenge, one could plant these discontinued nanostructures on graphene coated ATR element, [232] or employ inverse nanostructures, including nanoapertures/nanoslits decorated continuous metallic substrate for ATR-SEIRAS investigations [233, 234].
- An enhanced sensitivity and time resolution for ATR-SEIRAS with the aforementioned strategies open up novel research directions. Detection of adsorption site specific information from ATR-SEIRAS is impractical as the IR beam samples a wide area of the metal catalysts. Here we propose that, with higher ATR-SEIRAS sensitivity, combination of scanning electrochemical cell microscopy (SECCM) with ATR-SEIRAS as a feasible method to reach this goal. Further, single-atom catalysts (SACs) have emerged as a promising means of increasing the atom efficiency and activity of electrocatalytic reactions [235, 236]. With high sensitivity achieved, elucidation of reaction mechanisms on single-atom catalysts using ATR-SEIRAS is attainable.
- We further elaborate that combined SEIRAS and DEMS studies bring in new av-

enues in examining structure-reactivity properties in electrochemical reactions on thin electrodes used in SEIRAS techniques. As manifested in Chapter 5, the thin film catalysts used in SEIRAS studies do not always possess similar activity and product selectivity as their polycrystalline foils which are readily incorporated in reactivity studies. Nevertheless, further improvements to the cell described by Gunathunge *et al.* [158] are required to enhance its potential for structure-reactivity relationship investigations such as incorporation of thin flow cell configuration combining SEIRAS and DEMS to improve mass transport limitation and sampling efficiency of the DEMS system.

In Chapter 6, we highlight an approach for inferring electrochemical double layer properties using SEIRAS as a direct technique, especially with the C≡O stretch frequency of CO_{ads} as a molecular probe of the interface. The C≡O stretch frequency is highly dependent on the CO coverage as this is influenced by dynamical dipole coupling and chemical effects. Therefore, a relatively constant coverage of CO_{ads} should be maintained to acquire the potential dependence of the C≡O stretch frequency due to the vibrational Stark effect. Locating a constant CO coverage on copper electrodes is arduous due to the fact that adsorbed CO is an on pathway intermediate of important electrochemical reactions such as CO₂ reduction and CO oxidation. Other electrochemically inert molecules, whose coverage is relatively constant in a wide potential regime, could also be used as a probe of the interfacial electric field. For example, CO_{bridge} has been proved to be electrochemically inactive on copper electrode under cathodic potential relevant for CO/CO₂ reduction and therefore can be utilized as a molecular probe to investigate interfacial electric field at cathodic potentials where CO₂ reduction occurs.

Bibliography

1. Van der Ham, C. J. M., Koper, M. T. M. & Hetterscheid, D. G. H. Challenges in Reduction of Dinitrogen by Proton and Electron Transfer. *Chem. Soc. Rev.* **43**, 5183–5191 (15 2014).
2. Jiao, Y., Zheng, Y., Jaroniec, M. & Qiao, S. Z. Design of Electrocatalysts for Oxygen- and Hydrogen-Involving Energy Conversion Reactions. *Chem. Soc. Rev.* **44**, 2060–2086 (8 2015).
3. Kortlever, R., Shen, J., Schouten, K. J. P., Calle-Vallejo, F. & Koper, M. T. M. Catalysts and Reaction Pathways for the Electrochemical Reduction of Carbon Dioxide. *J. Phys. Chem. Lett.* **6**, 4073–4082 (2015).
4. Dunwell, M., Luc, W., Yan, Y., Jiao, F. & Xu, B. Understanding Surface-Mediated Electrochemical Reactions: CO₂ Reduction and Beyond. *ACS Catal.* **8**, 8121–8129 (2018).
5. Orella, M. J., Román-Leshkov, Y. & Brushett, F. R. Emerging Opportunities for Electrochemical Processing to Enable Sustainable Chemical Manufacturing. *Curr. Opin. Chem. Eng.* **20**, 159–167 (2018).
6. Yuan, Y. & Lei, A. Is Electrosynthesis Always Green and Advantageous Compared to Traditional Methods? *Nat. Commun.* **11**, 1–3 (2020).
7. Uitley, J. H. in *Fundamentals of Thermochemical Biomass Conversion* 1087–1102 (Springer, 1985).

8. Vuyyuru, K. R. & Strasser, P. Oxidation of Biomass Derived 5-Hydroxymethylfurfural using Heterogeneous and Electrochemical Catalysis. *Catal. Today* **195**, 144–154 (2012).
9. Hori, Y. & Suzuki, S. Electrolytic Reduction of Carbon Dioxide at Mercury Electrode in Aqueous Solution. *Bull. Chem. Soc. Jpn.* **55**, 660–665 (1982).
10. Kuhl, K. P., Cave, E. R., Abram, D. N. & Jaramillo, T. F. New Insights into the Electrochemical Reduction of Carbon Dioxide on Metallic Copper Surfaces. *Energ. Environ. Sci.* **5**, 7050–7059 (5 2012).
11. Xu, K., Chen, P., Li, X., Tong, Y., Ding, H., Wu, X., Chu, W., Peng, Z., Wu, C. & Xie, Y. Metallic Nickel Nitride Nanosheets Realizing Enhanced Electrochemical Water Oxidation. *J. Am. Chem. Soc.* **137**, 4119–4125 (2015).
12. Yan, Y., Xia, B. Y., Zhao, B. & Wang, X. A Review on Noble-Metal-Free Bifunctional Heterogeneous Catalysts for Overall Electrochemical Water Splitting. *J. Mater. Chem. A* **4**, 17587–17603 (45 2016).
13. Schouten, K. J. P., Kwon, Y., van der Ham, C. J. M., Qin, Z. & Koper, M. T. M. A New Mechanism for the Selectivity to C1 and C2 Species in the Electrochemical Reduction of Carbon Dioxide on Copper Electrodes. *Chem. Sci.* **2**, 1902–1909 (10 2011).
14. Ruckenstein, E. & Wang, H. Carbon Deposition and Catalytic Deactivation during CO₂ Reforming of CH₄ over Co/ γ -Al₂O₃ Catalysts. *J. Catal.* **205**, 289–293 (2002).
15. Popović, S., Smiljanić, M., Jovanović, P., Vavra, J., Buonsanti, R. & Hodnik, N. Stability and Degradation Mechanisms of Copper-Based Catalysts for Electrochemical CO₂ Reduction. *Angew. Chem. Int. Ed.* **59**, 14736–14746 (2020).
16. Whipple, D. T. & Kenis, P. J. A. Prospects of CO₂ Utilization via Direct Heterogeneous Electrochemical Reduction. *J. Phys. Chem. Lett.* **1**, 3451–3458 (2010).

17. Lai, S. C. S., Lebedeva, N. P., Housmans, T. H. M. & Koper, M. T. M. Mechanisms of Carbon Monoxide and Methanol Oxidation at Single-crystal Electrodes. *Top. in Catal.* **46**, 320–333 (2007).
18. Arán-Ais, R. M., Gao, D. & Roldan Cuenya, B. Structure- and Electrolyte-Sensitivity in CO₂ Electroreduction. *Acc. Chem. Res.* **51**, 2906–2917 (2018).
19. Holewinski, A., Xin, H., Nikolla, E. & Linic, S. Identifying Optimal Active Sites for Heterogeneous Catalysis by Metal Alloys Based on Molecular Descriptors and Electronic Structure Engineering. *Curr. Opin. Chem. Eng.* **2**, 312–319 (2013).
20. Holewinski, A., Idrobo, J.-C. & Linic, S. High-Performance Ag-Co Alloy Catalysts for Electrochemical Oxygen Reduction. *Nat. Chem.* **6**, 828–834 (2014).
21. Danilovic, N., Subbaraman, R., Strmcnik, D., Paulikas, A. P., Myers, D., Stamenkovic, V. R. & Markovic, N. M. The Effect of Noncovalent Interactions on the HOR, ORR, and HER on Ru, Ir, and Ru_{0.50}Ir_{0.50} Metal Surfaces in Alkaline Environments. *Electrocatalysis* **3**, 221–229 (2012).
22. Waegele, M. M., Gunathunge, C. M., Li, J. & Li, X. How Cations Affect the Electric Double Layer and the Rates and Selectivity of Electrocatalytic Processes. *J. Chem. Phys.* **151**, 160902 (2019).
23. Zhang, Z.-Q., Banerjee, S., Thoi, V. S. & Shoji Hall, A. Reorganization of Interfacial Water by an Amphiphilic Cationic Surfactant Promotes CO₂ Reduction. *J. Phys. Chem. Lett.* **11**, 5457–5463 (2020).
24. Koper, M. T. M. Theory of Multiple Proton-Electron Transfer Reactions and Its Implications for Electrocatalysis. *Chem. Sci.* **4**, 2710–2723 (2013).
25. Varela, A. S., Kroschel, M., Reier, T. & Strasser, P. Controlling the Selectivity of CO₂ Electroreduction on Copper: The Effect of the Electrolyte Concentration and the Importance of the Local pH. *Catal. Today* **260**, 8–13 (2016).

26. Zhang, F. & Co, A. C. Direct Evidence of Local pH Change and the Role of Alkali Cation during CO₂ Electroreduction in Aqueous Media. *Angew. Chem. Inter. Ed.* **59**, 1674–1681 (2020).
27. Ryu, J. & Surendranath, Y. Polarization-Induced Local pH Swing Promotes Pd-Catalyzed CO₂ Hydrogenation. *J. Am. Chem. Soc.* **142**, 13384–13390 (2020).
28. Remsing, R. C., McKendry, I. G., Strongin, D. R., Klein, M. L. & Zdilla, M. J. Frustrated Solvation Structures Can Enhance Electron Transfer Rates. *J. Phys. Chem. Lett.* **6**, 4804–4808 (2015).
29. Li, J., Li, X., Gunathunge, C. M. & Waegele, M. M. Hydrogen Bonding Steers the Product Selectivity of Electrocatalytic CO Reduction. *Proc. Natl. Acad. Sci. USA* **116**, 9220–9229 (2019).
30. Gunathunge, C. M., Li, X., Li, J., Hicks, R. P., Ovalle, V. J. & Waegele, M. M. Spectroscopic Observation of Reversible Surface Reconstruction of Copper Electrodes under CO₂ Reduction. *J. Phys. Chem. C* **121**, 12337–12344 (2017).
31. Medina-Ramos, J., Zhang, W., Yoon, K., Bai, P., Chemburkar, A., Tang, W., Atifi, A., Lee, S. S., Fister, T. T., Ingram, B. J., Rosenthal, J., Neurock, M., van Duin, A. C. T. & Fenter, P. Cathodic Corrosion at the Bismuth-Ionic Liquid Electrolyte Interface under Conditions for CO₂ Reduction. *Chem. Mater.* **30**, 2362–2373 (2018).
32. Yan, B., Krishnamurthy, D., Hendon, C. H., Deshpande, S., Surendranath, Y. & Viswanathan, V. Surface Restructuring of Nickel Sulfide Generates Optimally Coordinated Active Sites for Oxygen Reduction Catalysis. *Joule* **1**, 600–612 (2017).
33. Wang, H., Zhou, Y.-W. & Cai, W.-B. Recent Applications of *in situ* ATR-IR Spectroscopy in Interfacial Electrochemistry. *Curr. Opin. Electrochem.* **1**, 73–79 (2017).
34. Zhu, S., Li, T., Cai, W.-B. & Shao, M. CO₂ Electrochemical Reduction as Probed Through Infrared Spectroscopy. *ACS Energy Lett.* **4**, 682–689 (2019).

35. Kas, R., Ayemoba, O., Firet, N. J., Middelkoop, J., Smith, W. A. & Cuesta, A. In-Situ Infrared Spectroscopy Applied to the Study of the Electrocatalytic Reduction of CO₂: Theory, Practice and Challenges. *ChemPhysChem* **20**, 2904–2925 (2019).
36. Hori, Y., Murata, A. & Yoshinami, Y. Adsorption of CO, Intermediately Formed in Electrochemical Reduction of CO₂, at a Copper Electrode. *J. Chem. Soc., Faraday Trans.* **87**, 125–128 (1991).
37. Samjeské, G., Komatsu, K.-i. & Osawa, M. Dynamics of CO Oxidation on a Polycrystalline Platinum Electrode: A Time-Resolved Infrared Study. *J. Phys. Chem. C* **113**, 10222–10228 (2009).
38. Cabello, G., Davoglio, R. A., Marco, J. F. & Cuesta, A. Probing Electronic and Atomic Ensembles Effects on PtAu₃ Nanoparticles with CO Adsorption and Electrooxidation. *J. Electroanal. Chem.* **870**, 114233 (2020).
39. Hori, Y., Takahashi, I., Koga, O. & Hoshi, N. Selective Formation of C₂ Compounds from Electrochemical Reduction of CO₂ at a Series of Copper Single Crystal Electrodes. *J. Phys. Chem. B* **106**, 15–17 (2002).
40. García, G. & Koper, M. T. M. Stripping Voltammetry of Carbon Monoxide Oxidation on Stepped Platinum Single-Crystal Electrodes in Alkaline Solution. *Phys. Chem. Chem. Phys.* **10**, 3802–3811 (25 2008).
41. Durand, W. J., Peterson, A. A., Studt, F., Abild-Pedersen, F. & Nørskov, J. K. Structure Effects on the Energetics of the Electrochemical Reduction of CO₂ by Copper Surfaces. *Surf. Sci.* **605**, 1354–1359 (2011).
42. Tang, W., Peterson, A. A., Varela, A. S., Jovanov, Z. P., Bech, L., Durand, W. J., Dahl, S., Nørskov, J. K. & Chorkendorff, I. The Importance of Surface Morphology in Controlling the Selectivity of Polycrystalline Copper for CO₂ Electroreduction. *Phys. Chem. Chem. Phys.* **14**, 76–81 (1 2012).

43. Li, C. W. & Kanan, M. W. CO₂ Reduction at Low Overpotential on Cu Electrodes Resulting from the Reduction of Thick Cu₂O Films. *J. Am. Chem. Soc.* **134**, 7231–7234 (2012).
44. Wuttig, A., Yaguchi, M., Motobayashi, K., Osawa, M. & Surendranath, Y. Inhibited Proton Transfer Enhances Au-Catalyzed CO₂-to-Fuels Selectivity. *Proc. Natl. Acad. Sci. U.S.A.* **113**, E4585–E4593 (2016).
45. Eren, B., Zherebetsky, D., Patera, L. L., Wu, C. H., Bluhm, H., Africh, C., Wang, L.-W., Somorjai, G. A. & Salmeron, M. Activation of Cu(111) Surface by Decomposition into Nanoclusters Driven by CO Adsorption. *Science* **351**, 475–478 (2016).
46. Kim, Y.-G., Baricuatro, J. H., Javier, A., Gregoire, J. M. & Soriaga, M. P. The Evolution of the Polycrystalline Copper Surface, First to Cu(111) and Then to Cu(100), at a Fixed CO₂RR Potential: A Study by *Operando* EC-STM. *Langmuir* **30**, 15053–15056 (2014).
47. Kim, Y.-G., Javier, A., Baricuatro, J. H., Torelli, D., Cummins, K. D., Tsang, C. F., Hemminger, J. C. & Soriaga, M. P. Surface Reconstruction of Pure-Cu Single-Crystal Electrodes Under CO-Reduction Potentials in Alkaline Solutions: A Study by *Seriatim* ECSTM-DEMS. *J. Electroanal. Chem.* **780**, 290–295 (2016).
48. Gao, X., Hamelin, A. & Weaver, M. J. Potential-Dependent Reconstruction at Ordered Au(100)-Aqueous Interfaces as Probed by Atomic-Resolution Scanning Tunneling Microscopy. *Phys. Rev. Lett.* **67**, 618–621 (5 1991).
49. Resasco, J., Chen, L. D., Clark, E., Tsai, C., Hahn, C., Jaramillo, T. F., Chan, K. & Bell, A. T. Promoter Effects of Alkali Metal Cations on the Electrochemical Reduction of Carbon Dioxide. *J. Am. Chem. Soc.* **139**, 11277–11287 (2017).

50. Akhade, S. A., McCrum, I. T. & Janik, M. J. The Impact of Specifically Adsorbed Ions on the Copper-Catalyzed Electroreduction of CO₂. *J. Electrochem. Soc.* **163**, F477 (2016).
51. Hartstein, A., Kirtley, J. R. & Tsang, J. C. Enhancement of the Infrared Absorption from Molecular Monolayers with Thin Metal Overlayers. *Phys. Rev. Lett.* **45**, 201–204 (3 1980).
52. Osawa, M. Dynamic Processes in Electrochemical Reactions Studied by Surface-Enhanced Infrared Absorption Spectroscopy (SEIRAS). *Bull. Chem. Soc. Jpn.* **70**, 2861–2880 (1997).
53. Kawata, S., Ohtsu, M. & Irie, M. *Near-Field Optics and Surface Plasmon Polaritons* 163–187 (Springer Science & Business Media, 2001).
54. Osawa, M. & Ikeda, M. Surface-Enhanced Infrared Absorption of p-Nitrobenzoic Acid Deposited on Silver Island Films: Contributions of Electromagnetic and Chemical Mechanisms. *J. Phys. Chem.* **95**, 9914–9919 (1991).
55. Lu, G.-Q., Sun, S.-G., Chen, S.-P. & Cai, L.-R. Novel Properties of Dispersed Pt and Pd Thin Layers Supported on GC for CO Adsorption Studied Using In Situ MS-FTIR Reflection Spectroscopy. *J. Electroanal. Chem.* **421**, 19–23 (1997).
56. Lu, G.-Q., Sun, S.-G., Cai, L.-R., Chen, S.-P., Tian, Z.-W. & Shiu, K.-K. In Situ FTIR Spectroscopic Studies of Adsorption of CO, SCN⁻, and Poly(o-phenylenediamine) on Electrodes of Nanometer Thin Films of Pt, Pd, and Rh: Abnormal Infrared Effects (AIREs). *Langmuir* **16**, 778–786 (2000).
57. Aroca, R. & Price, B. A New Surface for Surface-Enhanced Infrared Spectroscopy: Tin Island Films. *J. Phys. Chem. B* **101**, 6537–6540 (1997).

58. Skibbe, O., Binder, M., Otto, A. & Pucci, A. Electronic Contributions to Infrared Spectra of Adsorbate Molecules on Metal Surfaces: Ethene on Cu(111). *J. Chem. Phys.* **128**, 194703 (2008).
59. Kraack, J. P., Kaech, A. & Hamm, P. Surface Enhancement in Ultrafast 2D ATR IR Spectroscopy at the Metal-Liquid Interface. *J. Phy. Chem. C* **120**, 3350–3359 (2016).
60. Kraack, J. P. & Hamm, P. Vibrational Ladder-Climbing in Surface-Enhanced, Ultrafast Infrared Spectroscopy. *Phys. Chem. Chem. Phys.* **18**, 16088–16093 (24 2016).
61. Osawa, M. & Ataka, K.-I. Electromagnetic Mechanism of Enhanced Infrared Absorption of Molecules Adsorbed on Metal Island Films. *Surf. Sci.* **262**, L118–L122 (1992).
62. Osawa, M., Ataka, K.-I., Yoshii, K. & Nishikawa, Y. Surface-Enhanced Infrared Spectroscopy: The Origin of the Absorption Enhancement and Band Selection Rule in the Infrared Spectra of Molecules Adsorbed on Fine Metal Particles. *Appl. Spectrosc.* **47**, 1497–1502 (1993).
63. Aroca, R. F., Ross, D. J. & Domingo, C. Surface-Enhanced Infrared Spectroscopy. *Appl. Spectrosc.* **58**, 324A–338A (2004).
64. Gunathunge, C. M., Ovalle, V. J., Li, Y., Janik, M. J. & Waegele, M. M. Existence of an Electrochemically Inert CO Population on Cu Electrodes in Alkaline pH. *ACS Catal.* **8**, 7507–7516 (2018).
65. Merklin, G. T. & Griffiths, P. R. Influence of Chemical Interactions on the Surface-Enhanced Infrared Absorption Spectrometry of Nitrophenols on Copper and Silver Films. *Langmuir* **13**, 6159–6163 (1997).

66. Ishida, K. P. & Griffiths, P. R. Theoretical and Experimental Investigation of Internal Reflection at Thin Copper Films Exposed to Aqueous Solutions. *Anal. Chem.* **66**, 522–530 (1994).
67. Zhu, S., Jiang, B., Cai, W.-B. & Shao, M. Direct Observation on Reaction Intermediates and the Role of Bicarbonate Anions in CO₂ Electrochemical Reduction Reaction on Cu Surfaces. *J. Am. Chem. Soc.* **139**, 15664–15667 (2017).
68. Firet, N. J. & Smith, W. A. Probing the Reaction Mechanism of CO₂ Electroreduction over Ag Films via Operando Infrared Spectroscopy. *ACS Catal.* **7**, 606–612 (2017).
69. Malkani, A. S., Dunwell, M. & Xu, B. Operando Spectroscopic Investigations of Copper and Oxide-Derived Copper Catalysts for Electrochemical CO Reduction. *ACS Catal.* **9**, 474–478 (2019).
70. Milosevic, M. *Internal Reflection and ATR Spectroscopy* (John Wiley & Sons, 2012).
71. Milosevic, M. On the Nature of the Evanescent Wave. *Appl. Spectrosc.* **67**, 126–131 (2013).
72. Griffiths, D. J. *Introduction to Electrodynamics* (Cambridge University Press, 2005).
73. Blyholder, G. Molecular Orbital View of Chemisorbed Carbon Monoxide. *J. Phys. Chem.* **68**, 2772–2777 (1964).
74. Hammer, B., Morikawa, Y. & Nørskov, J. K. CO Chemisorption at Metal Surfaces and Overlayers. *Phys. Rev. Lett.* **76**, 2141–2144 (12 1996).
75. Hammer, B., Nielsen, O. H. & Nørskov, J. Structure Sensitivity in Adsorption: CO Interaction with Stepped and Reconstructed Pt Surfaces. *Catal. Lett.* **46**, 31–35 (1997).

76. Cooper, V. R., Kolpak, A. M., Yourdshahyan, Y. & Rappe, A. M. Supported Metal Electronic Structure: Implications for Molecular Adsorption. *Phys. Rev. B* **72**, 081409 (8 2005).
77. Mason, S. E., Grinberg, I. & Rappe, A. M. Orbital-Specific Analysis of CO Chemisorption on Transition-Metal Surfaces. *J. Phys. Chem. C* **112**, 1963–1966 (2008).
78. Föhlisch, A., Nyberg, M., Bennich, P., Triguero, L., Hasselström, J., Karis, O., Pettersson, L. G. M. & Nilsson, A. The Bonding of CO to Metal Surfaces. *J. Chem. Phys.* **112**, 1946–1958 (2000).
79. Föhlisch, A., Nyberg, M., Hasselström, J., Karis, O., Pettersson, L. G. M. & Nilsson, A. How Carbon Monoxide Adsorbs in Different Sites. *Phys. Rev. Lett.* **85**, 3309–3312 (15 2000).
80. Hollins, P. & Pritchard, J. Infrared Studies of Chemisorbed Layers on Single Crystals. *Prog. Surf. Sci.* **19**, 275–349 (1985).
81. Vollmer, S., Witte, G. & Wöll, C. Determination of Site Specific Adsorption Energies of CO on Copper. *Catal. Lett.* **77**, 97–101 (2001).
82. Nakamura, I., Takahashi, A & Fujitani, T. Selective Dissociation of O₃ and Adsorption of CO on Various Au Single Crystal Surfaces. *Catal. Lett.* **129**, 400–403 (2009).
83. Piccolo, L., Loffreda, D., Cadete Santos Aires, F. J., Deranlot, C., Jugnet, Y., Sautet, P. & Bertolini, J. C. The Adsorption of CO on Au (111) at Elevated Pressures Studied by STM, RAIRS and DFT Calculations. *Surf. Sci.* **566**, 995–1000 (2004).
84. Hussain, A., Ferré, D. C., Gracia, J., Nieuwenhuys, B. & Niemantsverdriet, J. DFT Study of CO and NO Adsorption on Low Index and Stepped Surfaces of Gold. *Surf. Sci.* **603**, 2734–2741 (2009).

85. Mehmood, F., Kara, A., Rahman, T. S. & Henry, C. R. Comparative Study of CO Adsorption on Flat, Stepped, and Kinked Au Surfaces Using Density Functional Theory. *Phys. Rev. B* **79**, 075422 (7 2009).
86. Mavrikakis, M., Stoltze, P. & Nørskov, J. K. Making Gold Less Noble. *Catal. Lett.* **64**, 101–106 (2000).
87. Meier, D. C., Bukhtiyarov, V. & Goodman, D. W. CO Adsorption on Au(110)–(1×2): An IRAS Investigation. *J. Phys. Chem. B* **107**, 12668–12671 (2003).
88. Kim, J., Samano, E. & Koel, B. E. CO Adsorption and Reaction on Clean and Oxygen-Covered Au(211) Surfaces. *J. Phys. Chem. B* **110**, 17512–17517 (2006).
89. Ruggiero, C. & Hollins, P. Adsorption of Carbon Monoxide on the Gold(332) Surface. *J. Chem. Soc., Faraday Trans.* **92**, 4829–4834 (23 1996).
90. Yim, W.-L., Nowitzki, T., Necke, M., Schnars, H., Nickut, P., Biener, J., Biener, M. M., Zielasek, V., Al-Shamery, K., Klüner, T. & Bäumer, M. Universal Phenomena of CO Adsorption on Gold Surfaces with Low-Coordinated Sites. *J. Phys. Chem. C* **111**, 445–451 (2007).
91. Tüshaus, M., Schweizer, E., Hollins, P. & Bradshaw, A. M. Yet Another Vibrational Study of the Adsorption System Pt(111)-CO. *J. Electron Spectrosc.* **44**, 305–316 (1987).
92. Bradshaw, A. & Hoffmann, F. The Chemisorption of Carbon Monoxide on Palladium Single Crystal Surfaces: IR Spectroscopic Evidence for Localised Site Adsorption. *Surf. Sci.* **72**, 513–535 (1978).
93. Conrad, H., Ertl, G., Koch, J. & Latta, E. Adsorption of CO on Pd Single Crystal Surfaces. *Surf. Sci.* **43**, 462–480 (1974).

94. Ortega, A., Huffman, F. & Bradshaw, A. The Adsorption of CO on Pd(100) Studied by IR Reflection Absorption Spectroscopy. *Surf. Sci.* **119**, 79–94 (1982).
95. Raval, R., Harrison, M. & King, D. Temperature Effects in Compression Structures: Carbon Monoxide on Pd(110) by RAIRS. *Surf. Sci.* **211-212**, 61–70 (1989).
96. Eren, B., Liu, Z., Stacchiola, D., Somorjai, G. A. & Salmeron, M. Structural Changes of Cu(110) and Cu(110)-(2×1)-O Surfaces Under Carbon Monoxide in the Torr Pressure Range Studied with Scanning Tunneling Microscopy and Infrared Reflection Absorption Spectroscopy. *J. Phys. Chem. C* **120**, 8227–8231 (2016).
97. Hori, Y., Koga, O., Watanabe, Y. & Matsuo, T. FTIR Measurements of Charge Displacement Adsorption of CO on Poly- and Single Crystal (100) of Cu Electrodes. *Electrochim. Acta* **44**, 1389–1395 (1998).
98. Koga, O., Teruya, S., Matsuda, K., Minami, M., Hoshi, N. & Hori, Y. Infrared Spectroscopic and Voltammetric Study of Adsorbed CO on Stepped Surfaces of Copper Monocrystalline Electrodes. *Electrochim. Acta* **50**, 2475–2485 (2005).
99. Bagus, P. & Pacchioni, G. Electric Field Effects on the Surface-Adsorbate Interaction: Cluster Model Studies. *Electrochim. Acta* **36**, 1669–1675 (1991).
100. Head-Gordon, M. & Tully, J. C. Electric Field Effects on Chemisorption and Vibrational Relaxation of CO on Cu(100). *Chem. Phys.* **175**, 37–51 (1993).
101. Woodruff, D., Hayden, B., Prince, K. & Bradshaw, A. Dipole Coupling and Chemical Shifts in IRAS of CO Adsorbed on Cu(110). *Surf. Sci.* **123**, 397–412 (1982).
102. Hamm, P., Lim, M. & Hochstrasser, R. M. Structure of the Amide I Band of Peptides Measured by Femtosecond Nonlinear-Infrared Spectroscopy. *J. Phys. Chem. B* **102**, 6123–6138 (1998).

103. Borguet, E. & Dai, H.-L. Site-Specific Properties and Dynamical Dipole Coupling of CO Molecules Adsorbed on a Vicinal Cu(100) Surface. *J. Chem. Phys.* **101**, 9080–9095 (1994).
104. Hollins, P. & Pritchard, J. Interactions of CO Molecules Adsorbed on Cu(111). *Surf. Sci.* **89**, 486–495 (1979).
105. Helmholtz, H. Ueber einige Gesetze der Vertheilung elektrischer Ströme in körperlichen Leitern mit Anwendung auf die thierisch-elektrischen Versuche. *Annalen der Physik* **165**, 211–233 (1853).
106. Faulkner, L. R. & Bard, A. J. *Electrochemical Methods: Fundamentals and Applications* chap. 13 (John Wiley and Sons, 2002).
107. Eliaz, N. & Gileadi, E. *Physical Electrochemistry: Fundamentals, Techniques, and Applications* (John Wiley & Sons, 2019).
108. Magnussen, O. M. & Groß, A. Toward an Atomic-Scale Understanding of Electrochemical Interface Structure and Dynamics. *J. Am. Chem. Soc.* **141**, 4777–4790 (2019).
109. Gunathunge, C. M., Ovalle, V. J. & Waegele, M. M. Probing Promoting Effects of Alkali Cations on the Reduction of CO at the Aqueous Electrolyte/Copper Interface. *Phys. Chem. Chem. Phys.* **19**, 30166–30172 (44 2017).
110. Ovalle, V. J. & Waegele, M. M. Understanding the Impact of N-Arylpyridinium Ions on the Selectivity of CO₂ Reduction at the Cu/Electrolyte Interface. *J. Phys. Chem. C* **123**, 24453–24460 (2019).
111. Ovalle, V. J. & Waegele, M. M. Impact of Electrolyte Anions on the Adsorption of CO on Cu Electrodes. *J. Phys. Chem. C* **124**, 14713–14721 (2020).

112. Grahame, D. C. The Electrical Double Layer and the Theory of Electrocapillarity. *Chem. Rev.* **41**, 441–501 (1947).
113. Bockris, J. O., Devanathan, M. A. V., Müller, K. & Butler, J. A. V. On the Structure of Charged Interfaces. *P. Roy. Soc. A-Math. Phys.* **274**, 55–79 (1963).
114. Delahay, P. Double Layer Studies. *J. Electrochem. Soc.* **113**, 967 (1966).
115. Favaro, M., Jeong, B., Ross, P. N., Yano, J., Hussain, Z., Liu, Z. & Crumlin, E. J. Unravelling the Electrochemical Double Layer by Direct Probing of the Solid/Liquid Interface. *Nat. Commun.* **7**, 1–8 (2016).
116. Liu, Y., Kawaguchi, T., Pierce, M. S., Komanicky, V. & You, H. Layering and Ordering in Electrochemical Double Layers. *J. Phys. Chem. Lett.* **9**, 1265–1271 (2018).
117. Sorenson, S. A., Patrow, J. G. & Dawlaty, J. M. Solvation Reaction Field at the Interface Measured by Vibrational Sum Frequency Generation Spectroscopy. *J. Am. Chem. Soc.* **139**, 2369–2378 (2017).
118. Patrow, J. G., Sorenson, S. A. & Dawlaty, J. M. Direct Spectroscopic Measurement of Interfacial Electric Fields near an Electrode under Polarizing or Current-Carrying Conditions. *J. Phys. Chem. C* **121**, 11585–11592 (2017).
119. Ge, A., Videla, P. E., Lee, G. L., Rudshiteyn, B., Song, J., Kubiak, C. P., Batista, V. S. & Lian, T. Interfacial Structure and Electric Field Probed by In Situ Electrochemical Vibrational Stark Effect Spectroscopy and Computational Modeling. *J. Phys. Chem. C* **121**, 18674–18682 (2017).
120. Gewirth, A. A. & Niece, B. K. Electrochemical Applications of in Situ Scanning Probe Microscopy. *Chem. Rev.* **97**, 1129–1162 (1997).

121. Itaya, K. In Situ Scanning Tunneling Microscopy in Electrolyte Solutions. *Prog. Surf. Sci.* **58**, 121–247 (1998).
122. Schnur, S. & Groß, A. Properties of Metal-Water Interfaces Studied From First Principles. *New J. Phys.* **11**, 125003 (2009).
123. Sakong, S. & Groß, A. The Electric Double Layer at Metal-Water Interfaces Revisited Based on a Charge Polarization Scheme. *J. Chem. Phys.* **149**, 084705 (2018).
124. Gorin, C. F., Beh, E. S. & Kanan, M. W. An Electric Field-Induced Change in the Selectivity of a Metal Oxide-Catalyzed Epoxide Rearrangement. *J. Am. Chem. Soc.* **134**, 186–189 (2012).
125. Chen, L. D., Urushihara, M., Chan, K. & Nørskov, J. K. Electric Field Effects in Electrochemical CO₂ Reduction. *ACS Catal.* **6**, 7133–7139 (2016).
126. Chattopadhyay, A. & Boxer, S. G. Vibrational Stark Effect Spectroscopy. *J. Am. Chem. Soc.* **117**, 1449–1450 (1995).
127. Lambert, D. K. Vibrational Stark Effect of Adsorbates at Electrochemical Interfaces. *Electrochimica Acta* **41**, 623–630 (1996).
128. Weaver, M. J. & Wasileski, S. A. Influence of Double-Layer Solvation on Local versus Macroscopic Surface Potentials on Ordered Platinum-Group Metals as Sensed by the Vibrational Stark Effect. *Langmuir* **17**, 3039–3043 (2001).
129. Fried, S. D. & Boxer, S. G. Measuring Electric Fields and Noncovalent Interactions Using the Vibrational Stark Effect. *Acc. Chem. Res.* **48**, 998–1006 (2015).
130. Singh, M. R., Kwon, Y., Lum, Y., Ager, J. W. & Bell, A. T. Hydrolysis of Electrolyte Cations Enhances the Electrochemical Reduction of CO₂ over Ag and Cu. *J. Am. Chem. Soc.* **138**, 13006–13012 (2016).

131. Hori, Y., Kikuchi, K. & Suzuki, S. Production of CO and CH₄ in Electrochemical Reduction of CO₂ at Metal Electrodes in Aqueous Hydrogencarbonate Solution. *Chem. Lett.* **14**, 1695–1698 (1985).
132. Schouten, K. J. P., Qin, Z., Pérez Gallent, E. & Koper, M. T. M. Two Pathways for the Formation of Ethylene in CO Reduction on Single-Crystal Copper Electrodes. *J. Am. Chem. Soc.* **134**, 9864–9867 (2012).
133. Nie, X., Esopi, M. R., Janik, M. J. & Asthagiri, A. Selectivity of CO₂ Reduction on Copper Electrodes: The Role of the Kinetics of Elementary Steps. *Angew. Chem., Int. Ed.* **52**, 2459–2462 (2013).
134. Kuhl, K. P., Hatsukade, T., Cave, E. R., Abram, D. N., Kibsgaard, J. & Jaramillo, T. F. Electrocatalytic Conversion of Carbon Dioxide to Methane and Methanol on Transition Metal Surfaces. *J. Am. Chem. Soc.* **136**, 14107–14113 (2014).
135. Goodpaster, J. D., Bell, A. T. & Head-Gordon, M. Identification of Possible Pathways for C-C Bond Formation during Electrochemical Reduction of CO₂: New Theoretical Insights from an Improved Electrochemical Model. *J. Phys. Chem. Lett.* **7**, 1471–1477 (2016).
136. Xiao, H., Cheng, T. & Goddard, W. A. Atomistic Mechanisms Underlying Selectivities in C₁ and C₂ Products from Electrochemical Reduction of CO on Cu(111). *J. Am. Chem. Soc.* **139**, 130–136 (2017).
137. White, J. L., Baruch, M. F., Pander, J. E., Hu, Y., Fortmeyer, I. C., Park, J. E., Zhang, T., Liao, K., Gu, J., Yan, Y., Shaw, T. W., Abelev, E. & Bocarsly, A. B. Light-Driven Heterogeneous Reduction of Carbon Dioxide: Photocatalysts and Photoelectrodes. *Chem. Rev.* **115**, 12888–12935 (2015).

138. Hori, Y., Murata, A., Takahashi, R. & Suzuki, S. Electrochemical Reduction of Carbon Monoxide to Hydrocarbons at Various Metal Electrodes in Aqueous Solution. *Chem. Lett.* **16**, 1665–1668 (1987).
139. Hori, Y., Murata, A. & Takahashi, R. Formation of Hydrocarbons in the Electrochemical Reduction of Carbon Dioxide at a Copper Electrode in Aqueous Solution. *J. Chem. Soc., Faraday Trans. 1* **85**, 2309–2326 (8 1989).
140. Gattrell, M., Gupta, N. & Co, A. A Review of the Aqueous Electrochemical Reduction of CO₂ to Hydrocarbons at Copper. *J. Electroanal. Chem.* **594**, 1–19 (2006).
141. Hori, Y., Koga, O., Yamazaki, H. & Matsuo, T. Infrared Spectroscopy of Adsorbed CO and Intermediate Species in Electrochemical Reduction of CO₂ to Hydrocarbons on a Cu Electrode. *Electrochim. Acta* **40**, 2617–2622 (1995).
142. Schouten, K., Pérez Gallent, E. & Koper, M. Structure Sensitivity of the Electrochemical Reduction of Carbon Monoxide on Copper Single Crystals. *ACS Catal.* **3**, 1292–1295 (2013).
143. Luo, W., Nie, X., Janik, M. J. & Asthagiri, A. Facet Dependence of CO₂ Reduction Paths on Cu Electrodes. *ACS Catal.* **6**, 219–229 (2016).
144. Huang, Y., Handoko, A. D., Hirunsit, P. & Yeo, B. S. Electrochemical Reduction of CO₂ Using Copper Single-Crystal Surfaces: Effects of CO* Coverage on the Selective Formation of Ethylene. *ACS Catal.* **7**, 1749–1756 (2017).
145. Loiudice, A., Lobaccaro, P., Kamali, E. A., Thao, T., Huang, B. H., Ager, J. W. & Buonsanti, R. Tailoring Copper Nanocrystals towards C₂ Products in Electrochemical CO₂ Reduction. *Angew. Chem. Int. Ed.* **55**, 5789–5792 (2016).
146. Wuttig, A., Liu, C., Peng, Q., Yaguchi, M., Hendon, C. H., Motobayashi, K., Ye, S., Osawa, M. & Surendranath, Y. Tracking a Common Surface-Bound Intermediate During CO₂-to-Fuels Catalysis. *ACS Cent. Sci.* **2**, 522–528 (2016).

147. Li, C. W., Ciston, J. & Kanan, M. W. Electroreduction of Carbon Monoxide to Liquid Fuel on Oxide-Derived Nanocrystalline Copper. *Nature* **508**, 504–507 (2014).
148. Hori, Y., Murata, A., Tsukamoto, T., Wakebe, H., Koga, O. & Yamazaki, H. Adsorption of Carbon Monoxide at a Copper Electrode Accompanied by Electron Transfer Observed by Voltammetry and IR Spectroscopy. *Electrochim. Acta* **39**, 2495–2500 (1994).
149. Smith, B. D., Irish, D. E., Kedzierzawski, P. & Augustynski, J. A Surface Enhanced Raman Scattering Study of the Intermediate and Poisoning Species Formed during the Electrochemical Reduction of CO₂ on Copper. *J. Electrochem. Soc.* **144**, 4288–4296 (1997).
150. Hirschmugl, C. J., Williams, G. P., Hoffmann, F. M. & Chabal, Y. J. Adsorbate-Substrate Resonant Interactions Observed for CO on Cu(100) in the Far Infrared. *Phys. Rev. Lett.* **65**, 480–483 (4 1990).
151. Akemann, W. & Otto, A. Vibrational Modes of CO Adsorbed on Disordered Copper Films. *J Raman Spectrosc.* **22**, 797–803 (1991).
152. Campion, A. & Kambhampati, P. Surface-Enhanced Raman Scattering. *Chem. Soc. Rev.* **27**, 241–250 (4 1998).
153. Waszczuk, P., Zelenay, P. & Sobkowski, J. Surface Interaction of Benzoic Acid with a Copper Electrode. *Electrochim. Acta* **40**, 1717–1721 (1995).
154. Hori, Y., Takahashi, R., Yoshinami, Y. & Murata, A. Electrochemical Reduction of CO at a Copper Electrode. *J. Phys. Chem. B* **101**, 7075–7081 (1997).
155. Peterson, A. A., Abild-Pedersen, F., Studt, F., Rossmeisl, J. & Nørskov, J. K. How Copper Catalyzes the Electroreduction of Carbon Dioxide into Hydrocarbon Fuels. *Energy Environ. Sci.* **3**, 1311–1315 (9 2010).

156. Calle-Vallejo, F. & Koper, M. T. M. Theoretical Considerations on the Electroreduction of CO to C₂ Species on Cu(100) Electrodes. *Ange. Chem. Int. Ed.* **52**, 7282–7285 (2013).
157. Zhang, Y.-J., Sethuraman, V., Michalsky, R. & Peterson, A. A. Competition between CO₂ Reduction and H₂ Evolution on Transition-Metal Electrocatalysts. *ACS Catal.* **4**, 3742–3748 (2014).
158. Gunathunge, C. M., Li, J., Li, X., Hong, J. J. & Waagele, M. M. Revealing the Predominant Surface Facets of Rough Cu Electrodes under Electrochemical Conditions. *ACS Catal.* **10**, 6908–6923 (2020).
159. Salimon, J, Hernández-Romero, R. & Kalaji, M. The Dynamics of the Conversion of Linear to Bridge Bonded CO on Cu. *J. Electroanal. Chem.* **538-539**, 99–108 (2002).
160. Shaw, S. K., Berná, A., Feliu, J. M., Nichols, R. J., Jacob, T. & Schiffrin, D. J. Role of Axially Coordinated Surface Sites for Electrochemically Controlled Carbon Monoxide Adsorption on Single Crystal Copper Electrodes. *Phys. Chem. Chem. Phys.* **13**, 5242–5251 (12 2011).
161. Verdaguer-Casadevall, A., Li, C. W., Johansson, T. P., Scott, S. B., McKeown, J. T., Kumar, M., Stephens, I. E. L., Kanan, M. W. & Chorkendorff, I. Probing the Active Surface Sites for CO Reduction on Oxide-Derived Copper Electrocatalysts. *J. Am. Chem. Soc.* **137**, 9808–9811 (2015).
162. Ma, S., Sadakiyo, M., Luo, R., Heima, M., Yamauchi, M. & Kenis, P. J. One-Step Electrosynthesis of Ethylene and Ethanol from CO₂ in an Alkaline Electrolyzer. *J. Power Sources* **301**, 219–228 (2016).

163. Reller, C., Krause, R., Volkova, E., Schmid, B., Neubauer, S., Rucki, A., Schuster, M. & Schmid, G. Selective Electroreduction of CO₂ toward Ethylene on Nano Dendritic Copper Catalysts at High Current Density. *Adv. Energy Mater.* **7**, 1602114 (2017).
164. Bertheussen, E., Hogg, T. V., Abghoui, Y., Engstfeld, A. K., Chorkendorff, I. & Stephens, I. E. L. Electroreduction of CO on Polycrystalline Copper at Low Overpotentials. *ACS Energy Lett.* **3**, 634–640 (2018).
165. Dinh, C.-T., Burdyny, T., Kibria, M. G., Seifitokaldani, A., Gabardo, C. M., García de Arquer, F. P., Kiani, A., Edwards, J. P., De Luna, P., Bushuyev, O. S., Zou, C., Quintero-Bermudez, R., Pang, Y., Sinton, D. & Sargent, E. H. CO₂ Electroreduction to Ethylene via Hydroxide-Mediated Copper Catalysis at an Abrupt Interface. *Science* **360**, 783–787 (2018).
166. Kim, Y.-G. & Soriaga, M. P. Cathodic Regeneration of a Clean and Ordered Cu(100)-(1 × 1) Surface from an Air-Oxidized and Disordered Electrode: An Operando STM Study. *J. Electroanal. Chem.* **734**, 7–9 (2014).
167. Lobaccaro, P., Singh, M. R., Clark, E. L., Kwon, Y., Bell, A. T. & Ager, J. W. Effects of Temperature and Gas-Liquid Mass Transfer on the Operation of Small Electrochemical Cells for the Quantitative Evaluation of CO₂ Reduction Electrocatalysts. *Phys. Chem. Chem. Phys.* **18**, 26777–26785 (38 2016).
168. Li, X., Gunathunge, C. M., Agrawal, N., Montalvo-Castro, H., Jin, J., Janik, M. J. & Waegle, M. M. Impact of Alkali Metal Cations and Iron Impurities on the Evolution of Hydrogen on Cu Electrodes in Alkaline Electrolytes. *J. Electrochem. Soc.* **167**, 106505 (2020).
169. Tornquist, W., Guillaume, F. & Griffin, G. L. Vibrational Behavior of Carbon Monoxide Adsorbed on Platinum in Nonacidic Electrolytes. *Langmuir* **3**, 477–483 (1987).

170. Cuesta, A. & Gutiérrez, C. Study by Fourier Transform Infrared Spectroscopy of the Adsorption of Carbon Monoxide on a Nickel Electrode at pH 3-14. *Langmuir* **14**, 3397–3404 (1998).
171. Cuesta, A. & Gutiérrez, C. Study by Fourier Transform Infrared Spectroscopy of the Adsorption of Carbon Monoxide on a Cobalt Electrode at pH 3-14. *Langmuir* **14**, 3390–3396 (1998).
172. Couto, A., Rincón, A., Pérez, M. & Gutiérrez, C. Adsorption and Electrooxidation of Carbon Monoxide on Polycrystalline Platinum at pH 0.3-13. *Electrochim. Acta* **46**, 1285–1296 (2001).
173. Yau, S. L., Gao, X., Chang, S. C., Schardt, B. C. & Weaver, M. J. Atomic-Resolution Scanning Tunneling Microscopy and Infrared Spectroscopy as Combined In Situ Probes of Electrochemical Adlayer Structure: Carbon Monoxide on Rhodium (111). *J. Am. Chem. Soc.* **113**, 6049–6056 (1991).
174. Gileadi, E., Argade, S. D. & Bockris, J. O. The Potential of Zero Charge of Platinum and Its pH Dependence. *J. Phys. Chem.* **70**, 2044–2046 (1966).
175. Manthiram, K., Beberwyck, B. J. & Alivisatos, A. P. Enhanced Electrochemical Methanation of Carbon Dioxide with a Dispersible Nanoscale Copper Catalyst. *J. Am. Chem. Soc.* **136**, 13319–13325 (2014).
176. Roberts, F. S., Kuhl, K. P. & Nilsson, A. High Selectivity for Ethylene from Carbon Dioxide Reduction over Copper Nanocube Electrocatalysts. *Angew. Chem. Int. Ed.* **54**, 5179–5182 (2015).
177. Hoang, T. T. H., Ma, S., Gold, J. I., Kenis, P. J. A. & Gewirth, A. A. Nanoporous Copper Films by Additive-Controlled Electrodeposition: CO₂ Reduction Catalysis. *ACS Catal.* **7**, 3313–3321 (2017).

178. Wang, L., Nitopi, S., Wong, A. B., Snider, J. L., Nielander, A. C., Morales-Guio, C. G., Orazov, M., Higgins, D. C., Hahn, C. & Jaramillo, T. F. Electrochemically Converting Carbon Monoxide to Liquid Fuels by Directing Selectivity with Electrode Surface Area. *Nat. Catal.* **2**, 702–708 (2019).
179. Liu, M., Pang, Y., Zhang, B., De Luna, P., Voznyy, O., Xu, J., Zheng, X., Dinh, C. T., Fan, F., Cao, C., *et al.* Enhanced Electrocatalytic CO₂ Reduction via Field-Induced Reagent Concentration. *Nature* **537**, 382–386 (2016).
180. Chen, X., Henckel, D. A., Nwabara, U. O., Li, Y., Frenkel, A. I., Fister, T. T., Kenis, P. J. A. & Gewirth, A. A. Controlling Speciation during CO₂ Reduction on Cu-Alloy Electrodes. *ACS Catal.* **10**, 672–682 (2020).
181. De Luna, P., Quintero-Bermudez, R., Dinh, C.-T., Ross, M. B., Bushuyev, O. S., Todorović, P., Regier, T., Kelley, S. O., Yang, P. & Sargent, E. H. Catalyst Electro-Redeposition Controls Morphology and Oxidation State for Selective Carbon Dioxide Reduction. *Nat. Catal.* **1**, 103–110 (2018).
182. Kas, R., Kortlever, R., Ylmaz, H., Koper, M. T. M. & Mul, G. Manipulating the Hydrocarbon Selectivity of Copper Nanoparticles in CO₂ Electroreduction by Process Conditions. *ChemElectroChem* **2**, 354–358 (2015).
183. Dutta, A., Rahaman, M., Luedi, N. C., Mohos, M. & Broekmann, P. Morphology Matters: Tuning the Product Distribution of CO₂ Electroreduction on Oxide-Derived Cu Foam Catalysts. *ACS Catal.* **6**, 3804–3814 (2016).
184. Raciti, D., Cao, L., Livi, K. J. T., Rottmann, P. F., Tang, X., Li, C., Hicks, Z., Bowen, K. H., Hemker, K. J., Mueller, T. & Wang, C. Low-Overpotential Electroreduction of Carbon Monoxide Using Copper Nanowires. *ACS Catal.* **7**, 4467–4472 (2017).
185. Lv, J.-J., Jouny, M., Luc, W., Zhu, W., Zhu, J.-J. & Jiao, F. A Highly Porous Copper Electrocatalyst for Carbon Dioxide Reduction. *Adv. Mater.* **30**, 1803111 (2018).

186. Kim, C., Jeon, H. S., Eom, T., Jee, M. S., Kim, H., Friend, C. M., Min, B. K. & Hwang, Y. J. Achieving Selective and Efficient Electrocatalytic Activity for CO₂ Reduction Using Immobilized Silver Nanoparticles. *J. Am. Chem. Soc.* **137**, 13844–13850 (2015).
187. Kim, D., Kley, C. S., Li, Y. & Yang, P. Copper Nanoparticle Ensembles for Selective Electroreduction of CO₂ to C₂-C₃ Products. *Proc. Natl. Acad. Sci. U. S. A.* **114**, 10560–10565 (2017).
188. Kauffman, D. R., Alfonso, D. R., Tafen, D. N., Wang, C., Zhou, Y., Yu, Y., Lekse, J. W., Deng, X., Espinoza, V., Trindell, J., Ranasingha, O. K., Roy, A., Lee, J.-S. & Xin, H. L. Selective Electrocatalytic Reduction of CO₂ into CO at Small, Thiol-Capped Au/Cu Nanoparticles. *J. Phys. Chem. C* **122**, 27991–28000 (2018).
189. Yoon, Y., Hall, A. S. & Surendranath, Y. Tuning of Silver Catalyst Mesostructure Promotes Selective Carbon Dioxide Conversion into Fuels. *Angew. Chem., Int. Ed.* **55**, 15282–15286 (2016).
190. Nguyen-Phan, T.-D., Wang, C., Marin, C. M., Zhou, Y., Stavitski, E., Popczun, E. J., Yu, Y., Xu, W., Howard, B. H., Stuckman, M. Y., Waluyo, I., Ohodnicki, P. R. & Kauffman, D. R. Understanding Three-Dimensionally Interconnected Porous Oxide-Derived Copper Electrocatalyst for Selective Carbon Dioxide Reduction. *J. Mater. Chem. A* **7**, 27576–27584 (48 2019).
191. Chen, C. S., Handoko, A. D., Wan, J. H., Ma, L., Ren, D. & Yeo, B. S. Stable and Selective Electrochemical Reduction of Carbon Dioxide to Ethylene on Copper Mesocrystals. *Catal. Sci. Technol.* **5**, 161–168 (1 2015).
192. Kwon, Y., Lum, Y., Clark, E. L., Ager, J. W. & Bell, A. T. CO₂ Electroreduction with Enhanced Ethylene and Ethanol Selectivity by Nanostructuring Polycrystalline Copper. *ChemElectroChem* **3**, 1012–1019 (2016).

193. Gao, D., Scholten, F. & Roldan Cuenya, B. Improved CO₂ Electroreduction Performance on Plasma-Activated Cu Catalysts via Electrolyte Design: Halide Effect. *ACS Catal.* **7**, 5112–5120 (2017).
194. Gao, D., Sinev, I., Scholten, F., Arán-Ais, R. M., Divins, N. J., Kvashnina, K., Timoshenko, J. & Roldan Cuenya, B. Selective CO₂ Electroreduction to Ethylene and Multicarbon Alcohols via Electrolyte-Driven Nanostructuring. *Angew. Chem. Int. Ed.* **58**, 17047–17053 (2019).
195. Hori, Y., Takahashi, I., Koga, O. & Hoshi, N. Electrochemical Reduction of Carbon Dioxide at Various Series of Copper Single Crystal Electrodes. *J. Mol. Catal. A: Chem.* **199**, 39–47 (2003).
196. Wang, H.-F., Yan, Y.-G., Huo, S.-J., Cai, W.-B., Xu, Q.-J. & Osawa, M. Seeded Growth Fabrication of Cu-on-Si Electrodes for In Situ ATR-SEIRAS Applications. *Electrochim. Acta* **52**, 5950–5957 (2007).
197. Miyake, H., Ye, S. & Osawa, M. Electroless Deposition of Gold Thin Films on Silicon for Surface-Enhanced Infrared Spectroelectrochemistry. *Electrochem. Commun.* **4**, 973–977 (2002).
198. Heyes, J., Dunwell, M. & Xu, B. CO₂ Reduction on Cu at Low Overpotentials with Surface-Enhanced in Situ Spectroscopy. *J. Phys. Chem. C* **120**, 17334–17341 (2016).
199. Schouten, K. J. P., Pérez Gallent, E. & Koper, M. T. M. The Influence of pH on the Reduction of CO and CO₂ to Hydrocarbons on Copper Electrodes. *J. Electroanal. Chem.* **716**, 53–57 (2014).
200. Roberts, F. S., Kuhl, K. P. & Nilsson, A. Electroreduction of Carbon Monoxide Over a Copper Nanocube Catalyst: Surface Structure and pH Dependence on Selectivity. *ChemCatChem* **8**, 1119–1124 (2016).

201. Wang, L., Nitopi, S. A., Bertheussen, E., Orazov, M., Morales-Guio, C. G., Liu, X., Higgins, D. C., Chan, K., Nørskov, J. K., Hahn, C. & Jaramillo, T. F. Electrochemical Carbon Monoxide Reduction on Polycrystalline Copper: Effects of Potential, Pressure, and pH on Selectivity toward Multicarbon and Oxygenated Products. *ACS Catal.* **8**, 7445–7454 (2018).
202. Pérez-Gallent, E., Marcandalli, G., Figueiredo, M. C., Calle-Vallejo, F. & Koper, M. T. M. Structure- and Potential-Dependent Cation Effects on CO Reduction at Copper Single-Crystal Electrodes. *J. Am. Chem. Soc.* **139**, 16412–16419 (2017).
203. Mistry, H., Reske, R., Strasser, P. & Cuenya, B. R. Size-Dependent Reactivity of Gold-Copper Bimetallic Nanoparticles During CO₂ Electroreduction. *Catal. Today* **288**, 30–36 (2017).
204. Kim, C., Dionigi, F., Beermann, V., Wang, X., Möller, T. & Strasser, P. Alloy Nanocatalysts for the Electrochemical Oxygen Reduction (ORR) and the Direct Electrochemical Carbon Dioxide Reduction Reaction (CO₂RR). *Adv. Mater.* **31**, 1805617 (2019).
205. Jović, V. & Jović, B. EIS and Differential Capacitance Measurements onto Single Crystal Faces in Different Solutions: Part II: Cu(111) and Cu(100) in 0.1 M NaOH. *J. Electroanal. Chem.* **541**, 13–21 (2003).
206. Schouten, K. J. P., Gallent, E. P. & Koper, M. T. The Electrochemical Characterization of Copper Single-Crystal Electrodes in Alkaline Media. *J. Electroanal. Chem.* **699**, 6–9 (2013).
207. Le Duff, C. S., Lawrence, M. J. & Rodriguez, P. Role of the Adsorbed Oxygen Species in the Selective Electrochemical Reduction of CO₂ to Alcohols and Carbonyls on Copper Electrodes. *Angew. Chem. Int. Ed.* **56**, 12919–12924 (2017).

208. Bagger, A., Arán-Ais, R. M., Halldin Stenlid, J., Campos dos Santos, E., Arnarson, L., Degn Jensen, K., Escudero-Escribano, M., Cuenya, B. R. & Rossmeisl, J. Ab Initio Cyclic Voltammetry on Cu (111), Cu (100) and Cu (110) in Acidic, Neutral and Alkaline Solutions. *ChemPhysChem* **20**, 3096–3105 (2019).
209. Yaguchi, M., Uchida, T., Motobayashi, K. & Osawa, M. Speciation of Adsorbed Phosphate at Gold Electrodes: a Combined Surface-Enhanced Infrared Absorption Spectroscopy and DFT Study. *J. Phys. Chem. Lett.* **7**, 3097–3102 (2016).
210. Tsuji, M., Yamaguchi, D., Matsunaga, M. & Alam, M. J. Epitaxial Growth of Au@Cu Core-Shell Nanocrystals Prepared Using the PVP-Assisted Polyol Reduction Method. *Cryst. Growth Des.* **10**, 5129–5135 (2010).
211. Frumkin, A. N. Influence of Cation Adsorption on the Kinetics of Electrode Processes. *Trans. Faraday Soc.* **55**, 156–167 (0 1959).
212. Paik, W., Andersen, T. & Eyring, H. Kinetic Studies of the Electrolytic Reduction of Carbon Dioxide on the Mercury Electrode. *Electrochim. Acta* **14**, 1217–1232 (1969).
213. Thorson, M. R., Siil, K. I. & Kenis, P. J. A. Effect of Cations on the Electrochemical Conversion of CO₂ to CO. *J. Electrochem. Soc.* **160**, F69–F74 (2012).
214. Anderson, M. R. & Huang, J. The Influence of Cation Size Upon the Infrared Spectrum of Carbon Monoxide Adsorbed on Platinum Electrodes. *J. Electroanal. Chem.* **318**, 335–347 (1991).
215. Jiang, X. & Weaver, M. J. The Role of Interfacial Potential in Adsorbate Bonding: Electrode Potential-Dependent Infrared Spectra for Saturated CO Adlayers on Pt(110) and Related Electrochemical Surfaces in Varying Solvent Environments. *Surf. Sci.* **275**, 237–252 (1992).

216. Mills, J. N., McCrum, I. T. & Janik, M. J. Alkali Cation Specific Adsorption onto fcc(111) Transition Metal Electrodes. *Phys. Chem. Chem. Phys.* **16**, 13699–13707 (27 2014).
217. Kolb, D. & Schneider, J. Surface Reconstruction in Electrochemistry: Au(100-(5×20), Au(111)-(1×23) and Au(110)-(1×2). *Electrochim. Acta* **31**, 929–936 (1986).
218. Wang, J., Davenport, A. J., Isaacs, H. S. & Ocko, B. M. Surface Charge-Induced Ordering of the Au(111) Surface. *Science* **255**, 1416–1418 (1992).
219. Broekmann, P., Wilms, M., Spaenig, A. & Wandelt, K. Morphological Aspects of Sulfate-Induced Reconstruction of Cu(111) in Sulfuric Acid Solution: In Situ STM Study. *Prog. Surf. Sci.* **67**, 59–77 (2001).
220. Goletti, C., Bussetti, G., Violante, A., Bonanni, B., Di Giovannantonio, M., Serrano, G., Breuer, S., Gentz, K. & Wandelt, K. Cu(110) Surface in Hydrochloric Acid Solution: Potential Dependent Chloride Adsorption and Surface Restructuring. *J. Phys. Chem. C* **119**, 1782–1790 (2015).
221. Ayemoba, O. & Cuesta, A. Spectroscopic Evidence of Size-Dependent Buffering of Interfacial pH by Cation Hydrolysis during CO₂ Electroreduction. *ACS Appl. Mater. Interfaces* **9**, 27377–27382 (2017).
222. Yan, Y.-G., Li, Q.-X., Huo, S.-J., Ma, M., Cai, W.-B. & Osawa, M. Ubiquitous Strategy for Probing ATR Surface-Enhanced Infrared Absorption at Platinum Group Metal-Electrolyte Interfaces. *J. Phys. Chem. B* **109**, 7900–7906 (2005).
223. Wang, H.-F., Yan, Y.-G., Huo, S.-J., Cai, W.-B., Xu, Q.-J. & Osawa, M. Seeded Growth Fabrication of Cu-on-Si Electrodes for *in situ* ATR-SEIRAS Applications. *Electrochim. Acta* **52**, 5950–5957 (2007).

224. Rodes, A, Orts, J., Pérez, J., Feliu, J. & Aldaz, A. Sulphate Adsorption at Chemically Deposited Silver Thin Film Electrodes: Time-Dependent Behaviour as Studied by Internal Reflection Step-Scan Infrared Spectroscopy. *Electrochem. Commun.* **5**, 56–60 (2003).
225. Zhao, Y., Liu, J., Liu, C., Wang, F. & Song, Y. Amorphous CuPt Alloy Nanotubes Induced by $\text{Na}_2\text{S}_2\text{O}_3$ as Efficient Catalysts for the Methanol Oxidation Reaction. *ACS Catal.* **6**, 4127–4134 (2016).
226. Lü, F., Qi, G., Liu, X., Zhang, C., Guo, R., Peng, X., He, J. & Luo, J. Selective Electrolysis of CO_2 to CO on Ultrathin In_2Se_3 Nanosheets. *Electrochem. commun.* **103**, 127–132 (2019).
227. Watanabe, M., Zhu, Y. & Uchida, H. Oxidation of CO on a Pt-Fe Alloy Electrode Studied by Surface Enhanced Infrared Reflection-Absorption Spectroscopy. *J. Phys. Chem. B* **104**, 1762–1768 (2000).
228. Yajima, T., Uchida, H. & Watanabe, M. In-Situ ATR-FTIR Spectroscopic Study of Electro-oxidation of Methanol and Adsorbed CO at Pt-Ru Alloy. *J. Phys. Chem. B* **108**, 2654–2659 (2004).
229. Zhu, S., Wang, Q., Qin, X., Gu, M., Tao, R., Lee, B. P., Zhang, L., Yao, Y., Li, T. & Shao, M. Tuning Structural and Compositional Effects in Pd-Au Nanowires for Highly Selective and Active CO_2 Electrochemical Reduction Reaction. *Adv. Energy Mater.* **8**, 1802238 (2018).
230. Yuan, X., Zhang, L., Li, L., Dong, H., Chen, S., Zhu, W., Hu, C., Deng, W., Zhao, Z.-J. & Gong, J. Ultrathin Pd-Au Shells with Controllable Alloying Degree on Pd Nanocubes toward Carbon Dioxide Reduction. *J. Am. Chem. Soc.* **141**, 4791–4794 (2019).

231. Neubrech, F., Huck, C., Weber, K., Pucci, A. & Giessen, H. Surface-Enhanced Infrared Spectroscopy Using Resonant Nanoantennas. *Chem. Rev.* **117**, 5110–5145 (2017).
232. Yao, Y., Chen, W., Du, Y., Tao, Z., Zhu, Y. & Chen, Y.-X. An Electrochemical in Situ Infrared Spectroscopic Study of Graphene/Electrolyte Interface under Attenuated Total Reflection Configuration. *J. Phys. Chem. C* **119**, 22452–22459 (2015).
233. Huck, C., Vogt, J., Sendner, M., Hengstler, D., Neubrech, F. & Pucci, A. Plasmonic Enhancement of Infrared Vibrational Signals: Nanoslits versus Nanorods. *ACS Photonics* **2**, 1489–1497 (2015).
234. Hentschel, M., Weiss, T., Bagheri, S. & Giessen, H. Babinet to the Half: Coupling of Solid and Inverse Plasmonic Structures. *Nano Lett.* **13**, 4428–4433 (2013).
235. Qiao, B., Wang, A., Yang, X., Allard, L. F., Jiang, Z., Cui, Y., Liu, J., Li, J. & Zhang, T. Single-Atom Catalysis of CO Oxidation Using Pt₁/FeO_x. *Nat. Chem.* **3**, 634 (2011).
236. Zhang, Z., Zhu, Y., Asakura, H., Zhang, B., Zhang, J., Zhou, M., Han, Y., Tanaka, T., Wang, A., Zhang, T., *et al.* Thermally Stable Single Atom Pt/m-Al₂O₃ for Selective Hydrogenation and CO Oxidation. *Nat. Commun.* **8**, 1–10 (2017).